FACULTY OF ENGINEERING AND ARCHITECTURE

Design of a High Torque Density Electric Actuator for Quasi-Direct-Drive Robot Applications

Jordi Van Damme

Doctoral dissertation submitted to obtain the academic degree of
Doctor of Electromechanical Engineering

Supervisors
Prof. Guillaume Crevecoeur, PhD - Prof. Hendrik Vansompel, PhD
Department of Electromechanical, Systems and Metal Engineering
Faculty of Engineering and Architecture, Ghent University

October 2023

GHENT UNIVERSITY

ISBN 978-94-6355-753-5
NUR 959, 929
Wettelijk depot: D/2023/10.500/85

Members of the Examination Board

Chair

Prof. Filip De Turck, PhD, Ghent University

Other members entitled to vote

Prof. Peter Sergeant, PhD, Ghent University
Prof. Ilya T'Jollyn, PhD, Universiteit Antwerpen
Jonathan Terfurth, PhD, 1X Technologies, Norway
Prof. Em. Alex Van den Bossche, PhD, Ghent University

Supervisors

Prof. Guillaume Crevecoeur, PhD, Ghent University
Prof. Hendrik Vansompel, PhD, Ghent University

Voorwoord

Een professor emeritus zei me ooit met een guitig lachje: “het moeilijkste aan een doctoraat is weten hoe je moet beginnen en weten hoe je moet eindigen.” Wel, ik denk te kunnen zeggen dat mijn doctoraat hier een mooi voorbeeld van is. Degenen die mij van dichtbij hebben opgevolgd zullen dit ook misschien beamen. Zo maak ik ietwat geniepig de sprong naar waar ik in dit voorwoord naartoe wil: iedereen die van dichtbij betrokken was oprecht bedanken.

Eerst en vooral wil ik mijn beide promotoren bedanken. Hendrik, jouw passie en bevlogenheid voor uw vak werkten bijzonder aanstekelijk en motiveerden mij om telkens het onderste uit de kan te halen. Jouw kennis en ervaring zijn bewonderenswaardig en ik ben je dan ook dankbaar dat je deze met mij wou delen. De brainstorm sessies aan bord waarbij we fundamenteel nieuwe ideeën en concepten rond elektrische machines verkenden, zullen me steeds bijblijven. Guillaume, bedankt voor je vertrouwen en geloof in mij en je eindeloze optimisme. Op momenten dat ik zelf het noorden even kwijt was over welke onderzoeksrichting nu in te slaan, stond jij altijd klaar met raad. Jij wist als doorwinterd wetenschapper steeds de juiste vragen te stellen die uiteindelijk zicht gaven op de volgende stappen. Hendrik, Guillaume, bedankt om mij de kans te geven te doctoreren en mij de vrijheid te geven mijn interesses te exploreren en mijn passie te ontdekken en hiermee aan te slag te kunnen gaan in mijn onderzoek. Hierdoor heb ik een kleine bijdrage kunnen leveren aan de wetenschappelijke wereld waar ik nu oprecht fier op ben.

Naast mijn promotoren, wil ik ook mijn collega’s en bureaugenoten van het Laboratorium voor Elektrische Energie (EElab) bedanken voor hun verantwoordelijkheid in het creëren van een aangename werkomgeving in al zijn facetten. In het bijzonder, had ik hier graag prof. em. Alex Van den Bossche en prof. Peter Sergeant vermeld. Ondanks dat zij niet rechtstreeks betrokken waren bij mijn onderzoek, heb ik hun interesse en nieuwsgierigheid in mijn werk steeds gewaardeerd omdat dit een bron van motivatie was voor mij.

Tijdens dit bijna 5-jarig avontuur, heb ik ook de eer en het genoegen gehad met zeer veel nieuwe mensen buiten mijn labo samen te werken. Deze samenwerkingen waren voor mij bijzonder leerrijk en verrijkend op persoonlijk vlak. Ik sta er nog telkens versteld van hoe mensen volledige

belangenloos en gedreven door wetenschappelijke nieuwsgierigheid steeds klaar stonden om mij te helpen ondanks hun eigen drukke agenda's. Bedankt Koen Faes en Rafael Nunes van het Belgisch Lasinstituut, Jurgen Adriaensen van Absolem, Koen Vervaeke, Femke Parthoens en Glenn Noé van Magcam, Johannes von Lindenfels van de universiteit van Erlangen-Nürnberg, Lukas Reißenweber van de hogeschool van Coburg. Yvan Van Gorp van Henkel en Arne Simons uit de vakgroep Materialen, Textiel en Chemische Proceskunde van dezelfde faculteit als mezelf.

Ik wil Tony Boone, Vincent Gevaert en Lieven Van West bedanken voor hun hulp en advies bij het realiseren van de vele proefopstellingen en prototypes in het kader van dit proefschrift. De ludieke conversaties in de werkplaats zullen mij lang bijblijven. Ook wil ik Marilyn Van den Bossche, Ingrid Dubois en Katrien Verstraete bedanken voor hun hulp bij het verwerken van de vele offertes, facturen, onkostennota's enzovoort en Nic Vermeulen voor zijn assistentie en hulp bij ICT-gerelateerde taken.

Voor het voltooien van mijn doctoraat ben ik niet alleen de hierboven vernoemde mensen uit mijn wetenschappelijke omgeving dankbaar, ook mijn familie, schoonfamilie en vrienden wil ik bedanken om voor de nodige rust, ontspanning en afwisseling te zorgen waardoor ik steeds weer met frisse geest en nieuwe ideeën weer aan het werk kon.

Mama, Papa, bedankt voor het warme nest waarin ik ben mogen opgroeien, en voor de veilige en zorgeloze omgeving waarin wij onze passies konden ontdekken. Bedankt om mij de bagage mee te geven om deze uitdaging aan te gaan en er steeds te zijn wanneer het nodig was op welke manier dan ook. Mijn broer, Janick, bedankt om tijdens mijn doctoraat af en toe mijn blik eens te verruimen en mij door uw geheel eigen kritische vragen mij te helpen de focus terug te vinden. Dankjewel dat ik ook steeds op jou kon/kan rekenen. Laura, een doctoraat eindigt niet wanneer je 's avonds het labo verlaat, ik denk dat jij dat als geen ander kan beamen, ondanks dat jij geen invloed hebt gehad in mijn keuze om te doctoreren ben jij me wel onvoorwaardelijk en onberispelijk blijven steunen op een heel warme, begripvolle en tactvolle manier die slechts weinigen je zouden nadoen. Dankjewel noesje!

Jordi Van Damme, 22 juli 2023

Opdat je nooit zou vergeten worden,

aan mijn dierbare nonkel, Christaan Van Damme

° 27 augustus 1958 - † 29 juli 2023

Contents

Summary

Our modern factories and warehouses are built around robots. They are configured so as to simplify the deployment of robots as much as possible. This strategy has proven very effective for the last few decades to automate a large number of repetitive and/or precise tasks. However, a large part of all work still takes place outside a controlled factory environment. To provide an answer to the upcoming labor shortage and the need for higher productivity, robots have to leave the confined factory floor and enter the real world. In the past, both the robot and its environment could be co-designed to maximize productivity. In the future, robots will have to be adapted to deal with unstructured, unknown and changing environments. This will involve a paradigm shift in all robot design aspects from mechanical structure over sensing and control to actuation. This work will focus on the robot's actuation architecture which has to shift away from stiff and heavy actuators based on a high ratio transmission which excels in predefined position-controlled tasks to lightweight, compliant, backdrivable and robust actuators which are required to safely interact with humans and the environment, and survive intentional or unintentional collisions.

There are several strategies to realize these actuators which can be classified in three groups: (1) strategies using a high ratio transmission and a torque sensor, (2) strategies using a high ratio transmission and a fixed or variable compliant mechanism and, (3) strategies using a low ratio transmission, so called quasi-direct-drive actuators. The latter has an excellent backdrivability and thus robustness. Compliance can be realised through impedance control based on motor currents and it has a low complexity because it doesn't require an additional variable compliance mechanism or torque sensor. A major drawback of this actuator architecture is its low torque density due to its low ratio transmission. In this regard, state-of-the-art quasi-direct-drive actuators closely integrate the electric motor and power electronics to eliminate separate enclosures and connectors, and share a cooling system. Because the outer diameter is typically constrained in robotics applications, the power electronics are integrated axially. Depending on the application specifications different integration approaches are possible. Since literature on the evaluation of the torque density of a particular integration is scarce, this work starts with

the introduction of an axial endplate mount integration concept. It consists of a Yokeless and Segmented Armature Axial Flux Permanent Magnet Synchronous Machine (YASA AFPMSM), an Insulated Metal Substrate Printed Circuit Board and a radially finned heatsink with a frameless centrifugal fan in its centre. The torque density of a hardware realization of this concept is evaluated using 3D thermal finite element model which is validated using experimental data. A torque density of 2 Nm/kg was achieved. The type of conductor and rotor mass were identified as key bottlenecks for the torque density. To take full benefit from the advantages of quasi-direct-drives, this dissertation aims to increase their torque density by addressing three key challenges.

First, the limited torque density due to the type of conductor is addressed. It is the consequence of the limited thermal conductivity and fill factor of a winding based on round enamelled copper wire. Therefore the use of anodised aluminum foil conductors is evaluated. Due to the ceramic aluminum-oxide layer constituting the electrical insulation, the winding equivalent thermal conductivity is higher. Additionally, aluminum is also three times less dense than copper and a foil conductor enables a higher fill factor. On the other hand, aluminum has a higher resistivity and the flux impinging the foil surface might lead to excessive AC losses. Two electromagnetically identical YASA AFPMSMs were build, one with each type of conductor. Both were compared on a testbench up to 300 rpm (direct-drive applications), and a 13 % higher torque per kg active stator mass was measured due to the low density and high fill factor of aluminum. The superior thermal properties could not be exploited since the winding was not dominant in the thermal path from heat source to heatsink. It could be concluded that anodised aluminum foil offers an attractive alternative for round enamelled copper wire.

The second key challenge is related to manufacturing a stator with anodised aluminum foil winding. Resolving this challenge is a prerequisite to evaluate its performance. Due to the limited thickness of the foil and the brittleness of the ceramic oxide-layer, excessive bending or puncturing of the foil should be avoided. Moreover, the breakdown voltage depends on the bending radius. Hence insertion of the foil in the slots of a radial flux machine is seldom possible. To overcome this a YASA AFPMSM topology is used. Its inherent segmented nature allows to rely on existing foil winding techniques. Its preliminary design is described based on the requirements of quasi-direct-drive actuators. The aluminum-oxide layer also impedes the soldering of a copper wire on the foil using regular soldering methods for copper wire. In this work ultrasonic welding was studied extensively, however satisfactory mechanical properties of the weld could not be guaranteed. A method in which the two ends of a foil are first electrolytically nickel-coated to facilitate regular soldering was used. This method produced repeatable and satisfactory connections for further coil handling.

The final challenge addressed in this work is the overheating during standstill due to an uneven loss distribution. In robot applications, long periods of high torque at almost standstill occur frequently. This is also known as stall torque. During this operation mode, the majority of conduction losses are concentrated in a single phase. If a motor has to generate its rated torque in the worst-case rotor position, even twice the rated losses are generated in a single phase resulting in overheating. Derating of the stall torque is thus necessary. To address this, the influence of key parameters that have an impact on the tangential heat transport are studied: the slot/pole combination, the thermal end-winding interconnection and the equivalent thermal conductivity of the winding. A DC current is injected in a stator which is configured to emulate the worst-case loss distribution. The measured thermal resistance is used to determine the impact of the aforementioned parameters on the stall torque derating. It could be concluded that the slot/pole combination and thermal end-winding interconnection have a limited impact on the stall torque performance. A higher equivalent thermal conductivity resulted in both a higher stall torque and rated torque. So it is more effective to focus on improving rated thermal performance as this also improves stall torque performance.

To summarize: an axial endplate mount integration concept using a YASA AFPMSM was realised in this dissertation and the use of anodised aluminum foil was studied to increase its torque density, both during continuous operation and at standstill.

In future work, the optimization of the rotor mass will be studied to further increase torque density by considering the use of lightweight composite structures. This will be done in the recently granted Horizon RIA European project CliMAFlux. Also more fundamental and applied research into the electrical insulation properties of anodised aluminum will be required to increase confidence in this novel conductor type. To exploit the high temperature capabilities and realize a significant leap in torque density, more research will be required to replace all organic polymers used in the electric motor.

Samenvatting

Onze moderne fabrieken en logistieke verdeelcentra zijn gebouwd rond robots. Ze zijn zo ontworpen om de inzet van robots zo eenvoudig mogelijk te maken. Deze strategie is de afgelopen decennia zeer effectief gebleken voor het automatiseren van een groot aantal repetitieve en/of taken met hoge precisie. Een groot deel van al het werk vindt echter nog steeds plaats buiten een gecontroleerde fabrieksomgeving. Om een antwoord te bieden op het toekomstige tekort aan arbeidskrachten en de behoefte aan een hogere productiviteit, zullen robots ook meer en meer buiten de fabrieksmuren ingezet worden. In het verleden konden de robot en zijn (fabrieks)omgeving samen ontworpen worden om de productiviteit te maximaliseren. In de toekomst zullen robots aangepast moeten worden om om te gaan met ongestructureerde, onbekende en veranderende omgevingen. Dit zal een ware paradigmaverschuiving vereisen in alle aspecten van robotontwerp: van mechanische ontwerp over sensoren en controle tot actuatoren. Dit proefschrift focust op de actuatiearchitectuur. Deze moet verschuiven van stijve en zware actuatoren gebaseerd op een transmissie met een hoge overbrengingsverhouding die uitblinken in vooraf gedefinieerde positie-gecontroleerde taken, naar lichtgewicht, flexibele, "backdrivable" en robuuste actuatoren. Deze zijn nodig om een veilige interactie met mens en omgeving te garanderen en om opzettelijke en onopzettelijke botsingen te overleven.

Er zijn verschillende strategieën om deze actuatoren te realiseren, deze kunnen worden onderverdeeld in drie groepen: (1) strategieën gebaseerd op een transmissie met een hoge overbrengingsverhouding en koppelsensor, (2) strategieën gebaseerd op een transmissie met een hoge overbrengingsverhouding en een vast of variabel veer-demper systeem en (3) strategieën gebaseerd op een transmissie met een lage overbrengingsverhouding, de zogenaamde quasi-directe aandrijving. De laatste heeft zijn uitstekende "backdrivability" en dus robuustheid te danken aan de lage overbrengingsverhouding. Dit soort actuatoren kan zijn flexibiliteit regelen door middel van impedantiecontrole op basis van de motorstromen. De afwezigheid van koppelsensor of extra veer-demper systeem zorgt bovendien voor een lage complexiteit. Een groot nadeel van deze actuatorarchitectuur is de lage koppeldichtheid als

gevolg van de lage overbrengingsverhouding. In dit opzicht integreren de nieuwste quasi-direct aangedreven actuatoren reeds de elektromotor en vermogenselektronica. Dit laat toe om aparte behuizingen en connectoren te elimineren en een koelsysteem te delen. Omdat de buitendiameter meestal beperkt is in robottoepassingen, is de vermogenselektronica typisch axiaal geïntegreerd. Afhankelijk van de toepassingsspecificaties zijn verschillende integratiebenaderingen mogelijk. Omdat literatuur over de evaluatie van de koppeldichtheid van een bepaalde integratie schaars is, begint dit werk met de introductie van een integratieconcept voor een axiale eindplaatbevestiging van de vermogenselektronica. Het integratieconcept bestaat uit een jukloze axiale-flux permanent magneet bekrachtigde synchrone machine met gesegmenteerde stator (YASA AFPMSM), een printplaat met geïsoleerd metalen substraat en een koelplaat met radiale vinnen met een frameloze centrifugaalventilator in het midden. De koppeldichtheid van een hardwarerealisatie van dit concept wordt geëvalueerd met behulp van een 3D thermisch eindige-elementenmodel dat werd gevalideerd met experimentele gegevens. Er werd een koppeldichtheid van 2 Nm/kg bereikt. Het type geleider en de rotormassa werden geïdentificeerd als de belangrijkste oorzaken voor de beperkte koppeldichtheid. Om de voordelen van quasi-directe aandrijvingen ten volle te benutten is dit proefschrift gericht op het verhogen van hun koppeldichtheid door drie belangrijke uitdagingen aan te pakken.

Ten eerste wordt de beperkte koppeldichtheid als gevolg van het type geleider aangepakt. Dit is het gevolg van de beperkte thermische geleidbaarheid en vulfactor van een wikkeling op basis van ronde, gelakte koperdraad. Om hier een antwoord op te bieden wordt het gebruik van geanodiseerde aluminiumfolie geleiders voorgesteld. Door de keramische aluminiumoxide laag die de elektrische isolatie vormt, is de equivalente warmtegeleiding van de wikkeling hoger. Bovendien heeft aluminium ook een drie keer lagere massadichtheid in vergelijking met koper en kan een hogere vulfactor bereikt worden met folievormige geleiders. Aan de andere kant, heeft aluminium een hogere weerstand en de flux die op het oppervlak van de folie valt kan leiden tot overmatige AC verliezen. Twee elektromagnetisch identieke YASA AFPMSM's werden gebouwd, één met elk type geleider. Beide werden vergeleken op een testbank tot 300 rpm (toepassingen met directe aandrijving), en een 13 % hoger koppel per kg actieve statormassa werd gemeten vanwege de lage dichtheid en en hoge vulfactor van aluminium. De superieure thermische eigenschappen konden niet worden benut omdat de wikkeling niet dominant was in het thermische pad van warmtebron naar koellichaam. Er kon geconcludeerd worden dat geanodiseerde aluminiumfolie een aantrekkelijk alternatief biedt voor ronde, gelakte koperdraad.

De tweede belangrijke uitdaging heeft te maken met de productie van een statorwikkeling uit geanodiseerde aluminium folie. Het oplossen van deze

uitdaging is een eerste vereiste om de prestaties van dit nieuwe geleidertype te evalueren. Vanwege de beperkte dikte van de folie en de brosheid van de keramische oxidelaag moet overmatig buigen of doorboren van de folie worden vermeden. Bovendien hangt de doorslagspanning af van de buigradius. Daarom is het zelden mogelijk om de folie in de gleuven van een radiale fluxmachine te plaatsen. Om dit te verhelpen wordt een YASA AFPMSM topologie gebruikt. De inherent gesegmenteerde aard maakt het mogelijk om te vertrouwen op bestaande wikkeltechnieken voor folie. Het ontwerp wordt beschreven op basis van de vereisten voor quasi-direct aangedreven actuatoren. De aluminiumoxidelaag verhindert ook het solderen van een koperdraad op de folie met de gebruikelijke soldeermethoden. In dit werk wordt ultrasoon lassen uitgebreid bestudeerd, maar deze methode kon geen bevredigende mechanische eigenschappen van de las garanderen. Een methode waarbij de twee uiteinden van een folie eerst elektrolytisch vernikkeld werden om er nadien een koperdraad op te solderen werd daarom voorgesteld. Deze methode leverde herhaalbare verbindingen met voldoende sterke mechanische eigenschappen voor daaropvolgende productiestappen.

De laatste uitdaging die werd aangepakt in dit werk is de oververhitting tijdens stilstand als gevolg van een ongelijkmatige verliesverdeling. Bij robottoepassingen komen lange perioden van hoog koppel bij bijna stilstand regelmatig voor. Tijdens deze bedrijfsmodus zijn de meeste geleidingsverliezen geconcentreerd in één fase. Als een motor zijn nominale koppel moet genereren wanneer hij in de slechtst mogelijke rotorpositie staat, worden zelfs twee keer de nominale verliezen gegenereerd in één enkele fase, wat leidt tot ontoelaatbare opwarming. Het koppel bij stilstand moet dus beperkt worden. Om dit probleem aan te pakken, wordt de invloed van belangrijke parameters die een invloed hebben op de tangentiële warmtegeleiding bestudeerd, zijnde: de sleuf/poolcombinatie, de thermische interconnectie van de spoelkoppen en de equivalente thermische geleidbaarheid van de wikkeling. Er wordt een gelijkstroom geïnjecteerd in een stator die geconfigureerd is om de slechtst denkbare verliesverdeling na te bootsen. De gemeten thermische weerstand wordt gebruikt om de invloed te bepalen van de bovengenoemde parameters op de noodzakelijke beperking van het stilstandkoppel. Er kan geconcludeerd worden dat de sleuf/pool combinatie en thermische interconnectie van de spoelkoppen een, zij het beperkte, invloed hebben op het stilstandkoppel. De verhoging van de equivalente thermische geleidbaarheid resulteerde in zowel een hoger stilstandkoppel als nominaal koppel. Het is dus effectiever om te focussen op het verbeteren van de thermische performantie in nominale omstandigheden, aangezien dit ook de prestaties bij stilstand verbetert.

Samenvattend: een concept gebaseerd op axiale eindplaatmontage voor de integratie van vermogenselektronica en elektrische motor van het YASA AFPMSM type werd gerealiseerd in dit proefschrift en het gebruik van geanodis-

eerde aluminium folie werd bestudeerd om de koppeldichtheid te verhogen, zowel tijdens continu bedrijf en bij stilstand.

In toekomstig werk zal gepoogd moeten worden de koppeldichtheid verder te verhogen door een reductie van de rotormassa door het gebruik van lichtgewicht composietstructuren. Dit zal gebeuren in het kader van het onlangs toegekende Horizon RIA Europese project CliMAFlux. Ook zal er meer fundamenteel en toegepast onderzoek nodig zijn naar de elektrische isolatie-eigenschappen van geanodiseerd aluminium om het vertrouwen in dit nieuwe geleidertype te vergroten. Een volgende grote stap in de koppeldichtheid is mogelijk door gebruik te maken van het feit dat geanodiseerd aluminium in principe bestand is tegen zeer hoge temperaturen. Echter om deze eigenschap ten volle te benutten, zal eerst meer onderzoek nodig zijn om alle organische polymeren te vervangen.

List of Abbreviations

- AFPMSM: Axial Flux Permanent Magnet Synchronous Machine
- back-emf: back electromotive force
- CNC: Computer Numerically Controlled
- DC: Direct Current
- FE: Finite Element
- IMD: Integrated Motor Drive
- IMS: Insulated Metal Substrate
- I/O: Input/Output
- PCB: Printed Circuit Board
- PMSM: Permanent Magnet Synchronous Machine
- PWM: Pulse Width Modulation
- RMS: Root Mean Square
- rpm: rotations per minute
- VSA: Variable Stiffness Actuator
- YASA: Yokeless and Segmented Armature

Chapter 1

Introduction

1.1 Service Robots

In 1973, in a small factory in Sweden with only 20 employees called Magnussons AB, the very first industrial robot arm was installed [1]. It was used to handle and polish stainless steel tubes. Arguably, this could be seen as the start of modern robotization in the manufacturing industry. This first robot, ASEA's (now ABB) IRB 6 shown in Fig. 1.1, has several features of today's robots found in e.g. automotive assembly halls. It was the first serially produced, all-electric, microprocessor controlled robot arm for the manufacturing industry [2]. It was bought by the CEO of Magnussons AB to increase the productivity of his stainless steel pipe processing factory and even become one of the world's first unmanned factories to operate around the clock, seven days a week.

This story tangibly illustrates the zeitgeist of the 1960's and 1970's when robotics development took off [3]. Enabled by technological advancements in electronics and microprocessors, and driven by the need for higher productivity, robots were massively installed in Western countries to support their competitiveness in the global market [4].

Since the introduction of the first all-electric robot arm in 1973, robots have become an indispensable part of our modern manufacturing industry. The automotive and electronics industry host the lion's share of all robots deployed in manufacturing today [5] and the appearance of today's robot reflects the requirements of these industries. They consist of a set of heavy, rigid linkages forming a kinematic chain that is driven by brushless AC motors and gears and controlled via power electronics and microprocessors. These characteristics makes them perfectly suited to perform repetitive, heavy, and/or dangerous tasks, or tasks that require high productivity and/or precision in well-known environments. However, this is only a small subset of all indus-

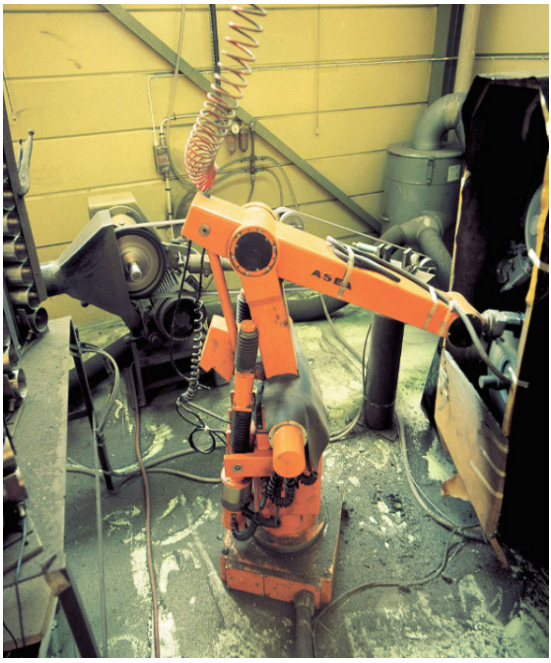

Figure 1.1: Picture of the very first ASEA (now ABB) IRB 6 at Magnussons AB in 1973. It was the very first, serially produced, all-electric, microprocessor controlled robot arm [3].

trial tasks [3]. When considering the world's population distribution today and the forecast for 2050 in Fig. 1.2, it can be concluded that the population is ageing. As a consequence of the decreasing workforce and the growing group of elderly people requiring care, a massive labour shortage is expected. This is the main driver for the ongoing technological developments in the field of robotics [4, 5]: create robots that can support in a much wider variety of tasks beyond the manufacturing industry. This will require novel robot designs that are tailored to the needs of new application areas such as: maintenance and inspection, logistics, healthcare and agriculture. To formalize the distinction between traditional robots found in the manufacturing industry and these new robot design, the International Federation of Robotics (IRF) has defined two types of robots in their World Robotics report of 2022 [5]: industrial robots and service robots.

Some well-known and already wide-spread applications of service robots are shown in Fig. 1.3 and include Automated Guided Vehicles (AGVs) and mobile robots. They have enabled and supported the boost in e-commerce. They are used in semi-automatic warehouses to collect goods that can then be prepared for transportation [7]. Even more visible in our everyday lives are

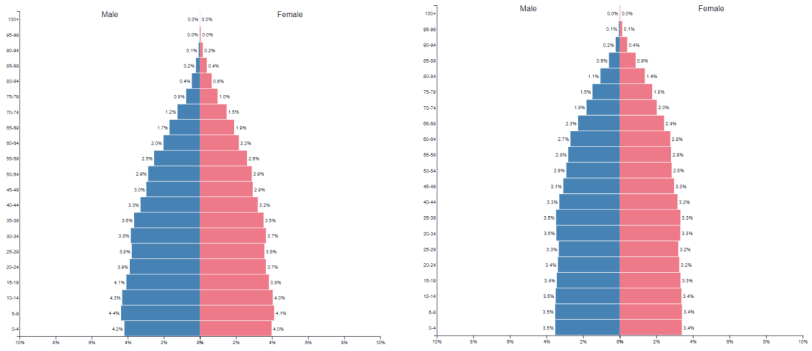

Figure 1.2: The world's current population distribution (left) and the forecasted distribution for 2050 (right) [6]

the vacuum cleaner and lawn mower robots that aim to alleviate the domestic workload by taking over some simple but time consuming chores [8].

Figure 1.3: Well established applications of service robots: (a) Automated Guided Vehicles in warehouses [7] (b) vacuum cleaner robot [8] (c) lawn mower robot [8]

The capabilities of existing commercially available service robots lag behind of what humans are capable of. They lack the senses, intelligence, dexterity, scale, speed, and force to perform human-scale service tasks with matching quality. When facing the upcoming labor shortage, robot platforms with human-like capabilities will be required to fill the skills gap in the future labour market [3, 5]. This vision on the future of robotics is already as old as the word robot itself which was first introduced in 1921 by a Czech playwright. The attempts to give a real shape to this vision are nearly as old. This has eventually culminated in several research fields that focus on realizing service robots endowed with human-like capabilities. In what follows, three types of service robots with significant potential impact on society are introduced: exoskeletons, legged quadruped robots and humanoid robots. The aim is to derive the specific requirements from the envisaged applications that have implications

Figure 1.4: Exoskeletons for industrial and rehabilitation applications [15, 16]

on the actuation system of the robot in order to identify the research needs. Although the performance of a robot does not only depend on its actuation capabilities, but is rather the result of a synergy of control, sensing and mechanical aspects, the focus in this dissertation is on the actuator as it was identified as a key factor for enabling service robotics with human-like capabilities [9–11].

1.1.1 Exoskeletons

Exoskeletons are actively-powered wearable robotic devices that support or replace the functions of the human muscular system. Although passive exoskeletons exist that only use passive elements like springs, research efforts focus on active exoskeletons due to their enhanced capabilities.

They are used in very diverse application areas as illustrated in Fig. 1.4. To alleviate the burden on the human body and improve the ergonomics of heavy manual labour as found for example in automotive industry [12], cargo handling [13] or construction [14], exoskeletons interact with their user to amplify the human forces and power. As more and more countries increase the retirement age in response to the ageing population (see Fig. 1.2), exoskeletons can offer a solution for the ageing workforce. For people with mobile disabilities, exoskeletons can be a means to (partially) regain their mobility and increase their quality of life. Exoskeletons are also used for rehabilitation purposes where they provide assistive forces and torques for people with reduced muscular power [15].

From the three types of service robots discussed in this section, exoskeletons exhibit the closest interaction with humans. Therefore it is of paramount importance, that this interaction is safe i.e. that it does not harm the user. Additionally, as is the case for the glasses on our nose, the interaction with the user has to feel comfortable and natural. Therefore exoskeletons have to be lightweight, compact, backdrivable and have a high mechanical bandwidth [17].

Backdrivablity means that the actuator can be back driven with minimal effort, factors affecting backdrivability are friction and inertia of the actuator. The perfect exoskeleton is an ideal torque source with a zero impedance over the bandwidth of human motion [18]. Sometimes the term transparent is used for a highly backdrivable actuator, this originates from the field of haptics and teleoperation where even more stringent requirements are put on the actuator in terms of backdrivability or transparency. The bandwidth is mainly determined by the mechanical construction of the exoskeleton, it should be high enough to support the wearer even in highly dynamic movements.

1.1.2 Legged Quadruped Robots

Inspired by nature, legged quadruped robots use four articulated legs to move through the real world as illustrated in Fig. 1.5. In comparison to their wheeled counterparts, they are better suited to navigate through unstructured, uncertain and changing terrains [19]. Therefore they constitute the ideal candidates to replace humans in maintenance and inspections tasks in hard to reach or hazardous environments [20]. To handle the extreme variety of terrains they might encounter, legged quadruped robots require truly multi-modal mobility: they have to be capable to perform static, highly stable motions when walking in an unknown and unstructured environment as well as dynamic motions to overcome obstacles on their path (e.g. jumping) [9, 21, 22]. To realize this multi-modal mobility, legged robots require some "sense of touch" encorporated in their actuators to perceive their environment. This is used in the absence of an accurate map to meticulously place their feet [23]. To perform acrobatic manoeuvres, the legs should be capable of achieving a high speed in a very short time, this requires actuators temporarily capable of generating high speed or torque.

To limit the impact forces during these dynamic manoeuvres, compliance is introduced in the legs. This can be done through the addition of passive elements such as springs and dampers. However, in order to successfully traverse a broad range of different terrains, a leg with variable compliance is required as this allows to realize a stable and energy efficient gait in a wider variety of situations including highly dynamic motions [24, 25].

1.1.3 Humanoid Robots

Humanoid robots aim to approach the versatile human capabilities by replicating the human morphology. They use articulated legs and arms for bipedal locomotion and object manipulation respectively. Due to their advanced capabilities, they can eventually replace human workers in hazardous and difficult to reach areas as well as on the factory floor. Although they strongly differ in

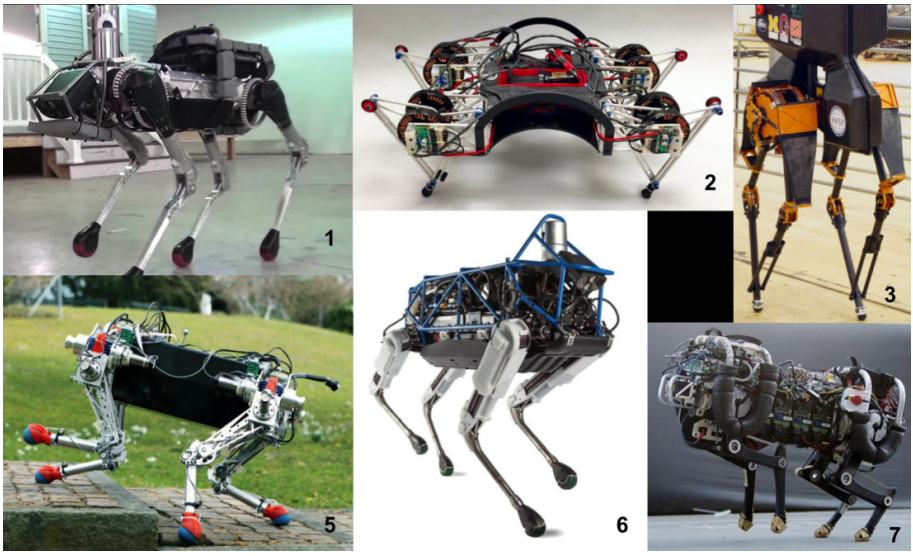

Figure 1.5: Legged quadruped robots [21]

morphology and capabilities, humanoid robots share largely the same requirements with legged quadruped robots. They also require a "sense of touch" to move through unknown and unstructured terrain and deal with unforeseen contacts [26]. They need variable compliance in their legs and arms to deal with impacts while maintaining their accuracy when required and they need the capability of high speed movements to overcome obstacles [27]. A final point of concern with humanoids is safety while operating in the neighbourhood of human coworkers. In commercial robot manipulator arms that are allowed to cooperate with humans, called cobots, this issue was resolved by combining strict force and speed limitations with a lightweight design [28]. However these limits are often too constraining for humanoid robots. Hindering them to reach their full potential. Therefore humanoids have to rely on a lightweight design and their variable compliance to limit impact forces during a collision accident [27].

1.1.4 Service Robot Requirements

Although the aforementioned types of service robots strongly differ in morphology and purpose, they share some requirements that originate from the trend that future service robots will have to leave the confined factory floor in a safe way for humans in order to fulfil their purpose i.e. close the gap in the labour market. The common requirements can be summarized as follows:

1. intrinsically safe to humans and their environment

Figure 1.6: Humanoid robots [11]

Table 1.1: Joint speed and torque requirements in different applications

Application	**Speed [rpm]**	**Torque [Nm]**	**Sources**
Exoskeleton	23–115	44–200	[17, 29–33]
Quadruped robot	65–355	17–58	[21, 34, 35]
Humanoid robot	11–335	33–516	[26, 27, 36–39]

2. robust to collisions
3. capable of highly dynamic motions
4. sensitive to perceive their environment

Apart from these qualitative design applications requirements, Table 1.1 summarizes the quantitative torque and speed requirements for the service robots discussed here above. Note that the torque and speed requirements span a wide interval which originates from the fact that multiple actuators on different locations are present in one service robot and the wide diversity of tasks a single robot might have to perform.

1.2 Actuator Architectures

In the previous section the requirements specific to future service robots were derived based on their applications needs. Although all of the aforementioned examples of service robots are the result of a holistic approach i.e. their performance depends on control, sensing, actuation and mechanical aspects. This section will focus on actuator architectures based on a rotary electromagnetic motor as primary source of motion. Although a wide variety of alternative motion sources exist, like hydraulic or pneumatic actuators to name only two examples, electric motors have dominated the commercial robot market [11] and therefore this is the first choice for many novel developments in the field of robotics. The examples mentioned in Sections 1.1.1,1.1.2 and 1.1.3 have proven that actuators based on rotary electric motors are excellent candidates to fulfil the requirement mentioned in Section 1.1.4. Additionally, they feature an excellent availability in a wide range of dimensions, torque and speed capabilities as mentioned in Table 1.1, low maintenance, and are easy to control with modern microprocessors and power electronics [11]. In what follows, the most prevalent actuators architectures used in future service robots are described and evaluated in terms of their suitability to fulfil the requirements postulated in Section 1.1.4. Largely four different classes of actuator architectures can be distinguished as illustrated in Fig. 1.7, these classes will be thoroughly discussed in the following paragraphs.

1.2.1 High Gear Ratio Actuators

High gear ratio actuators combine a high speed electric motor with a high gear ratio transmission such as strain-wave gears, cycloidal gears or multi-stage planetary gears (see Fig. 1.7(a)) [40]. Although there is no strict definition on what a high gear ratio is and the perception of a high gear ratio might be different in other application domains like automotive. In this work, a gear ratio is considered high if it cannot be achieved by a single stage, planetary gearbox, practically this means ratios larger than 10:1. Because in robotics, torque and not power is the limiting resource [21, 22], high gear ratio actuators offer an effective means for amplifying the electric motor torque. Moreover this allows the electric motor to operate at higher speeds where they tend to achieve a higher efficiency. Since without sufficient torque, robots cannot perform useful work, this actuator topology was chosen in the very first all-electric robot arm from Fig. 1.1. Nowadays, it is the prevailing standard for industrial robots [28]. Therefore, the first legged robots, and exoskeletons also adopted the same architecture [11]. An example of an actuator using a high ratio transmission is shown in Fig. 1.8.

However, high torque comes at the price of low speed. The input speed of a

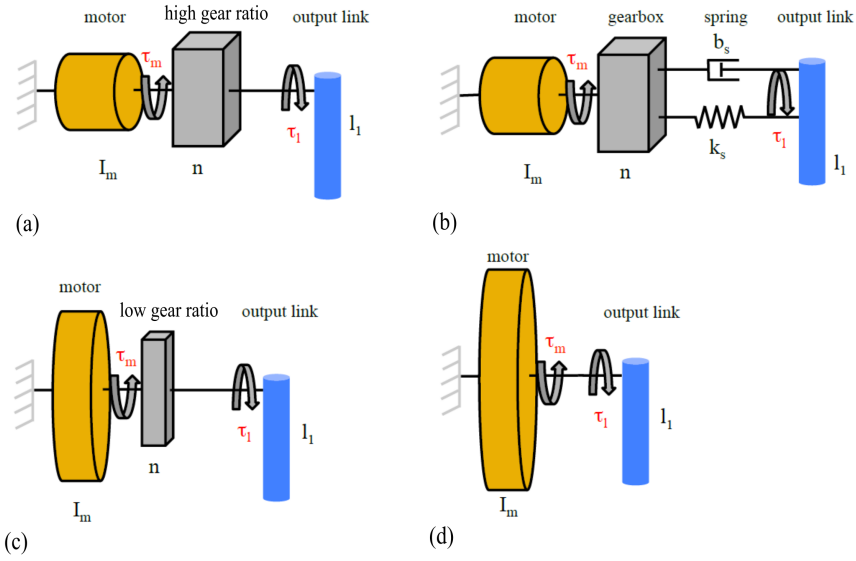

Figure 1.7: Overview of actuator architectures found in novel service robot applications: (a) High gear ratio actuator (b) Series elastic actuator (c) Quasi-direct-drive actuator (d) Direct-drive actuator (adapted from)[21]).

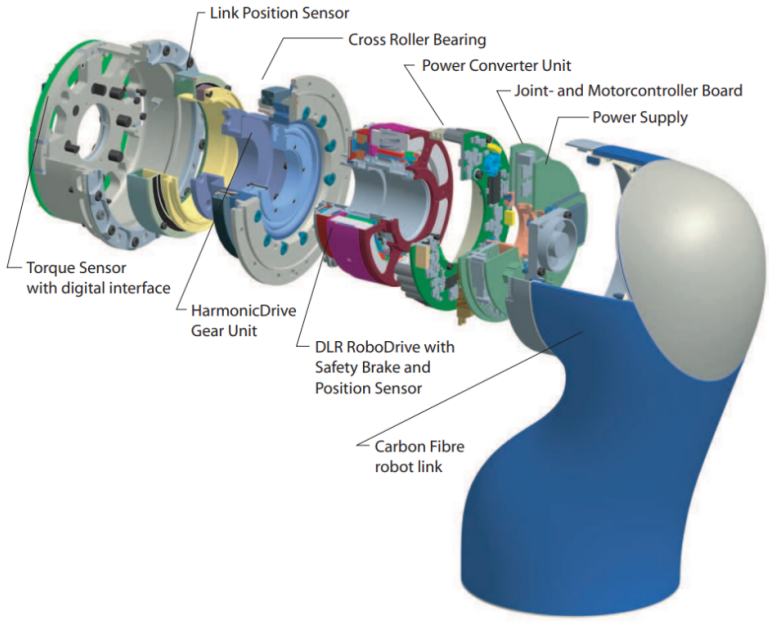

Figure 1.8: Actuator using a high gear ratio transmission [41]

gearbox is limited. First, there is a thermal constraint on the root-mean-square value of the input speed because gearbox losses increase with speed. This is typically the lowest speed limit, but the input speed can be temporarily higher as long as the root-mean-square value remains below the limit. An upper limit for short duration peaks in the input speed is imposed by the lubrication of the gears [42]. Proper lubrication of the contact area should minimize the friction and thus the wear, heat generation and noise. At higher input speeds, under the action of centrifugal forces, the lubricant is ejected from the gears. If the heat and noise can be tolerated by the design, the wear will eventually reduce the gearbox's lifetime. Spray lubrication enables the highest input speed, however this requires a pressurized oil circuit. To illustrate the speed limitation for the case of a quadruped robot: if a strain-wave gearbox is used with a 150:1 ratio, and its short term, input speed limit is 8000 rpm. The maximum output speed is only 53 rpm, which is typically insufficient to perform dynamic manoeuvres like jumps [26]. Additionally, the impact resistance of high gear ratio transmissions is also an issue [9, 43, 44]. Because in industrial robots, high precision is an important requirement, gearbox manufacturers have taken measures to reduce or eliminate backlash often at the cost of a reduced backdrivability. As a consequence, in the event of a collision or intentional non-zero speed contact, the impact forces are partially absorbed by the gears which can lead to tooth breakage [45]. The poor backdrivability of high gear ratio transmissions also impedes the opportunity to rely on motor current measurements for output torque estimation [44]. The output torque signal undergoes, as it were, a non-linear, non-time invariant transformation as it goes through the gearbox, making it difficult to use directly in mechanical impedance control, contact or collision detection. Some researchers have proposed to add a torque sensor to the actuator in order to obtain the sensitivity required to perceive their environment and mitigate collisions, however this adds extra weight and complexity. Additionally, some torque sensors are also prone to overload and require periodic recalibration. Therefore torque sensors are typically not desired in cost-sensitive applications [46].

1.2.2 Series Elastic and Variable Stiffness Actuators

Series elastic actuators rely on passive elements like springs and dampers between a high gear ratio transmission and the output link Fig. 1.7(b) to reduce the peak impact force seen by the gears during (non)-intentional contacts, making them more robust [47]. The addition of a spring makes series elastic actuators also safer for humans because the spring decouples the output link from the rest of the robot's mass during a collision, significantly limiting the impact severity [28]. Additionally, energy stored in the passive elements during parts of a motion cycle can be rapidly released during other parts of the cycle, which

helps to meet the speed requirement in highly dynamic movements [48]. The deflection of the elastic element can be measured and adjusted to control the torque of the output link [35]. This intrinsic torque sensing capability allows to perceive the environment. The series elastic actuator thus overcomes many shortcomings of stiff high gear ratio actuators. However the addition of passive elements reduces the mechanical bandwidth of the link, making it difficult to react to sudden changes in the environment.

Researchers have taken inspiration from nature to overcome this problem. Animals and humans can adjust the stiffness of their arms and legs to adapt to changing environments or to a collision [25, 27]. This principle is used in so-called Variable Stiffness Actuators (VSA). Typically, these actuators contain an additional actuated mechanism to adjust the stiffness of the spring. It allows legged robots to comply to varying terrains without loosing balance and cope with collisions [25]. Moreover, researchers have shown that higher energy efficiency can be obtained with a variable elastic element as compared to a fixed spring [49]. Despite the attractive features offered by VSAs, they typically feature a higher complexity, which makes their control challenging. Moreover, they don't exhibit inherent backdrivability, which means that in case of a fault in one of the VSA components, this can result in a complete loss of backdrivability which is catastrophic in case of a human-robot collision. Fig. 1.9 shows a famous example of a series elastic actuator and a variable stiffness actuator.

1.2.3 Quasi-Direct-Drive Actuators

A quasi-direct-drive actuator comprises an electric motor and a low gear ratio transmission between the motor and output link as shown in Fig. 1.7(c). Typically the transmission is a single stage planetary gear [9, 21, 26, 29, 50] or timing belt transmission [51, 52] with a gear ratio smaller than or equal to 10:1 [53]. A few examples are given in Fig. 1.10.

Quasi-direct-drive actuators offer a compromise between high gear ratio actuators that have a poor backdrivability and impact robustness, and series elastic actuators that are backdrivable and more robust but less adaptive to deal with changes in the environment because the elastic element reduces their mechanical bandwidth. Just like VSA's, quasi-direct-drive actuators can adapt the virtual stiffness of the output link by relying on so-called impedance control [57]. This is a motor control strategy in which the output link force or torque is estimated or measured and the motor position, velocity and acceleration are controlled in accordance with a preprogrammed mechanical impedance law. It is as if the link-environment interaction is governed by a passive mechanical element with a preprogrammed impedance. Due to the low gear ratio, friction and other non-linear gear effects remain limited and the

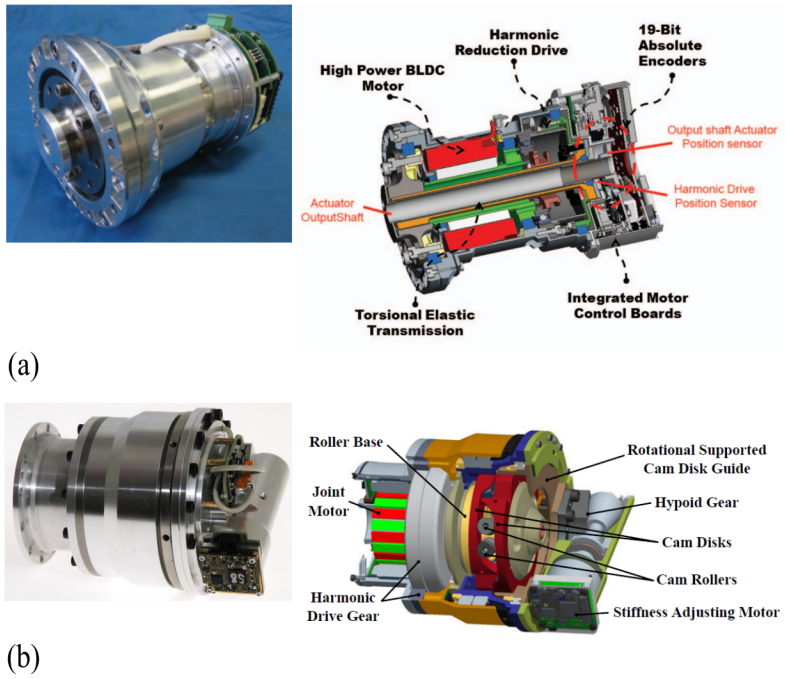

Figure 1.9: Series elastic actuator [36] (a); Variable Stiffness Actuator [48] (b)

motor currents can be used to estimate the output torque [21, 38, 55]. In contrast to VSA's, quasi-direct-drive actuators don't require a complex mechanical system to adjust the link stiffness. The low gear ratio allows to achieve significantly higher output speeds without violating the input speed limitations of the transmission. This has made quasi-direct-drive actuators a popular actuator choice in legged quadrupeds and small humanoid robots that have to perform highly dynamic manoeuvres [26, 55].

One of the major drawbacks of quasi-direct-drive actuators is their low torque density due to their low gear ratio [10, 56]. This is truly the limiting factor for the capabilities of today's robots based on quasi-direct-drive actuators. In [9], it was shown analytically that the torque density scales with the airgap radius of the motor. This statement was confirmed empirically by analysing motor catalog data as shown in Fig. 1.11. Under a fixed actuator mass constraint, and assuming constant stator and rotor thickness the axial length has to scale with the inverse of the motor radius: $l \sim 1/r$, hence large airgap radius, short axial length also called 'pancake-shaped' motors are often used in quasi-direct-drive actuators [9]. A disadvantage of pancake-shaped motors is their large torque ripple [59] which makes their control more challenging and

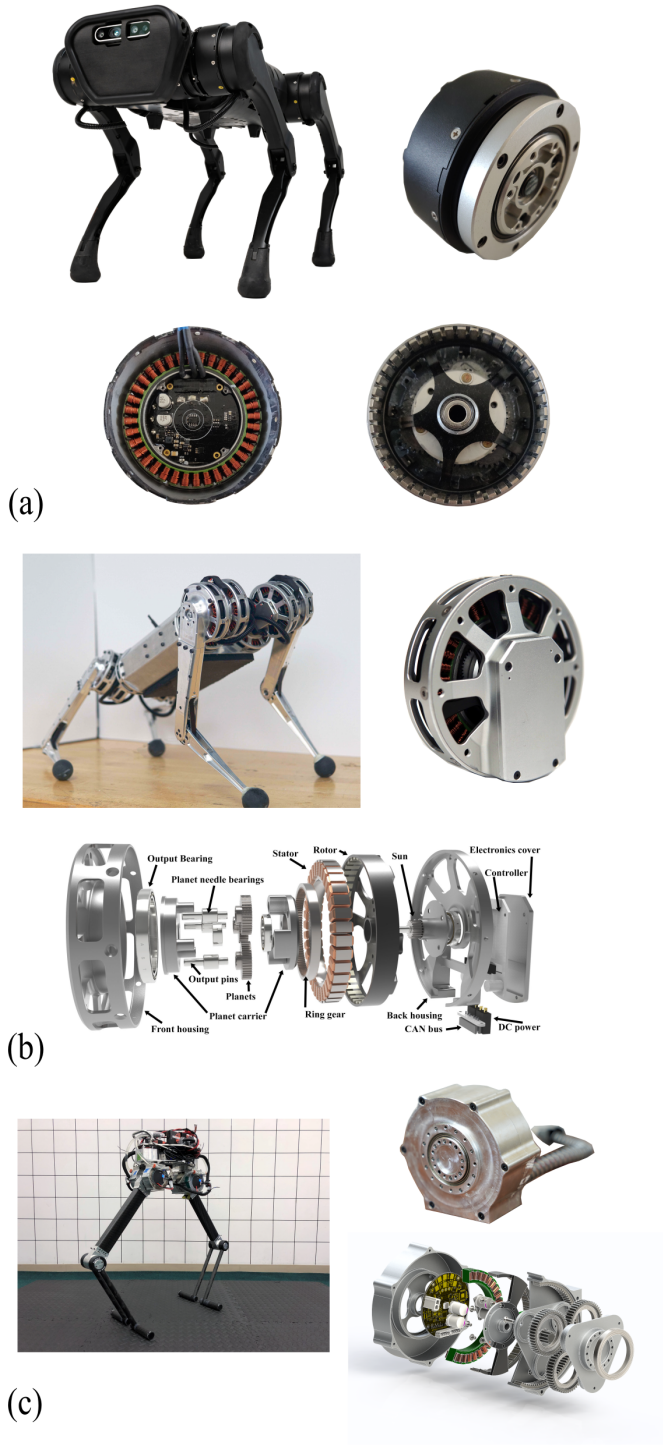

Figure 1.10: State-of-the-art quasi-direct-drive actuators with integrated power electronics: (a) Unitree Robotics A1 motor [54] (b) MIT Mini Cheetah [55] (c) Water-cooled BEAR actuator module [56]

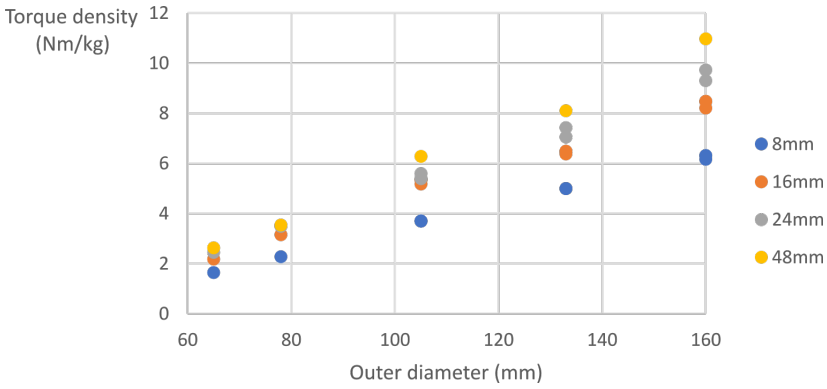

Figure 1.11: Torque density versus outer diameter for various motor stack lengths. Data was obtained form a series of inner rotor permanent magnet synchronous machines [58].

it becomes more difficult to use the motor current for output torque estimation [60]. It is currently an active research topic to cope with the torque ripple either via design measures [61, 62] or control methods [60, 63].

Driven by the goal to create the ideal torque source which is free of compliance and backlash, which is perfectly backdrivable, robust to collisions and capable of delivering sufficient torque even at very high speeds, researcher have come up with the concept of direct-drive actuators [64], this can be seen as a special subset of quasi-direct-drive actuators in which the electric motor is directly coupled to the output link without transmission as illustrated in Fig. 1.7. Given its promising features, research into this actuator architecture is almost already as old as the first full-electric industrial robot. Already in the 1980s, fully direct-drive robots have been developed primarily for laser-cutting and high-speed assembly operations [64]. Soon the limitations of this actuator technology also became clear: their extremely low volumetric and gravimetric torque-density [64, 65] which is inherently limited by magnetic saturation and material temperature limits [11]. Especially in serial linkage robotics where the actuators have to compensate for the weight of the robot linkages, gravimetric torque density is an important metric because a heavier motor increases the torque requirements, resulting in the need for larger motors which are again heavier. Also volumetric torque density is important to give the robot a sufficiently large workspace. If the diameter of the motor becomes too large with respect to the link it drives, the robots workspace becomes too small to perform useful tasks. Given their limitation, direct-drive actuators have mainly been applied in parallel linkage robots like delta-robots or serial linkage robots that don't require gravity compensation such as SCARA robots as illustrated in Fig. 1.12. More recently, direct-drive actuators have also been

(a) (b)

Figure 1.12: (a) A delta robot based on direct-drive actuators [66] (b) A SCARA robot concept based on direct-drive actuators [67]

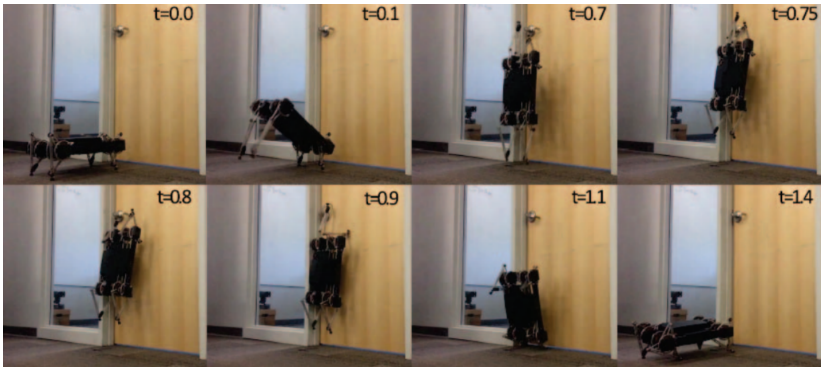

Figure 1.13: A direct-drive robot performing a dynamic door opening manoeuvre. Due to geometric limitation of the robot this would not be possible if a quasi-static control method was used [68].

used in a small legged quadruped robot that has demonstrated its capabilities in a door-opening task as shown in Fig. 1.13 [68]. It managed to open the door via a dynamic manoeuvre by relying on the inherent torque sensing capabilities of the direct-drive actuators and its thermal inertia to overcome its continuous torque limits. This would not have been possible by relying on pure quasi-static control methods because the robot is too small to reach the door handle. The same authors have proven in [69] the superior performance of direct-drive actuators in proprioceptive tasks, i.e. tasks in which sensing of the interaction forces of the environment is used to adjust the actuator torque.

Another aspect in favour of direct-drive actuators is noise. It is well known

Table 1.2: Qualitative comparison of actuator architectures [70]

Property	**High gear ratio**	**Series Elastic**	**Variable Stiffness**	**Quasi-Direct-Drive**	**Direct-Drive**
Torque density	+ +	+	+	-	- -
Output speed	- -	-	+	+	+ +
Robustness	- -	+ +	+ +	-	+ +
Backdrivability	- -	- -	-	+	+ +
Complexity	+	-	- -	+	+ +

that gearboxes represent an important source of noise [40] which may be a serious concern when operating in the close neighbourhood of humans.

In Table 1.2 the discussed actuator architectures are qualitatively compared based on five important design requirements in novel service robot applications. From the discussion above it is clear that quasi-direct-drive actuators exhibit several features that make them inherently more suitable for use in novel service robots that have to operate in changing, unstructured and/or unknown environments. Their low torque density is currently a major hurdle in the further proliferation of quasi-direct-drive actuators. Realizing quasi-direct-drive actuators with a higher torque density enables to significantly improve the performance of existing robots and would open up completely new applications. The impact that such actuator technology can bring was the main motivation for the work in this dissertation.

1.3 Torque Density of Quasi-Direct-Drive Actuators

Motivated by the potential impact that higher torque density quasi-direct-drive actuators can have, this research topic has already attracted the attention of numerous researchers in the past. This section wants to provide an overview of the most important pathways that have been studied. The largest body of efforts to increase the torque density of electric motors focuses mainly on energy conversion [71, 72] and transportation applications [73, 74]. Because the boundary conditions for the integration and operation of the electric motor in a robotic application are very different [75], this section focuses on the state-of-the-art techniques to increase the torque density of electric motors in this application area.

1.3.1 Electromagnetic Design Measures

The first all-electric industrial robot used Direct Current (DC) motors. Since then, due to their low overload capability and need for frequent maintenance, they have been replaced by Permanent Magnet Synchronous Motors (PMSMs) [75]. The remainder of this work will focus on this electric motor technology. The torque T of a PMSM is proportional to the current I through the stator winding and the magnetic flux ψ produced by the permanent magnets coupled with the winding:

$$T \sim I \cdot \psi$$

For a given electromagnetic motor design and winding connection, the coupled magnetic flux ψ of a PMSM is fixed and the torque can only be increased by increasing the current I. However, the laws of physics inherently limit the torque production capability of an electric motor [11] i.e. there is an upper limit for the current I. First, due to the Joule effect, heat is generated in the windings, resulting in increased temperatures in different parts of the motor. Typically, the motor winding [76] and the permanent magnets [77] are the components which are most susceptible to this temperature rise. Hence their temperature limit imposes a limit to the Root-Mean-Square (RMS) current that can be maintained by the motor in thermal steady-state. Second, the leakage flux of the current can cause magnetic saturation of the main flux path. This reduces the flux produced by the permanent magnets that is coupled with the stator winding. This reduces the motor's torque constant, the torque produced per unit of current and more current is needed to produce the same increment of torque. A motor operating in heavy saturation produces exponentially more heat and typically it is not possible to achieve thermal steady-state in this situation. Finally, the peak current should be limited to avoid demagnetization of the permanent magnets. Moreover, they are more prone to demagnetization at elevated temperatures. The current may not exceed the demagnetizing current level at any time.

Most research efforts focus on increasing the continuous current rating since it is generally accepted that operation in heavy saturation or demagnetization has to be avoided [78]. In [78–81], the authors relied on cobalt-iron alloy core to achieve a high torque density since it has a higher saturation flux density compared to conventional electrical steel grades. In [82], a Yokeless and Segmented Armature (YASA) Axial Flux PMSM (AFPMSM) was proposed for an exoskeleton application. Since the magnetic flux in the core of this electrical machine topology is mainly unidirectional, grain-oriented electrical steel can be used which also allows a higher saturation flux density. Fig. 1.14 shows a transverse flux electrical machine that was proposed for robotic applications because of its high torque density [83]. It was shown that the torque density increases with the number of poles.

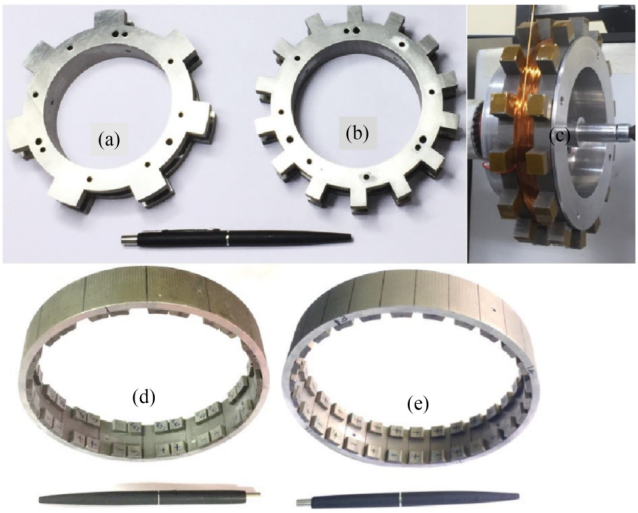

Figure 1.14: A transverse flux permanent magnet machine design for a robotic space application [81]. (a-b) two stator variant; (c) winding process of single phase (d-e) two rotor variants

1.3.2 Thermal Design Measures

Instead of improving the electromagnetic motor design, an enhanced thermal management of the motor allows to dissipate the generated heat more efficiently resulting in larger continuous current or torque capability. In [56, 84, 85] stator winding encapsulation was proposed to improve the heat transfer in the stator. Active cooling on the other hand can increase the dissipated heat by several orders of magnitude with respect to passive cooling. In Fig. 1.15, forced air-cooling was realised by the addition of a small fan typically found in large scale electronics [86, 87]. Liquid cooling can further help to improve heat dissipation. Typically a water jacket is mounted around the motor housing [88–90] or at an axial end-face as in Fig. 1.10c [56]. However, the addition of a liquid cooling system also adds significantly more weight in comparison to forced air cooling due to the need for a radiator, pump and hoses. In Fig. 1.17 a motor driver with and without liquid cooling for a motor in a humanoid robot are compared [43]. Through loss reduction by proper material choice and improving the thermal design, comparable performances could be obtained without the need for water cooling. Despite the effectiveness of the mentioned techniques, the torque density is still limited by the low slot fill factor and thermal conductivity of the winding body as is often found in small electric motors for robotic applications. Either a distributed winding is used, exhibiting typical fill factor between 35-45% [91], or a concentrated fractional slot winding is used having a higher fill factor. However it is still limited to 50 - 65 % [91] in

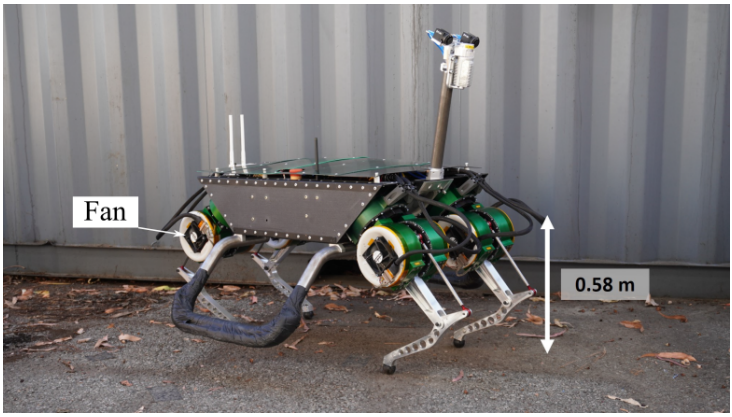

Figure 1.15: A legged quadruped robot using fan-cooled quasi-direct-drive actuators [86]

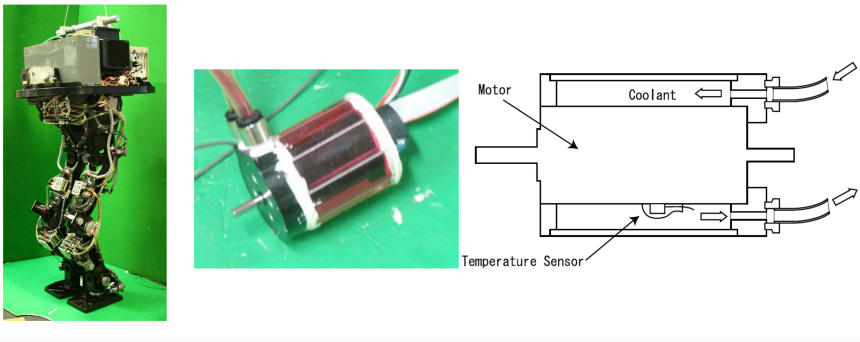

Figure 1.16: A legged quadruped robot using fan-cooled quasi-direct-drive actuators [86]

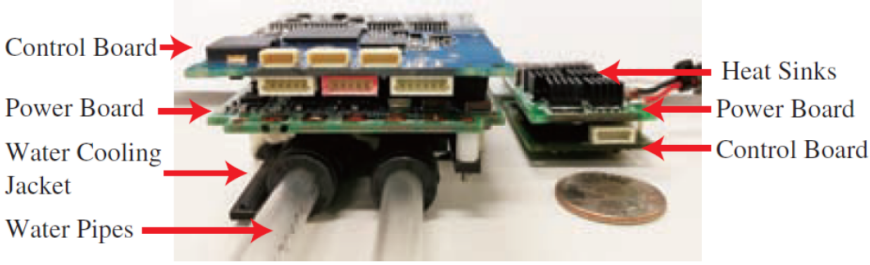

Figure 1.17: Comparison of a motor driver with and without water cooling for a humanoid robot applications [43]. (left) with water cooling (right) without water cooling

large volume manufacturing processes that rely on needle or flyer winding of a full stator [59, 92]. Although potting and encapsulation techniques have been proposed to improve the equivalent thermal conductivity of the winding body, the insulation enamel and potting material are still an important bottleneck in the heat dissipation path [93, 94].

In Fig. 1.10 several academic and commercial examples of quasi-direct-drive actuators are shown. Motivated by the need for compactness and a high volumetric torque density [21, 55], the inverter is integrated in the actuator. This is often referred to as Integrated Motor Drive (IMD) [95]. Hence it is no longer a question whether the drive should be integrated in the actuator, but rather how should the drive be integrated in the actuator to maximize the torque density. The high temperature of the motor windings often constitutes an important challenge when integrating the power electronics because the semiconductor junction temperature typically has a lower temperature limit [95]. In [96] for example, the power electronics switches already reach their temperature limit before the motor windings do. This prevents the motor to reach its full potential. In [55], the motor windings reach their temperature limit first, implying that the drive electronics were oversized. Both examples illustrate the difficulty to realize a well-balanced thermo-mechanical integration. Despite the fact that [97] already stressed the importance of a balanced thermo-mechanical integration in order to achieve a high volumetric torque density, only very few concepts that tightly integrate motor and power electronics for quasi-direct-drive robot actuators have been evaluated yet. These are given in Fig. 1.10.

1.4 Research Objective and Challenges

This work aims to design and evaluate an Integrated Motor Drive concept for a quasi-direct-drive robotic actuator, and increase its torque density by addressing three key challenges:

1. *The poor fill factor and thermal conductivity of a round enamelled copper wire winding*

   Since the torque density is inherently limited by the physical material properties and manufacturing processes of round enamelled copper wire, a fundamentally different conductor is studied in this work: anodized aluminum foil. A thin aluminum-oxide layer constitutes the electrical insulation of this foil conductor. Since this is a ceramic material, it exhibits a higher thermal conductivity [98] and temperature limit [99] in comparison to organic insulation materials. Additionally, the gravimetric density of aluminum is approximately three times lower compared to

copper, making this type of conductor an interesting candidate for a high torque density electric motor. To the author's best knowledge, the use of this type of conductor in a rotating electrical machine has not been reported in the scientific literature before.

2. *The mechanical challenges related to the use of anodized aluminum foil*

   There are mainly two major mechanical challenges related to the manufacturing of a rotating electrical machine with anodized aluminum foil winding. First, in robotics either internal rotor or external rotor radial flux PMSMs constitute the lion's share of electric machines used in robotics [80]. However the introduction of a foil winding in the slots of a conventional radial flux machine is not straightforward. Either the use of a segmented stator or a stator with open slots is required [100–102]. Also, in a radial flux machine with foil winding there is always some free space between the slots as a consequence of the rectangular shape of the cross-section of a stack of multiple layers of foil hence underutilizing the available slot area.

   The second mechanical challenge is related to soldering of the anodized foil. The presence of an aluminum-oxide layer makes soldering very difficult [103]. However, in many applications it is required to connect the anodized aluminum foil to another copper or aluminum conductor.

3. *Overheating due to uneven loss distribution at standstill.*

   All of the aforementioned design measures in Section 1.3 related to the thermal management focus on improving the heat dissipation under a uniform loss distribution. In novel service robotic applications relying on quasi-direct-drive actuators also a non-uniform loss distribution might arise. A typical example of such an application is a force controlled two-finger gripper [104]. When handling brittle or soft objects, the gripper should estimate and control the holding force. If the gripper uses a quasi-direct-drive actuator, this can be done by sensing and controlling the motor current [53]. However when holding an object with maximum force, the motor operates at quasi-standstill and generates its rated torque. The dissipated conduction loss in one of the three phases is then two times higher for the worst-case rotor position when compared to operation at non-zero speed for the same torque [105, 106]. This can lead to local overheating of the winding and hence the standstill torque should be derated.

Designing an IMD requires a truly multidisciplinary approach [107] involving mechanical, thermal, control, electronics and electromagnetic aspects of both the electric motor and the power electronics. The above mentioned

challenges focus on the electric motor of the IMD concept. Specific challenges related to the power electronics and its control were mentioned in [108–110], where the influence of the Pulse Width Modulation (PWM) strategy on the DC-link capacitor requirements was studied to reduce the volume occupied by the DC-link. In [111], a current control strategy was developed to eliminate the higher order harmonics in the stator current due to a non-sinusoidal back-emf. Although the author has substantially contributed to this research, this dissertation does not encompass these aspects since a different IMD concept was considered there which was tailored to the needs of a transportation application.

Although it was shown recently that advanced integration of the gears and electric motor might result in a very compact and high torque density actuator as well [112], the gears were not included in the IMD concept in order to limit the design complexity.

1.5 Thesis Outline

This chapter started by motivating the need for robots that are capable of dealing with uncertain, unstructured and changing environments, consequently the fitness of several actuator architectures to fulfil the needs in these novel applications was evaluated. It was concluded that a quasi-direct-drive actuator architecture is a promising candidate to realize a sensitive, robust, backdrivable, dynamic and cost-efficient robotic actuator. However, its low torque density is currently a limiting factor for the robot's performance. Subsequently, factors influencing the torque density of the electric motor and its power electronics were identified in order to derive the challenges that will be tackled in this dissertation. In Fig. 1.18 a schematic overview of the outline of this thesis is given which links each chapter to a specific research challenge mentioned in Section 1.4.

In Chapter 2, an integrated motor drive concept for a quasi-direct-drive actuator is introduced and evaluated of which an exploded view of this concept is shown in Fig. 1.18. This chapter starts by deriving the requirements of an IMD for a quasi-direct-drive robotic actuator and motivates the design choices to meet these specification for the main design aspects in an IMD. Subsequently, the realized IMD hardware prototype is presented and thoroughly characterized. The experimental data is used to validate a 3D thermal Finite Element (FE) model which is used to evaluate the torque density of the realized concept. Finally, the concept is benchmarked against the State-of-the-Art. The detailed evaluation of the IMD concept in this chapter will help designers in the future to make better informed decisions with respect to which integration concept best fulfils their requirements.

Chapter 3 and the following chapters are each based on one article published during this dissertation. In this chapter, the limited fill factor and thermal conductivity achieved in windings with round enamelled copper wire are improved by using anodized aluminum foil. This type of conductor is used for the electric motor in the IMD described in Chapter 2. Both the fill factor and thermal properties of a single concentrated coil and a complete motor are evaluated experimentally and compared to an electromagnetically identical coil and motor with round enamelled copper wire. Eventually the gravimetric and volumetric torque density is determined experimentally for both types of conductor. This is the first description of the use of anodized aluminum foil in a rotating electrical machine in the international scientific literature.

The use of a novel type of conductor requires tailored manufacturing processes. In Chapter 4 the mechanical challenges related to the use of anodized aluminum foil in a rotating electrical machine are tackled. To overcome the drawbacks related to the use of a foil winding in a radial flux machine, a Yokeless and Segmented Armature Axial Flux Permanent Magnet Synchronous Machine (AFPMSM) topology is considered in this work. Since it is inherently segmented, it allows winding of the coils outside the motor and it eliminates free space between adjacent slots allowing a high fill factor.

To address the issue of establishing reliable electrical connections to anodized aluminum foil, two interconnection methods were studied in this work.

Finally, in Chapter 5, the overheating due to an uneven loss distribution at standstill is addressed. Although this is a known problem in literature, there is a lack of design measures to overcome this problem. This work aims to provide insight in the heat transfer in an electric motor under an uneven loss distribution by developing an experimentally validated thermal model that allows to study the influence of several design parameters on the heat transfer in case of an uneven loss distribution. This knowledge forms the basis for the development of design measures to mitigate overheating.

Chapter 6 concludes this dissertation by providing a concrete answer to the challenges mentioned in Section 1.4 and directions for future research are presented.

1.6 Research Contributions

This section describes the contributions to the State-of-the-Art. Although the main goal of this dissertation is to advance the State-of-the-Art in the field of robotic actuators by addressing the challenges mentioned in Section 1.4, the created knowledge in this dissertation has a much broader and more general impact as will be explained in the following:

1. A yokeless and segmented armature, axial flux permanent magnet

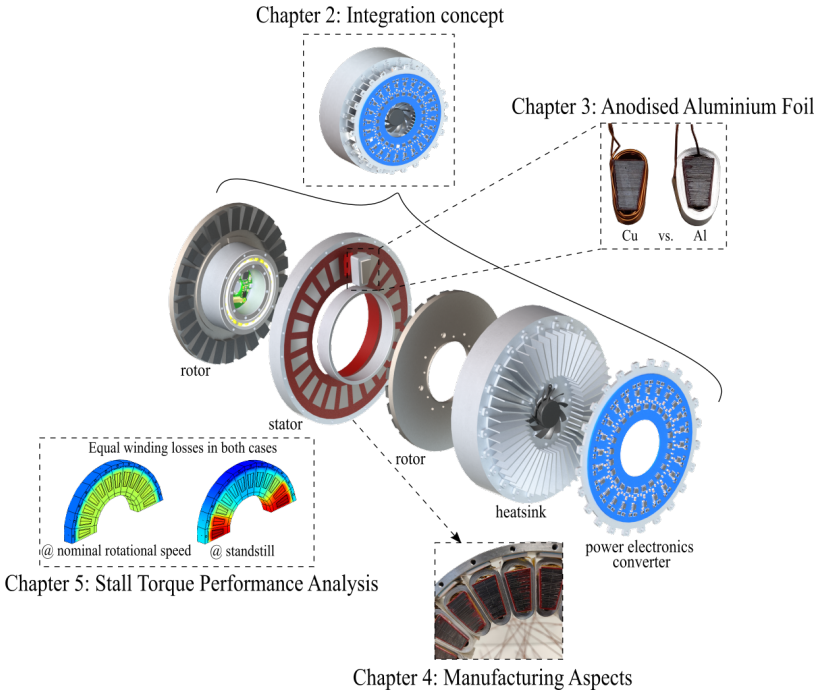

Figure 1.18: Exploded view of the proposed integration concept illustrating graphically the outline of this thesis.

synchronous machine with anodized aluminum foil winding with a higher torque density compared to an electromagnetically identical machine with round enamelled copper wire was designed, build and characterised. This is the result of the higher thermal conductivity, fill factor and lower mass density of the anodized aluminum foil. This is a distinct contribution to the State-of-the-Art as it is the first description of the usage of this type of conductor in a rotating electrical machine. The generated knowledge in this work allows to identify in which applications -apart from robotic actuators- anodized aluminum foil might outperform existing conductor technology.

2. A finite element method based, three dimensional thermal simulation model was introduced, allowing *to simulate the spatial temperature distribution in a YASA AFPMSM with anodized aluminum foil winding and in an electromagnetically identical machine with round enamelled copper wire winding*. The simulation results agreed well with experimental measurements which gives confidence in the prediction performance of the model. This allows to use the model to analyse the impact of design parameters on the performance and in particular the torque density. This

analysis can be valuable in future designs.

3. An integrated motor drive was designed, built and characterised. It consists of a yokeless and segmented armature axial flux permanent magnet synchronous machine, a 24-phase voltage source inverter which allows to supply each of the 24 slots individually, and a shared fan-heatsink combination for cooling. It is the first realization and evaluation of this integration concept in literature, demonstrating the feasibility of the concept.

4. A finite element method based, three dimensional thermal simulation model was introduced, allowing *to simulate the spatial temperature distribution in the integrated modular motor drive*. The simulation model allows to study the interaction of the losses generated by the electric motor and the losses generated by the power electronic switches. The simulation results agreed well with experimental measurements which gives confidence in the prediction performance of the model. This allows to use the model to analyse the impact of design parameters on the performance and in particular the torque density, providing valuable guidelines for future designs.

5. A finite element method based, three dimensional thermal simulation model was developed, allowing *to simulate the spatial temperature distribution in a yokeless and segmented armature, axial flux permanent magnet synchronous machine under uneven loss distribution*. The simulation results agreed well with experimental measurements which gives confidence in the prediction performance of the model. This allows to use the model to analyse the impact of design parameters on the performance and in particular the torque density at standstill. Apart from the non-uniform heating at standstill which was the motivation for this research as this issue might arise in novel robotic applications. Also in other applications an uneven loss distribution might occur e.g. in case of a voltage unbalance in grid supplied electric motors and in case of a turn-to-turn fault generating a local loss concentration.

These contributions represent a small step on the road towards high torque density quasi-direct-drive actuators which might help to realize robot that are capable to enter the unstructured, changing and/or unknown world. By doing so they will fill the gap in the future labour market and support a prosperous society.

1.7 Scientific Publications

The research results obtained in the framework of this dissertation have been the subject of a peer review process conducted by international experts in the field. A list of publications is given below:

1.7.1 International SCI Journals

1. **J. Van Damme**, H. Vansompel, and G. Crevecoeur, "Anodized aluminum foil winding axial flux machine for direct-drive robotic applications," *IEEE Transaction on Industrial Electronics*, vol. 70, no. 10, pp. 10409-10419, 2023

2. **J. Van Damme**, H. Vansompel, and G. Crevecoeur, "Stall Torque Performance Analysis of a YASA Axial Flux Permanent Magnet Synchronous Machine," *Machines*, vol. 11, no. 4, p. 487, 2023

3. L. Verkroost, A. Vande Ghinste, K. Vanthuyne, **J. Van Damme**, F. De Belie, P. Sergeant, H. Vansompel, "Multi-agent voltage balancing in modular motor drives with series-connected power electronic converters," *IET Power Electronics*, 2023

4. L. Verkroost, **J. Van Damme**, D. Bozalakov, F. De Belie, P. Sergeant, and H. Vansompel, "Simultaneous DC-link and stator current ripple reduction with interleaved carriers in multiphase controlled integrated modular motor drives," *IEEE Transactions on Industrial Electronics*, vol. 68, no. 7, pp. 5616-5625, 2021

5. H. Li, **J. Van Damme**, C. Ma, J. Melkebeek, and F. De Belie, "A geometrical interpretation of current transient responses to predict current gradients for IPMSM model predictive control," *IEEE Transactions on Industrial Electronics*, vol. 68, no. 11, pp. 10498-10509, 2021

1.7.2 Proceedings of International Conferences

1. **J. Van Damme**, H. Vansompel, G. Crevecoeur, K. Faes, R. Nunes and R. Tack, "Anodised Aluminium Foil Winding Axial Flux Machine for (Quasi-)Direct-Drive Robotic Applications: Preliminary Design and Manufacturing," 2022 *12th International Electric Drives Production Conference (EDPC)*, Regensburg, Germany, 2022, pp. 1-9

2. **J. Van Damme**, H. Vansompel and G. Crevecoeur, "Performance comparison of Axial Flux PM machine with Anodised aluminum Foil and Round Copper Wire," 2022 *International Conference on Electrical Machines (ICEM)*, Valencia, Spain, 2022, pp. 1397-1403

3. **J. Van Damme**, L. Verkroost, H. Vansompel, F. De Belie and P. Sergeant, "A holistic DC link architecture design method for multiphase integrated modular motor drives," 2019 *IEEE International Electric Machines & Drives Conference (IEMDC)*, San Diego, CA, USA, 2019, pp. 1593-1598

4. B. Mehdizadeh Gavgani, T. Staessens, **J. Van Damme**, J. De Kooning, D. Bozalakov, L. Vandevelde, and G. Crevecoeur, "Exploiting Bidirectional Power Flow Control to Capture Wind Gust Power in Small and Medium Wind Turbines," 2021 *The 9th Renewable Power Generation Conference (RPG Dublin Online 2021)*, pp. 204-209

5. L. Verkroost, **J. Van Damme**, H. Vansompel, F. De Belie and P. Sergeant, "Module Connection Topologies and Interleaving Strategies for Integrated Modular Motor Drives," 2019 *IEEE International Electric Machines & Drives Conference (IEMDC)*, San Diego, CA, USA, 2019, pp. 559-564

References

[1] J. Wallen, "The history of the industrial robot," Department of Electrical Engineering, Linkopings University, Tech. Rep., 2008.

[2] D. Marshall and N. Chambers, "Rise of the robot," *ABB Review*, vol. 2, pp. 24–31, 2014.

[3] B. Siciliano and O. Khatib, Eds., *Springer handbook of robotics*, 2nd ed., ser. Springer Handbooks. Basel, Switzerland: Springer International Publishing, Jul. 2016.

[4] K. De Backer, T. DeStefano, C. Menon, and J. Ran Suh, "Industrial robotics and the global organisation of production," Organisation for Economic Co-Operation and Development (OECD), Tech. Rep., Feb. 2018.

[5] "World robotics report 2022," International Federation of Robotics, Tech. Rep., 2022.

[6] Population pyramid. Available at https://www.populationpyramid.net/ (accessed: 07-04-2023).

[7] N. Boysen, R. de Koster, and F. Weidinger, "Warehousing in the e-commerce era: A survey," *European Journal of Operational Research*, vol. 277, no. 2, pp. 396–411, 2019.

[8] H. Sahin and L. Guvenc, "Household robotics: autonomous devices for vacuuming and lawn mowing [applications of control]," *IEEE Control Systems Magazine*, vol. 27, no. 2, pp. 20–96, 2007.

[9] P. M. Wensing, A. Wang, S. Seok, D. Otten, J. Lang, and S. Kim, "Proprioceptive actuator design in the mit cheetah: Impact mitigation and high-bandwidth physical interaction for dynamic legged robots," *IEEE Transactions on Robotics*, vol. 33, no. 3, pp. 509–522, 2017.

[10] H. Zhu, C. Nesler, N. Divekar, M. T. Ahmad, and R. D. Gregg, "Design and validation of a partial-assist knee orthosis with compact, backdrivable actuation," in *2019 IEEE 16th International Conference on Rehabilitation Robotics (ICORR)*, 2019, pp. 917–924.

[11] G. Ficht and S. Behnke, "Bipedal humanoid hardware design: a technology review," *Current Robotics Reports*, vol. 2, no. 2, pp. 201–210, Apr. 2021.

[12] M. Smets, "A field evaluation of arm-support exoskeletons for overhead work applications in automotive assembly," *IISE Transactions on Occupational Ergonomics and Human Factors*, vol. 7, no. 3-4, pp. 192–198, Mar. 2019.

[13] F. Longo, A. Padovano, V. Solina, V. D'Augusta, S. Venzl, R. Calbi, M. Bartuni, O. Anastasi, and R. Diaz, "Human ergonomic simulation to support the design of an exoskeleton for lashing/de-lashing operations of containers cargo," *Procedia Computer Science*, vol. 200, pp. 1894–1902, 2022.

[14] Z. Zhu, A. Dutta, and F. Dai, "Exoskeletons for manual material handling - a review and implication for construction applications," *Automation in Construction*, vol. 122, p. 103493, 2021.

[15] M. A. Gull, S. Bai, and T. Bak, "A review on design of upper limb exoskeletons," *Robotics*, vol. 9, no. 1, 2020.

[16] B. Laschowski and J. McPhee, "Energy-Efficient Actuator Design Principles for Robotic Leg Prostheses and Exoskeletons: A Review of Series Elasticity and Backdrivability," *Journal of Computational and Nonlinear Dynamics*, vol. 18, no. 6, 04 2023.

[17] S. Yu, T.-H. Huang, X. Yang, C. Jiao, J. Yang, Y. Chen, J. Yi, and H. Su, "Quasi-direct drive actuation for a lightweight hip exoskeleton with high backdrivability and high bandwidth," *IEEE/ASME Transactions on Mechatronics*, vol. 25, no. 4, pp. 1794–1802, 2020.

[18] C. Hatzfeld and T. A. Kern, Eds., *Engineering Haptic Devices*. Springer London, 2014.

[19] M. H. Raibert, *Legged Robots That Balance*, ser. Artificial Intelligence Series. London, England: MIT Press, 2000.

[20] Anybotics ag. Available at https://www.anybotics.com/ (accessed: 24-05-2023).

[21] S. Kalouche, "Design for 3d agility and virtual compliance using proprioceptive force control in dynamic legged robots," Master's thesis, Carnegie Mellon University, Pittsburgh, PA, August 2016.

[22] G. Kenneally, A. De, and D. E. Koditschek, "Design principles for a family of direct-drive legged robots," *IEEE Robotics and Automation Letters*, vol. 1, no. 2, pp. 900–907, 2016.

[23] "blind" cheetah 3 robot can climb stairs littered with obstacles. Available at https://news.mit.edu/2018/blind-cheetah-robot-climb-stairs-obstacles-disaster-zones-0705 (accessed: 24-05-2023).

[24] B. Vanderborght, A. Albu-Schaeffer, A. Bicchi, E. Burdet, D. Caldwell, R. Carloni, M. Catalano, O. Eiberger, W. Friedl, G. Ganesh, M. Garabini, M. Grebenstein, G. Grioli, S. Haddadin, H. Hoppner, A. Jafari, M. Laffranchi, D. Lefeber, F. Petit, S. Stramigioli, N. Tsagarakis, M. Van Damme, R. Van Ham, L. Visser, and S. Wolf, "Variable impedance actuators: A review," *Robotics and Autonomous Systems*, vol. 61, no. 12, pp. 1601–1614, 2013.

[25] J. C. Arevalo, D. Sanz-Merodio, M. Cestari, and E. Garcia, "Identifying ground-robot impedance to improve terrain adaptability in running robots," *International Journal of Advanced Robotic Systems*, vol. 12, no. 1, p. 1, Jan. 2015.

[26] M. Chignoli, D. Kim, E. Stanger-Jones, and S. Kim, "The mit humanoid robot: Design, motion planning, and control for acrobatic behaviors," in *2020 IEEE-RAS 20th International Conference on Humanoid Robots (Humanoids)*, 2021, pp. 1–8.

[27] M. Grebenstein, A. Albu-Schaffer, T. Bahls, M. Chalon, O. Eiberger, W. Friedl, R. Gruber, S. Haddadin, U. Hagn, R. Haslinger, H. Hoppner, S. Jorg, M. Nickl, A. Nothhelfer, F. Petit, J. Reill, N. Seitz, T. Wimbock, S. Wolf, T. Wusthoff, and G. Hirzinger, "The dlr hand arm system," in *2011 IEEE International Conference on Robotics and Automation*, 2011, pp. 3175–3182.

[28] S. Haddadin, A. De Luca, and A. Albu-SchÃ¤ffer, "Robot collisions: A survey on detection, isolation, and identification," *IEEE Transactions on Robotics*, vol. 33, no. 6, pp. 1292–1312, 2017.

[29] J. Zhu, C. Jiao, I. Dominguez, S. Yu, and H. Su, "Design and backdrivability modeling of a portable high torque robotic knee prosthesis with intrinsic compliance for agile activities," *IEEE/ASME Transactions on Mechatronics*, vol. 27, no. 4, pp. 1837–1845, 2022.

[30] E. J. Rouse, L. M. Mooney, and H. M. Herr, "Clutchable series-elastic actuator: Implications for prosthetic knee design," *The International Journal of Robotics Research*, vol. 33, no. 13, pp. 1611–1625, 2014.

[31] B. E. Lawson, J. Mitchell, D. Truex, A. Shultz, E. Ledoux, and M. Goldfarb, "A robotic leg prosthesis: Design, control, and implementation," *IEEE Robotics and Automation Magazine*, vol. 21, no. 4, pp. 70–81, 2014.

[32] A. F. Azocar, L. M. Mooney, J.-F. Duval, A. M. Simon, L. J. Hargrove, and E. J. Rouse, "Design and clinical implementation of an open-source bionic leg," *Nature Biomedical Engineering*, vol. 4, no. 10, pp. 941–953, Oct. 2020.

[33] M. Tran, L. Gabert, M. Cempini, and T. Lenzi, "A lightweight, efficient fully powered knee prosthesis with actively variable transmission," *IEEE Robotics and Automation Letters*, vol. 4, no. 2, pp. 1186–1193, 2019.

[34] A. Singh, N. Kashiri, and N. Tsagarakis, "Design of a quasi-direct-drive actuator for dynamic motions," *Proceedings*, vol. 64, no. 1, 2020.

[35] M. Hutter, "Starleth and co.. design and control of legged robots with compliant actuation," Doctoral Thesis, ETH Zurich, Zurich, 2013.

[36] F. Negrello, M. Garabini, M. G. Catalano, J. Malzahn, D. G. Caldwell, A. Bicchi, and N. G. Tsagarakis, "A modular compliant actuator for emerging high performance and fall-resilient humanoids," in *2015 IEEE-RAS 15th International Conference on Robots (Humanoids)*, 2015, pp. 414–420.

[37] K. Kojima, Y. Kojio, T. Ishikawa, F. Sugai, Y. Kakiuchi, K. Okada, and M. Inaba, "Drive-train design in jaxon3-p and realization of jump motions: Impact mitigation and force control performance for dynamic motions," in *2020 IEEE/RSJ International Conference on Intelligent Robots and Systems (IROS)*, 2020, pp. 3747–3753.

[38] M. Chignoli, "Trajectory optimization for dynamic aerial motions of legged robots," Master's thesis, Massachusetts Institute of Technology, Cambridge, MA, January 2021.

[39] T. Asfour, M. Waechter, L. Kaul, S. Rader, P. Weiner, S. Ottenhaus, R. Grimm, Y. Zhou, M. Grotz, and F. Paus, "Armar-6: A high-performance humanoid for human-robot collaboration in real-world scenarios," *IEEE Robotics and Automation Magazine*, vol. 26, no. 4, pp. 108–121, 2019.

[40] P. L. Garcia, S. Crispel, E. Saerens, T. Verstraten, and D. Lefeber, "Compact gearboxes for modern robotics: A review," *Frontiers in Robotics and AI*, vol. 7, 2020.

[41] A. Albu-Schäffer, S. Haddadin, C. Ott, A. Stemmer, T. Wimböck, and G. Hirzinger, "The dlr lightweight robot – design and control concepts for robots in human environments," *INDUSTRIAL ROBOT-AN INTERNATIONAL JOURNAL*, vol. 34, no. 5, pp. 376–385, March 2007.

[42] H. Wittel, *Roloff/Matek machine-onderdelen: theorieboek*, 2013.

[43] F. Sugai, K. Kojima, Y. Kakiuchi, K. Okada, and M. Inaba, "Design of tiny high-power motor driver without liquid cooling for humanoid jaxon," in *2018 IEEE-RAS 18th International Conference on Humanoid Robots (Humanoids)*, 2018, pp. 1059–1066.

[44] F. Ostyn, T. Lefebvre, B. Vanderborght, and G. Crevecoeur, "Overload clutch design for collision tolerant high-speed industrial robots," *IEEE Robotics and Automation Letters*, vol. 6, no. 2, pp. 863–870, 2021.

[45] J. Englsberger, A. Werner, C. Ott, B. Henze, M. A. Roa, G. Garofalo, R. Burger, A. Beyer, O. Eiberger, K. Schmid, and A. Albu-Schaffer, "Overview of the torque-controlled humanoid robot toro," in *2014 IEEE-RAS International Conference on Humanoid Robots*, 2014, pp. 916–923.

[46] F. Ostyn, B. Vanderborght, and G. Crevecoeur, "Overload clutch with integrated torque sensing and decoupling detection for collision tolerant hybrid high-speed industrial cobots," *IEEE Robotics and Automation Letters*, vol. 7, no. 4, pp. 12 601–12 607, 2022.

[47] S. Wolf, O. Eiberger, and G. Hirzinger, "The dlr fsj: Energy based design of a variable stiffness joint," in *2011 IEEE International Conference on Robotics and Automation*, 2011, pp. 5082–5089.

[48] S. Wolf and G. Hirzinger, "A new variable stiffness design: Matching requirements of the next robot generation," in *2008 IEEE International Conference on Robotics and Automation*, 2008, pp. 1741–1746.

[49] T. Bacek, M. Moltedo, J. Geeroms, B. Vanderborght, C. Rodriguez-Guerrero, and D. Lefeber, "Varying mechanical compliance benefits energy efficiency of a knee joint actuator," *Mechatronics*, vol. 66, p. 102318, 2020.

[50] U. H. Lee, C.-W. Pan, and E. J. Rouse, "Empirical characterization of a high-performance exterior-rotor type brushless dc motor and drive," in *2019 IEEE/RSJ International Conference on Intelligent Robots and Systems (IROS)*, 2019, pp. 8018–8025.

[51] D. V. Gealy, S. McKinley, B. Yi, P. Wu, P. R. Downey, G. Balke, A. Zhao, M. Guo, R. Thomasson, A. Sinclair, P. Cuellar, Z. McCarthy, and P. Abbeel, "Quasi-direct drive for low-cost compliant robotic manipulation," in *2019 International Conference on Robotics and Automation (ICRA)*, 2019, pp. 437–443.

[52] F. Grimminger, A. Meduri, M. Khadiv, J. Viereck, M. Wuthrich, M. Naveau, V. Berenz, S. Heim, F. Widmaier, T. Flayols, J. Fiene, A. Badri-Sprowitz, and L. Righetti, "An open torque-controlled modular robot architecture for legged locomotion research," *IEEE Robotics and Automation Letters*, vol. 5, no. 2, pp. 3650–3657, 2020.

[53] F. Ostyn, B. Vanderborght, and G. Crevecoeur, "Design and control of a quasi-direct drive robotic gripper for collision tolerant picking at high speed," *IEEE Robotics and Automation Letters*, vol. 7, no. 3, pp. 7692–7699, 2022.

[54] Unitree robotics - story. Available at https://shop.unitree.com/pages/about-us (accessed: 16-05-2023).

[55] B. Katz, "A low cost modular actuator for dynamic robots," Master's thesis, Massachusetts Institute of Technology, Cambridge, MA, June 2018.

[56] T. Zhu, J. Hooks, and D. Hong, "Design, modeling, and analysis of a liquid cooled proprioceptive actuator for legged robots," in *2019 IEEE/ASME International Conference on Advanced Intelligent Mechatronics (AIM)*, 2019, pp. 36–43.

[57] N. Hogan, "Impedance control: An approach to manipulation," in *1984 American Control Conference*, 1984, pp. 304–313.

[58] Tecnotion direct drive torque motors. Available at https://www.tecnotion.com/products/qtl-torque-290-series/ (accessed: 24-05-2023).

[59] F. Meier, "Permanent-magnet synchronous machines with non-overlapping concentrated windings for low-speed direct-drive applications," Doctoral Thesis, KTH Stockholm, Stockholm, 2008.

[60] C. Lee, S. Bae, W. Kang, and S. Oh, "Transparent torque sensor-less impedance rendering for low-cost direct drive motor," in *2020 IEEE 16th International Workshop on Advanced Motion Control (AMC)*, 2020, pp. 291–296.

[61] M. G. Angle, J. H. Lang, J. L. Kirtley, S. Kim, and D. Otten, "Cogging torque reduction in permanent-magnet synchronous machines with skew," in *2016 XXII International Conference on Electrical Machines (ICEM)*, 2016, pp. 207–211.

[62] M. Angle, J. Lang, J. Kirtley, S. Kim, and D. Otten, "Modeling of surface permanent magnet motors with cogging and saturation effects included," *IEEE Transactions on Energy Conversion*, vol. 33, no. 4, pp. 1604–1613, 2018.

[63] M. Piccoli and M. Yim, "Anticogging: Torque ripple suppression, modeling, and parameter selection," *The International Journal of Robotics Research*, vol. 35, no. 1-3, pp. 148–160, 2016.

[64] H. Asada and K. Youcef-Toumi, *Direct-Drive Robots*. The MIT Press, 1987.

[65] F. Aghili, J. M. Hollerbach, and M. Buehler, "A modular and high-precision motion control system with an integrated motor," *IEEE/ASME Transactions on Mechatronics*, vol. 12, no. 3, pp. 317–329, 2007.

[66] Wyzo delta robot. Available at https://thewyzo.com/ (accessed: 24-05-2023).

[67] Genesis motion solutions. Available at https://genesismotion.com/products/ldx/ (accessed: 24-05-2023).

[68] T. T. Topping, G. Kenneally, and D. E. Koditschek, "Quasi-static and dynamic mismatch for door opening and stair climbing with a legged robot," in *2017 IEEE International Conference on Robotics and Automation (ICRA)*, 2017, pp. 1080–1087.

[69] G. Kenneally, W.-H. Chen, and D. Koditschek, "Actuator transparency and the energetic cost of proprioception," in *International Symposium on Experimental Robotics*, 2018.

[70] R. Zanis, E. Motoasca, and E. Lomonova, "Trade-offs in the implementation of rigid and intrinsically compliant actuators in biorobotic applications," in *2012 4th IEEE RAS and EMBS International Conference on Biomedical Robotics and Biomechatronics (BioRob)*, 2012, pp. 100–105.

[71] H. Vansompel, P. Leijnen, and P. Sergeant, "Multiphysics analysis of a stator construction method in yokeless and segmented armature axial flux pm machines," *IEEE Transactions on Energy Conversion*, vol. 34, no. 1, pp. 139–146, 2019.

[72] D. P. K. Truijen, J. D. M. De Kooning, D. Fauconnier, H. Vansompel, P. Sergeant, and K. Stockman, "Axial flux pmsm power take-off for a rim-driven contra-rotating pump-turbine," in *2022 IEEE PES 14th Asia-Pacific Power and Energy Engineering Conference (APPEEC)*, 2022, pp. 1–6.

[73] M. Galea, T. Hamiti, and C. Gerada, "Torque density improvements for high performance machines," in *2013 International Electric Machines Drives Conference*, 2013, pp. 1066–1073.

[74] P. Arumugam, E. Amankwah, A. Walker, and C. Gerada, "Design optimization of a short-term duty electrical machine for extreme environment," *IEEE Transactions on Industrial Electronics*, vol. 64, no. 12, pp. 9784–9794, 2017.

[75] S. Andersson, *Optimization of a servo motor for an industrial robot application*. Lund University, 2000.

[76] H. Vansompel and P. Sergeant, "Extended end-winding cooling insert for high power density electric machines with concentrated windings," *IEEE Transactions on Energy Conversion*, vol. 35, no. 2, pp. 948–955, 2020.

[77] H. Vansompel, P. Sergeant, and L. Dupre, "A multilayer 2d-2d coupled model for eddy current calculation in the rotor of an axial-flux pm machine," *IEEE Transactions on Energy Conversion*, vol. 27, no. 3, pp. 784–791, 2012.

[78] M. G. Angle, J. H. Lang, J. L. Kirtley, S. Kim, and D. Otten, "Optimization of surface-mount permanent magnet synchronous machines for low duty-cycle, high-torque applications," in *2017 IEEE International Electric Machines and Drives Conference (IEMDC)*, 2017, pp. 1–6.

[79] N. N. Farve, "Design of a low-mass high-torque brushless motor for application in quadruped robotics," Master's thesis, Massachusetts Institute of Technology, Cambridge, MA, June 2012.

[80] J. W. Sensinger, S. D. Clark, and J. F. Schorsch, "Exterior vs. interior rotors in robotic brushless motors," in *2011 IEEE International Conference on Robotics and Automation*, 2011, pp. 2764–2770.

[81] M. Ravichandran, V. Murali, S. Achari V.T., and C. Joseph, "A comprehensive study on transverse flux motor for direct drive low-speed spacecraft applications," *IEEE Transactions on Industrial Electronics*, vol. 68, no. 1, pp. 412–422, 2021.

[82] M. Waldhof, A. Echle, and N. Parspour, "A novel drive train concept for personalized upper body exoskeletons with a multiphase axial flux machine," in *2019 IEEE International Electric Machines and Drives Conference (IEMDC)*, 2019, pp. 2160–2166.

[83] B. Kaiser and N. Parspour, "Transverse flux machine-a review," *IEEE Access*, vol. 10, pp. 18 395–18 419, 2022.

[84] J. Hollerbach, I. Hunter, J. Lang, S. Umans, R. Sepe, E. Vaaler, and I. Garabieta, "The mcgill/mit direct drive motor project," in *[1993] Proceedings IEEE International Conference on Robotics and Automation*, 1993, pp. 611–617 vol.2.

[85] T. Elery, S. Rezazadeh, C. Nesler, and R. D. Gregg, "Design and validation of a powered knee ankle prosthesis with high-torque, low-impedance actuators," *IEEE Transactions on Robotics*, vol. 36, no. 6, pp. 1649–1668, 2020.

[86] J. Nicholson, J. Jasper, A. Kourchians, G. McCutcheon, M. Austin, M. Gonzalez, J. Pusey, S. Karumanchi, C. Hubicki, and J. Clark, "Llama: Design and control of an omnidirectional human mission scale quadrupedal robot," in *2020 IEEE/RSJ International Conference on Intelligent Robots and Systems (IROS)*, 2020, pp. 3951–3958.

[87] E. Walsh and R. Grimes, "Low profile fan and heat sink thermal management solution for portable applications," *International Journal of Thermal Sciences*, vol. 46, no. 11, pp. 1182–1190, 2007.

[88] J. Urata, Y. Nakanishi, K. Okada, and M. Inaba, "Design of high torque and high speed leg module for high power humanoid," in *2010 IEEE/RSJ International Conference on Intelligent Robots and Systems*, 2010, pp. 4497–4502.

[89] N. Paine and L. Sentis, "Design and comparative analysis of a retrofitted liquid cooling system for high-power actuators," *Actuators*, vol. 4, no. 3, pp. 182–202, 2015.

[90] A. Mazumdar, S. J. Spencer, C. Hobart, M. Kuehl, G. Brunson, N. Coleman, and S. P. Buerger, "Improving robotic actuator torque density and efficiency through enhanced heat transfer," in *Dynamic Systems and Control Conference*, vol. 50701. American Society of Mechanical Engineers, 2016, p. V002T26A004.

[91] A. M. EL-Refaie, "Fractional-slot concentrated-windings synchronous permanent magnet machines: Opportunities and challenges," *IEEE Transactions on Industrial Electronics*, vol. 57, no. 1, pp. 107–121, 2010.

[92] J. Hagedorn, F. S.-L. Blanc, and J. Fleischer, Eds., *Handbook of Coil Winding*. Springer Berlin Heidelberg, 2018.

[93] R. Wrobel, N. Simpson, P. H. Mellor, J. Goss, and D. A. Staton, "Design of a brushless pm starter generator for low-cost manufacture and a high-aspect-ratio mechanical space envelope," *IEEE Transactions on Industry Applications*, vol. 53, no. 2, pp. 1038–1048, 2017.

[94] S. Miersch, R. Schubert, thomas schuhmann, and M. Lindner, "Development of polymer-ceramic composite materials for the winding insulation of highly utilized and energy-efficient electrical machines," *TechRXiv Preprint*, 4 2023.

[95] T. M. Jahns and H. Dai, "The past, present, and future of power electronics integration technology in motor drives," *CPSS Transactions on Power Electronics and Applications*, vol. 2, no. 3, pp. 197–216, 2017.

[96] Benjamin katz - mit - blogpost. Available at https://build-its-inprogress.blogspot.com/2018/ (accessed: 16-05-2023).

[97] R. Wrobel, "A technology overview of thermal management of integrated motor drives- electrical machines," *Thermal Science and Engineering Progress*, vol. 29, p. 101222, 2022.

[98] N. Simpson, R. Wrobel, and P. H. Mellor, "Estimation of equivalent thermal parameters of impregnated electrical windings," *IEEE Transactions on Industry Applications*, vol. 49, no. 6, pp. 2505–2515, 2013.

[99] S. Babicz, S. Ait-Amar Djennad, and G. Velu, "Preliminary study of using anodized aluminum strip for electrical motor windings," in *2014*

IEEE Conference on Electrical Insulation and Dielectric Phenomena (CEIDP), 2014, pp. 176–179.

[100] P. Arumugam, T. Hamiti, and C. Gerada, "Fault tolerant winding design - a compromise between losses and fault tolerant capability," in *2012 XXth International Conference on Electrical Machines*, 2012, pp. 2559–2565.

[101] C. Gerada, "Estimation of eddy current loss in semi-closed slot vertical conductor permanent magnet synchronous machines considering eddy current reaction effect," *IEEE Transactions on Magnetics*, vol. 49, no. 10, pp. 5326–5335, 2013.

[102] M. Rios and G. Venkataramanan, "Design and construction of a foil winding permanent magnet machine," in *2020 IEEE Energy Conversion Congress and Exposition (ECCE)*, 2020, pp. 2026–2033.

[103] J. D. Widmer, C. M. Spargo, G. J. Atkinson, and B. C. Mecrow, "Solar plane propulsion motors with precompressed aluminum stator windings," *IEEE Transactions on Energy Conversion*, vol. 29, no. 3, pp. 681–688, 2014.

[104] T. De Clercq, A. Sianov, and G. Crevecoeur, "A soft barometric tactile sensor to simultaneously localize contact and estimate normal force with validation to detect slip in a robotic gripper," *IEEE Robotics and Automation Letters*, vol. 7, no. 4, pp. 11 767–11 774, 2022.

[105] G. Pfaff, A. Weschta, and A. F. Wick, "Design and experimental results of a brushless ac servo drive," *IEEE Transactions on Industry Applications*, vol. IA-20, no. 4, pp. 814–821, 1984.

[106] H. Gill, "Ac servo motor system the difference between continuous ratings and holding continuous loads," Kollmorgen, Tech. Rep., 2018.

[107] B. Lemaire-Semail, N. Idir, E. Semail, and S. Harmand, "Integrated motor drive: A multidisciplinary approach," in *2022 24th European Conference on Power Electronics and Applications (EPE'22 ECCE Europe)*, 2022, pp. P.1–P.9.

[108] J. V. Damme, "Design of an integrated modular motor drive," Master's thesis, Universiteit Gent, Gent, Belgium, Juni 2018.

[109] J. Van Damme, L. Verkroost, H. Vansompel, F. De Belie, and P. Sergeant, "A holistic dc link architecture design method for multiphase integrated modular motor drives," in *2019 IEEE International*

Electric Machines and Drives Conference (IEMDC), 2019, pp. 1593–1598.

[110] L. Verkroost, J. Van Damme, H. Vansompel, F. De Belie, and P. Sergeant, "Module connection topologies and interleaving strategies for integrated modular motor drives," in *2019 IEEE International Electric Machines and Drives Conference (IEMDC)*, 2019, pp. 559–564.

[111] L. Verkroost, J. Van Damme, D. V. Bozalakov, F. De Belie, P. Sergeant, and H. Vansompel, "Simultaneous dc-link and stator current ripple reduction with interleaved carriers in multiphase controlled integrated modular motor drives," *IEEE Transactions on Industrial Electronics*, vol. 68, no. 7, pp. 5616–5625, 2021.

[112] J. Terfurth, M. Waldhof, M. Schmid, J. Weber, M. Keller, and N. Parspour, "Design and evaluation of a spatially distributed and gear-integrated transverse flux machine," *IEEE Transactions on Industrial Electronics*, vol. 70, no. 5, pp. 5065–5073, 2023.

Chapter 2

Integrated Motor Drive Concept for a Quasi-Direct-Drive Actuator

The motivations for integrating the motor and power electronics in a quasi-direct-drive actuator were already highlighted in previous chapter, more specifically in Section 1.3. Fig. 2.1 gives an overview of the most prevalent integration topologies. The choice for a certain topology is often determined by application requirements. In [1], it was already pointed out that the literature focusing on improving the torque density of quasi-direct-drive actuators is rather scarce. It is thus no surprise that the literature on the analysis of the torque density of different integration strategies is even scarcer. This chapter presents the design and evaluation of an Integrated Motor Drive (IMD) concept for a quasi-direct-drive robotic actuator. It is not the aim of this dissertation to realize an optimized IMD, but rather to evaluate experimentally the torque density of an IMD prototype, and thus its feasibility. This knowledge can support the further optimization of this prototype and help IMD designers to improve the evaluation of different integration strategies in an early design phase.

The following chapters will build upon the IMD concept presented in this chapter and focus on sub-aspects with the aim to improve the torque density.

2.1 Axial Endplate Mount IMD Design

Fig. 2.1 shows the most prevalent integration strategies for the power electronics converter and motor. In Fig. 2.1a, the converter is mounted radially on the motor's housing, this strategy is often found in automotive traction applications [3]. In the radial stator mount strategy shown in Fig. 2.1, the converter

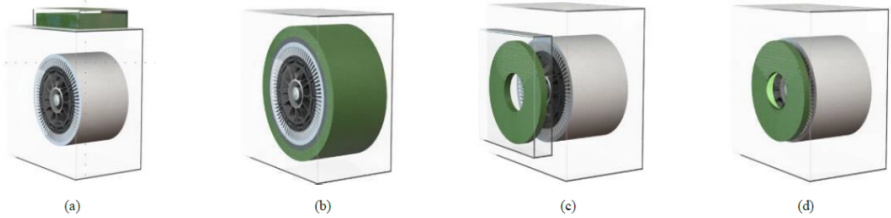

Figure 2.1: Overview of integration topologies: (a) Radial housing mount (b) Radial stator mount (c) Axial endplate mount (d) Axial stator mount [2]

is mounted on the circumference of the stator. This strategy was explored in [4, 5]. In analogy to the radial integration strategies, also axial endplate and stator mount strategies are shown in Fig. 2.1c and d respectively. These strategies have been studied for a power steering application [6] and traction motor [7] respectively. Despite the fact that several preliminary studies into different integration strategies have been performed, detailed performance analyses are scarce.

In this work, the axial endplate mount integration strategy is considered because integration should not increase the outer diameter in a quasi-direct-drive actuator. As explained in Section 1.2.3, the torque density scales proportional to the diameter for radial flux machines and proportional with the square of the diameter for axial flux machines [8]. To maximize torque density, the diameter of the motor should correspond to the maximum diameter allowed by the application. Fig. 2.2 shows an exploded view of the integration concept that is considered in this work.

The main elements of the IMD in Fig. 2.2 are: a Yokeless and Segmented Armature Axial Flux Permanent Magnet Synchronous Machine (YASA AFPMSM), a fan-heatsink combination, the power electronics drive i.e. inverter and an absolute encoder. The hardware realization of the IMD prototype on a test-bench is shown in Fig. 2.3. To facilitate measurements and debugging, the power electronics and motor are not directly electrically connected to each other but through a terminal block. This makes the photograph of the full IMD less clear, therefore 3D drawings or pictures of the subcomponents will be added separately.

The design aspects of the YASA AFPMSM are extensively discussed in Chapter 3, and its main specifications are given in Table 3.1. Its most important features are a short axial length and large diameter, it uses a fractional slot, concentrated winding with 24 slots i.e. tooth coils and 26 poles. Both terminals of every single tooth coil were made accessible for reconfiguring the winding. The winding uses round enamelled copper wire. It can be driven

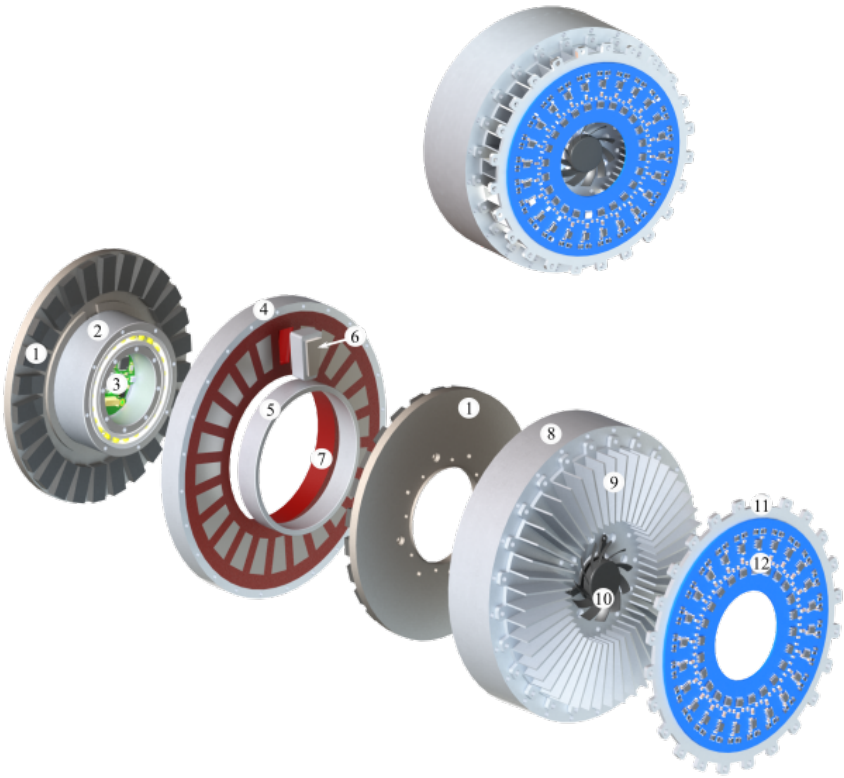

Figure 2.2: Axial endplate mount Integrated Motor Drive concept: (1) Permanent magnet rotor disc (2) Ball bearings and bearing seats (3) Absolute magnetic encoder (4) aluminum stator housing (5) Thermal end-winding interconnection ring (see Chapter 5) (6) Concentrated winding tooth coil (7) Epoxy potting (8) Housing shell (9) aluminum radially finned heatsink (10) Fan (11) aluminum PCB mounting plate (12) Power electronics drive on Insulated Metal Substrate (IMS) PCB

from a 48V DC power supply and was designed to cover a speed range from 300 to 3000 rpm by reconfiguring the winding. The remainder of this section will focus on the power electronics and fan-heatsink combination of the presented IMD concept.

2.1.1 Power Electronics

The power electronics to drive the YASA AFPMSM motor consists of 8 identical three-phase Voltage Source Inverters (VSI) connected in parallel to a com-

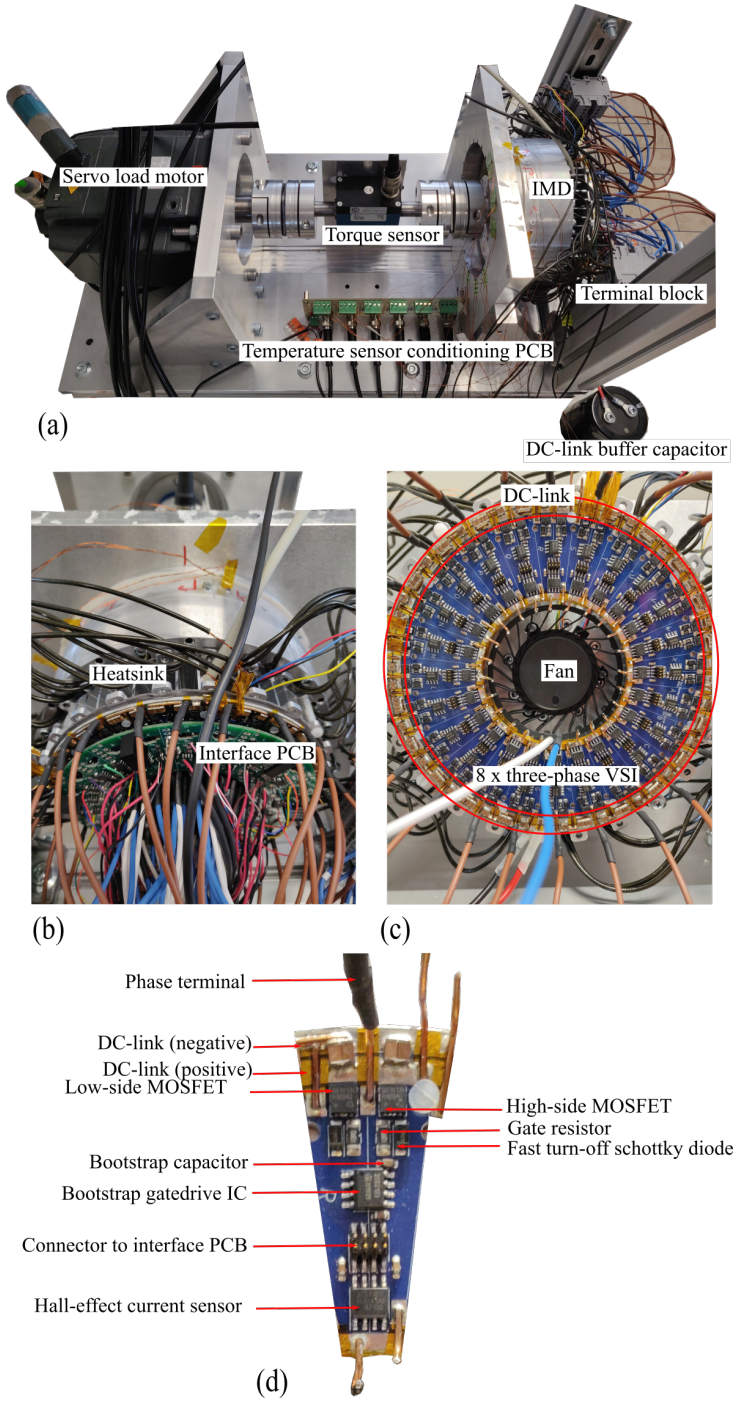

Figure 2.3: Hardware realization of IMD concept: (a) IMD mounted on testbench (b) Close-up of IMD prototype (c) IMD without the interface PCB, showing the 24 phase inverter and fan (d) Close-up of a single half-bridge inverter module

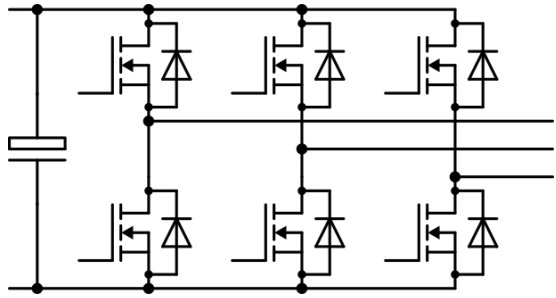

Figure 2.4: The IMD concept uses 8 three-phase VSIs connected in parallel to a common DC-link.

mon DC-link (Fig. 2.4). Each three-phase VSI consists of the same identical half-bridge modules as shown in Fig. 2.3d based on 100 V Silicon MOSFETs. The switching frequency was fixed at 37.5 kHz. The complete VSI is mounted on a single layer Insulated Metal Substrate (IMS) PCB. With this inverter topology, every single slot of the YASA AFPMSM is supplied individually by a single half-bridge module. The slots are divided in 8 groups of three phases. Each group has its own star point which is isolated from the other star points. There are several reasons for this advanced modularization of the power electronics:

1. The chosen integration topology (Fig. 2.1) imposes specific geometric constraints on the space envelope occupied by the power electronics. Modularization into smaller submodules allows to achieve a higher fill factor of the allocated power electronics mountings space and thus results in higher volumetric torque density.

2. Through modularization, less slots have to be connected in series which results in a higher fundamental winding factor and thus torque density.

3. Modularization creates a redundancy in the power electronics which opens opportunities for fault-tolerant operation of the actuator. This was identified as an important aspect in exoskeleton applications [8].

Next to the drivers for modularization, there are also factors that plea in favour of less modularization: the number of auxiliary components such as current sensors, isolated power supplies and connectors scales with the number of modules. Additionally, the I/O capabilities of the processor scales with the number of modules resulting in a more expensive processor. The relative cost of these components in comparison to the total cost of a module will play an important role when selecting the number of modules.

Another point of interest in the design of an IMD is the DC-link architecture. The DC-link often takes up a large portion of the volume of an in-

verter [9]. Additionally, the aspect-ratio and/or shape of many commercially available capacitors might not fit geometric constraints of a certain integration topology. Researchers have studied strategies to reduce the DC-link capacitor requirements in [10] or optimized the busbar topology [11]. In [12, 13] a custom capacitor design is proposed to meet the geometric constraints of the integration concept. In this work, the DC-link consists of 144 Surface Mount Device (SMD) multilayer ceramic capacitors of 2.2 μF located close to the swithces on the outer annulus of the inverter PCB to absorb the high frequency current ripple. A 2.2 mF electrolytic capacitor is added to serve as an energy buffer because the DC power supply is connected via 4 meter cable to the inverter.

The proliferation of SMD packages enabled a further miniaturization of electronics, a reduction of parasitic inductance and thus the opportunity to reduce switching losses. The compactness of SMD packages made new integration concepts possible. However, it also made heat dissipation in power electronic switches more complicated in comparison to through-hole TO-type packages. To overcome this issue [4, 14] used thermal vias to improve heat dissipation through the PCB, [15] used an SMD package that allowed two-sided cooling and thick copper layers to spread the heat over a larger surface area. In this work, an IMS PCB is used. Since it only has a 100 μm enamel insulation layer, it also has excellent thermal properties.

Finally, a separate interface PCB (see Fig. 2.3) is used that comprises digital isolators and auxiliary power supplies to provide a galvanic isolation between the processing unit and the inverter. The processing unit was not included in the IMD instead a dSPACE MicroLabBox® was used to allow rapid control prototyping and I/O configuration. Since every single tooth coil has its own half-bridge module, this offers additional degrees of freedom that can be exploited for e.g. fault-tolerant control or harmonic current injection [10]. In this work, each three-phase VSI uses conventional Field Oriented Control (FOC) of the stator currents [16] with a control frequency of 12.5 kHz.

2.1.2 Fan-Heatsink Combination

The opportunity to use a shared cooling for the motor and power electronics is a major motivation for integration as it increases the torque density [3, 4, 17, 18]. Therefore this section focuses on the thermo-mechanical integration aspects of the IMD concept. Forced air cooling by means of a single centrifugal frameless fan which can rotate independently from the motor shaft, is used to dissipate both motor and converter losses. Although the convection coefficient of forced air cooling can be an order of magnitude lower in comparison to water cooling, this does not necessarily leads to a lower system torque density as explained already in Section 1.3. Additionally, the hoses required

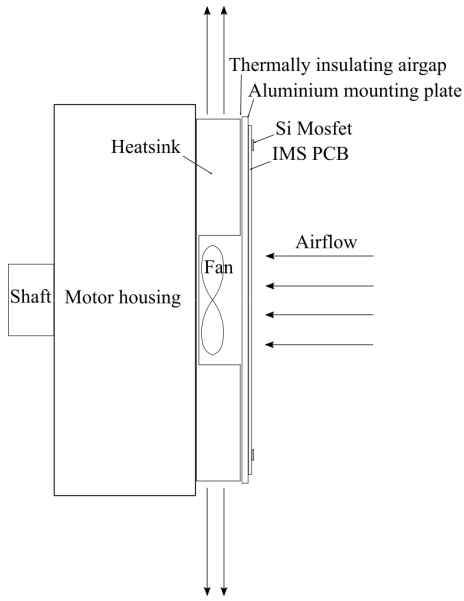

Figure 2.5: Illustration of the fan-heatsink concept evaluated in this work

to distribute the coolant over the robots joints raises concerns about reliability. Forced air cooling was eventually selected to eliminate the complexity associated to the implementation of a liquid cooling system in a mobile robot systems with multiple moving parts [19].

Fig. 2.5 visualizes schematically the airflow directions and the heatsink configuration of the considered fan-heatsink combination. Its main geometric specifications are given in Table 2.1. Analytical formulas for the heat transfer and pressure drop in rectangular channels [20] were used in combination with the pressure rise - airflow characteristic of the fan to derive the thermal resistance of the heatsink as a function of the number of fins and fin thickness. This led to the conclusion that the maximum number of fins and the minimum fin thickness should be chosen that satisfy the manufacturing constraints. Since the prototype heatsink is manufactured through CNC milling, a minimum fin spacing and fin thickness have to be respected.

The power electronics converter is mounted on an aluminum plate which acts as a heatsink. The mounting plate does not contain fins. An airgap between the mounting plate and motor heatsink acts as a thermal barrier. This allows both heatsinks to have a different temperature, and thus helps to respect the strongly different temperature limits of the motor and power electronics converter. In [21, 22], thermal insulation sheets were used to create this thermal barrier in forced air-cooled IMDs, however these sheets covered a substan-

Table 2.1: Specifications of the fan-heatsink combination

Motor heatsink	**Value**	**Unit**
Fin inner diameter	68	mm
Fin outer diameter	142	mm
Fin thickness	1.2	mm
Fin spacing (@ inner diameter)	3.25	mm
Fin height	16	mm
Number of fins	48	/
Material	aluminum	/
Weight	222	g
Fan		
Outer diameter	60	mm
Rotational speed	3300	rpm
Max air flow (at zero pressure rise)	0.274	m^3/min
Max pressure rise (at zero air flow)	158	Pa
Weight	28	g
Converter mounting plate		
Outer diameter	143	mm
Inner diameter	64	mm
Material	aluminum	/
Weight	110	g

tial part of the motor's outer surface hence underutilizing the motor's cooling potential.

2.2 IMD Torque Density

This section presents the torque density evaluation of the axial endplate mount IMD concept presented in this chapter. The evaluation of the torque density requires to find the thermal limit of the IMD, hence there is the risk of irreversible damage if this thermal limit is exceeded even temporarily. To overcome this, experimental data will be used to validate a 3D thermal Finite Element (FE) model. This model allows to predict the torque density without the risk of damaging the IMD prototype. Eventually, the predicted torque density will be compared to other IMDs for novel service robot applications.

2.2.1 Thermal Modelling

This section will discuss the thermal modelling of the considered IMD concept. A 3D thermal FE model will be used to find the spatial temperature

distribution for a given loss distribution. The discussion here will focus on the motor heatsink and power electronics converter. For a detailed discussion on the thermal modelling of the motor, the reader is referred to Chapter 4. However it is worth stressing that both the motor, heatsink and power electronics are included in the same FE model. Fig. 2.6 depicts the geometry used in the FE model. Due to symmetry, it is sufficient to model only one half of a stator tooth. A boundary condition expressing thermal symmetry is imposed on the symmetry planes. The rotor, bearings, fan and mounting frame are not explicitly included in the model.

The heat dissipation due to the airflow in the airgap caused by the rotation of the rotor is included in the model by imposing a convective heat flux on the airgap surfaces with h_{airgap} the convective heat transfer coefficient [23]. The heat dissipation due to the airflow of the fan is also included by imposing a convective heat flux on the surface of the motor heatsink and PCB mounting plate. Note that a different convection coefficient has to be used for the motor side heatsink surface ($h_{\text{fan,motor}}$) and for the power electronics converter side heatsink surface ($h_{\text{fan,conv}}$) to account for the reduced heat transfer on the converter side. The average airflow velocity on the converter side is lower since the fan is located closer to the motor and the majority of the air leaves the lower portion of the fan blades resulting in a higher average convection coefficient on the motor side [24]. The heat dissipation via the bearings is neglected and a boundary condition representing thermal insulation is imposed on the inner radius of the stator. The mounting frame is not modelled explicitly, it is represented by a thermal network consisting of a thermal resistance in parallel with a thermal capacitance. This thermal network imposes the boundary condition on the axial surface of (6) in Fig. 2.6 opposite to the housing shell (8). On the external surface of the motor housing i.e. (6) and (8) in Fig. 2.6 air flows under the action of natural convection, this is also the case for the external surface of the PCB i.e. (14) in Fig. 2.6. A boundary condition expressing convective heat transfer with $h_{\text{housing,motor}}$ the convective heat transfer coefficient is used for the motor housing. For the PCB, h_{PCB} is used as convective heat transfer coefficient. Only the losses of the semiconductor power switches are included in the model, the losses of auxiliary components are neglected. The power electronics losses are represented by imposing a heat flux on the PCB surface that corresponds to the footprint of the semiconductor power switches. The junction temperature is then found by using the average temperature of this surface and the thermal resistance of junction-to-drain from the mosfet's datasheet [25]. The single layer IMS PCB is represented by aluminum core of 1.6 mm and a 100 μm enamel layer.

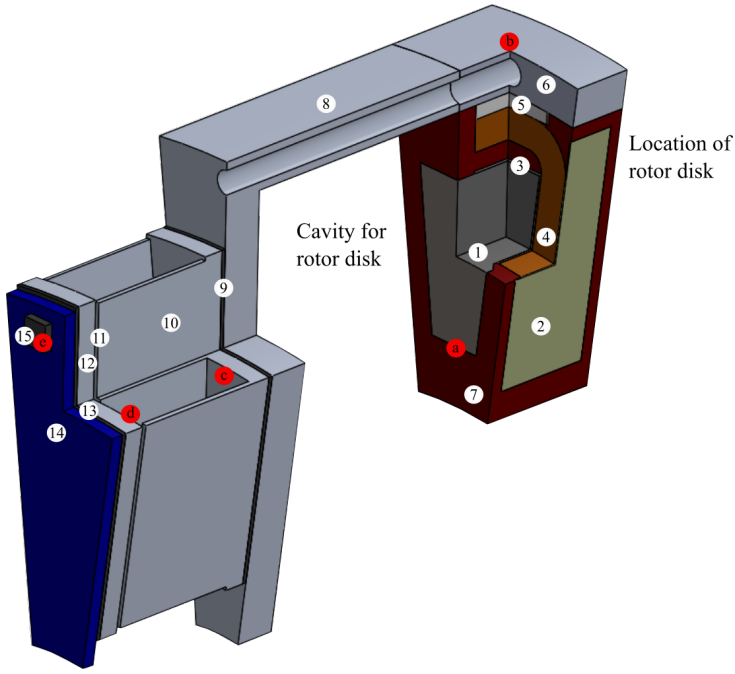

Figure 2.6: Cut-out view of the geometry used in the FE model: (1) Laminated iron core (2) Mica intra slot insulation (3) Mica -Kapton laminate slot liner (4) Round enamelled copper wire winding body (5) aluminum-oxide thermal pad and phase-to-ground insulation (6) Stator housing (7) Epoxy potting (8) Housing shell (9) Ceramic filled silicone thermal sheet (10) Motor heatsink (11) Airgap (12) Power electronics mounting plate (13) Ceramic filled silicone thermal sheet (14) IMS PCB (15) Mosfet (PQFN package); PT100 temperature sensors: (a-b-c-d-e).
For clarity the rotor disks are not shown on the figure, however their intended location is indicated on the figure.

2.2.2 Model Validation

This section describes the validation of the thermal FE model introduced in Section 2.2.1. The validated model will be required for the torque density evaluation in Section 2.2.3. A thermal transient test is performed on the testbench shown in Fig. 2.3a. Fig. 2.6 indicates the location of the PT100 temperature sensors. To account for small spatial variations in the motor thermal properties, the average of three temperature sensors over the circumference of the motor is used. The temperatures are sampled at 1.25 kHz. The temperature data is post-processed by applying a moving average with a window of 10 ksamples and further downsampling to 0.25 Hz. To validate the thermal FE

model, the measured temperature response will be compared to the simulated response. A load motor keeps the speed constant at 100 rpm and a step in the current setpoint is applied which corresponds to a step in the torque from 0 to 4 Nm. Initially the motor is in thermal steady-state and all temperatures are recorded during the transient test until the time derivative of all temperatures drops below 0.5°C/10 min. This takes approximately 100 minutes. During this transient test also the electrical input power and the mechanical output power are measured. In order to determine the electrical input power, the DC current and voltage are measured with an accuracy of 3% and 1.5% on the reading respectively. To determine the mechanical output power, the rotational speed and torque are measured. The torque is measured using a Lorenz Messtechnik DR-2112 strain-gauge based rotational torque sensor with an accuracy of 0.1 Nm. The measured temperature response is given in Fig. 2.7a.

The simulated temperature response is given in Fig. 2.7b. The thermal FE model parameters that give rise to this temperature response are given below. The material properties of the motor's subcomponents can be found in Table 5.4 in Chapter 5. The material properties of the heatsink and power electronics converter subcomponents which are not already mentioned in Table 5.4 in Chapter 5 are given in Table 2.2. The values for the convection coefficients are given in Table 2.3. Note that these are the values that result in a good fit between estimated temperatures and measured temperatures in one specific operating point, hence these coefficients are also only valid in that operating point. The airgap convection coefficient according to the empirical formulas of [26] falls between 35 and 70 W/m^{2}K. Taking into account the fact that the empirical formulas were not calibrated for the low operating speed considered here, these values agree reasonably well with the value found in Table 2.3. The parameters for the boundary conditions representing a thermal network are given in Table 2.4.

The losses in the winding body (4), the laminated iron core (1) and the semiconductor power switch (15), are derived from the difference between the measured electrical input power P_{el} and mechanical output power P_{m}, the total dissipated power is given by:

$$P_{\text{loss}} = P_{\text{el}} - P_{\text{m}} = 66W \tag{2.1}$$

The losses in the winding P_{w} (4) are then found using the resistance of a tooth coil $R_0 = 94.5m\Omega$ at 25°C, the resistance temperature coefficient of copper $\alpha_{\text{Cu}} = 0.00393/K$, the average temperature difference with the reference temperature $\Delta T^{25°C} = T_{\text{av,Cu}} - 25°C = 30°C$ with $T_{\text{av,Cu}} = 55°C$ the average temperature of the copper winding, the RMS phase current $I_{\text{ph}} = 4.6A_{\text{RMS}}$

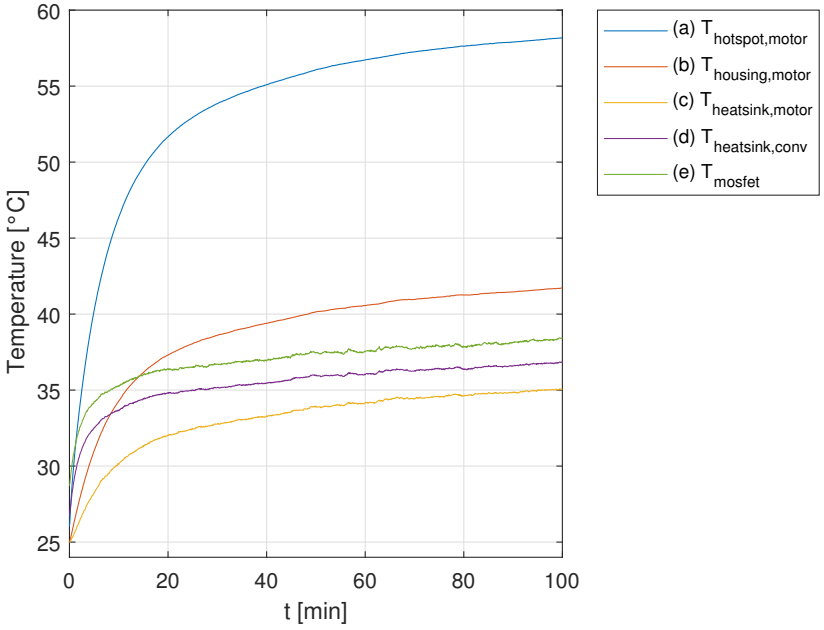

(a) Measured temperature response

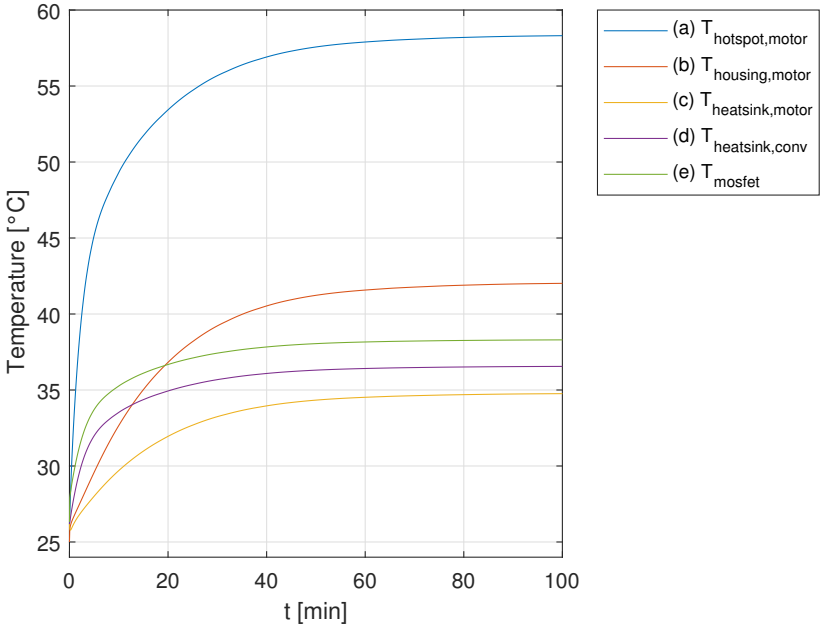

(b) Simulated temperature response

Figure 2.7: Measured (a) and simulated (b) temperature response at different location (see Fig. 2.6) in the IMD prototype shown in Fig. 2.3b for a step in the torque from 0 to 4 Nm at 100 rpm.

Table 2.2: Heatsink and power electronics converter material properties

Thermal conductivity	**Symbol**	**W/mK**
Air	k_{air}	0.026
IMS PCB enamel	$k_{\text{enamel,PCB}}$	1
Thermal sheet	k_{sheet}	2
Specific heat capacity	**Symbol**	**kJ/kgK**
Air	$C_{\text{p,air}}$	1
IMS PCB enamel	$C_{\text{p,enamel,PCB}}$	0.798
Thermal sheet	$C_{\text{p,sheet}}$	0.798
Density	**Symbol**	**kg/m^3**
Air	ρ_{air}	1.29
IMS PCB enamel	$\rho_{\text{enamel,PCB}}$	1540
Thermal sheet	ρ_{sheet}	1540

Table 2.3: Convection coefficients

Surface	**Symbol**	**W/m^{2}K**
airgap	h_{airgap}	30
motor side heatsink	$h_{\text{fan,motor}}$	90
converter side heatsink	$h_{\text{fan,conv}}$	40
motor housing	$h_{\text{housing,motor}}$	15
PCB surface	h_{PCB}	2

Table 2.4: Thermal network boundary conditions

Mounting frame	**Symbol**	**Value**	**Unit**
Thermal resistance	R_{frame}	5.37	K/W
Thermal capacitance	C_{frame}	3.38	kJ/K
Mosfet	**Symbol**	**Value**	**Unit**
Thermal resistance junction-to-drain	R_{jd}	1.1	K/W

and the number of tooth coils i.e. 24:

$$P_{\text{w}} = 24 \cdot R_0 \cdot (1 + \alpha_{\text{Cu}} \cdot \Delta T^{25^\circ C}) \cdot I_{\text{ph}}^2 = 24 \cdot 2.23W = 53.6W \qquad (2.2)$$

The losses in the laminated iron core P_{core} were estimated from a no-load test at 100 rpm. A total no-load loss of 1.06W was measured. This value includes rotor losses, stator losses in both the core and winding, bearing friction losses and windage losses. It is assumed that P_{core} constitutes one half of the no-load losses. Finally, the losses in the semiconductor power switch are estimated

from:

$$P_{\text{mosfet}} = \frac{P_{\text{loss}} - P_{\text{core}} - P_{\text{w}} - P_{\text{term}}}{2 \cdot 24} = 0.136W \tag{2.3}$$

With P_{term} the losses in the terminal wires i.e. the wires connecting the coils to the power converter:

$$P_{\text{term}} = 24 \cdot R_{\text{term}} \cdot I_{\text{ph}}^2 = 8.29W \tag{2.4}$$

With $R_{\text{term}} = 16.3m\Omega$.

It can be concluded that the simulated and measured temperature responses agree well i.e. less than $0.5°C$ difference, validating the calculated power losses and predictive performance of the thermal FE model.

2.2.3 Torque Density Evaluation

In this section, the gravimetric and volumetric torque density i.e. the torque per unit of mass and per unit of volume respectively are determined using the thermal FE model outlined in Section 2.2.1. To determine the torque density, the maximum continuous torque the IMD can generate in thermal steady-state is required. This is the torque for which either the winding temperature reaches its temperature limit or the semiconductor switch reaches its temperature limit. Although insulation of the used copper wire and the epoxy potting have a temperature rating of 180°C, to guarantee long term reliability of the insulation and sufficient mechanical stability of the epoxy, the temperature limit was set to 150°C. For the semiconductor switch, the temperature limit was set to 100° to insure long term reliable operation. The torque for which one of these temperature limits is reached, is determined iteratively by increasing the current and thus the losses gradually. The winding losses and power electronics losses were scaled with the square of the current. The simulated temperatures for a steady-state torque of 7.88 Nm are given in Table 2.5. It can be concluded that for this torque, the winding temperature $T_{\text{hotspot,motor}}$ reaches its limit first. The IMD mass and volume and eventually the gravimetric and volumetric torque density are given in Table 2.6. In the remainder of this work gravimetric torque density will be used to denote torque per unit of mass and volumetric torque density to denote torque per unit of volume, if gravimetric or volumetric is not specified explicitly, the author refers to both.

2.2.4 Discussion

Since the winding temperature limit is reached first, the motor and not the power electronics converter constitutes the limiting factor for the IMD torque density. Therefore in Chapter 4 and 5 strategies to improve the torque density

Table 2.5: Steady-state temperature (see Fig. 2.6) for a motor producing 7.88 Nm torque at 100 rpm

Temperature	**°C**
(a) $T_{\text{hotspot,motor}}$	150
(b) $T_{\text{housing,motor}}$	87.2
(c) $T_{\text{heatsink,motor}}$	59.2
(d) $T_{\text{heatsink,conv}}$	66.3
(e) T_{mosfet}	73.0

Table 2.6: Torque density of the IMD prototype realised in this dissertation

	this work	[1]	[27]	[28]	**unit**
IMD mass	4	/	0.23	0.81	kg
IMD volume	1.8	/	/	/	liter
Torque density					
gravimetric	2[1]	8.3	2	3.7	Nm/kg
volumetric	4.35[1]	/	/	/	Nm/liter

[1]+12% if the convection coefficient of the finned heatsink was 600W/m^{2}K which would be possible with water cooling

of the motor will be discussed. These strategies focus on the improving the thermal performance of the motor i.e. reducing its thermal resistance.

Note that the temperature difference between the winding and the semiconductor switch is larger than the typical uncertainty on the measurements, hence a detailed uncertainty analysis is not necessary.

Fig. 2.8 shows the mass distribution of the IMD prototype. The rotor discs account for 43% of the IMD mass. Strategies to further increase the torque density should therefore first focus on reducing the rotor mass since this also improves the torque over inertia ratio which is also important in applications with dynamic motion profiles like legged robots. However, this falls beyond the scope of this work and will be extensively studied in the recently granted European project CliMAFlux. For completeness, Fig. 2.9 also gives the volume distribution.

It is instructive to compare the torque density of the IMD realization in this work to other IMD's and motor's. In Fig. 2.10, the volumetric torque density is plotted versus the rated torque for some commercially available servo drives, torque motors, a state-of-the-art IMD from [29] and the IMD developed in this work. This figure clearly shows a linear relation between the volumetric torque density and rated torque. It also allows to assess the performance of

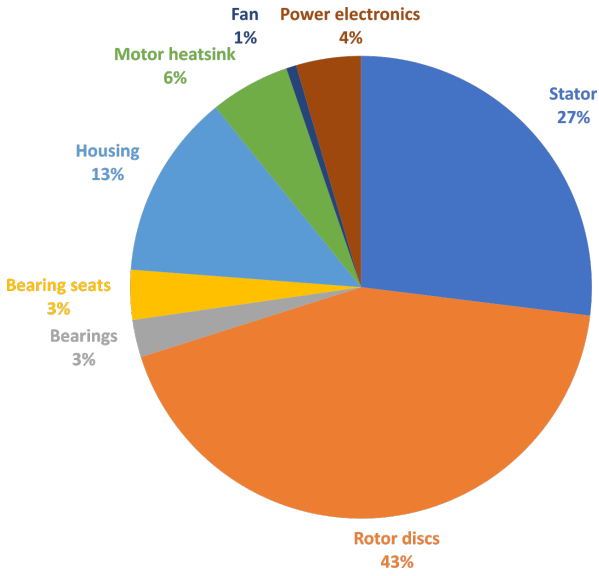

Figure 2.8: Pie chart illustrating the mass distribution of the IMD prototype. The total mass of the IMD is 4 kg. The IMD exhibits a gravimetric torque density of 2 Nm/kg

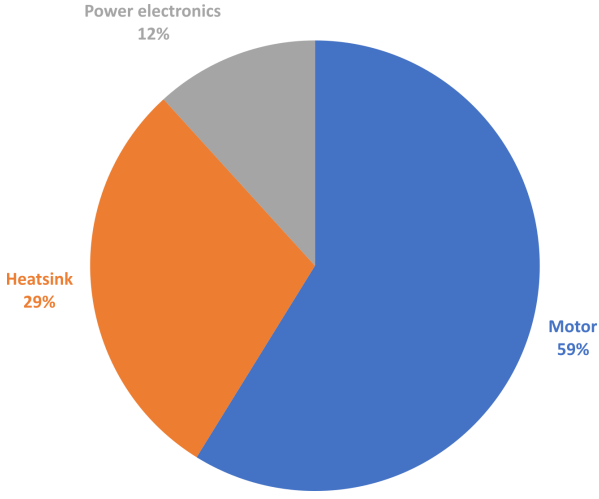

Figure 2.9: Pie chart illustrating the volume distribution of the IMD prototype. The total volume of the IMD is 1.8 liter. The IMD exhibits a volumetric torque density of 4.35 Nm/liter

the IMD of this work with respect to existing motors and IMDs for servo or robotic applications. However since novel service robot applications feature very specific requirements it might be more instructive to have a deeper look into the torque density performance of other state-of-the-art motors and IMDs designed for this application and compare them to the IMD of this dissertation. The authors in [1] reported a torque density of 8.3 Nm/kg and argued that a torque density of 10 Nm/kg would be sufficient to realize a direct-drive articulated robot arm. In contrast to this work, they used a water-cooled, single rotor double stator topology axial flux motor with an outer diameter of 260 mm. They did not include the mass of the power converter and auxiliary components of the water cooling system in their torque density calculation, also the torque of axial flux motors scales with the third power of the diameter [8]. This makes it difficult to compare their result with the IMD of this work. [27] also reports a thorough characterization of an axial end plate mount IMD concept for a wearable robotics application. The power electronics converter is mounted directly against the motor's axial endplate without a heatsink in between. Both motor and power electronics only rely on passive air cooling. They reported an almost identical value for the torque density in comparison to this work. It should be noted that the electric motor, power electronics and heatsink configuration of the IMD in this work have not been subject to an optimization process, they are the result of a first design iteration. Additionally, it was already explained at the start of this paragraph that there are still opportunities to improve its torque density. A team of researchers at MIT has designed a dedicated electric motor for a legged quadruped robot application [28]. They report a continuous torque density of 3.7 Nm/kg. This is the result of an optimised electromagnetic design and the use of a cobalt-iron alloy with a high saturation flux density. However, this value does not take the power electronics and housing mass into account and no details on the used cooling method were provided making it difficult to compare this motor.

2.3 Conclusion

In this chapter, an axial endplate mount integration concept for the electric motor and power electronics was introduced. Integrating the motor and its power electronics converter creates the opportunity to share parts of the thermal management system, i.e. a fan-heatsink combination in this case. Additionally, separate enclosures and wire harness connecting both are avoided. The torque density of this concept was evaluated using a 3D thermal Finite Element model validated by experimental data obtained on a testbench. As mentioned in Table 2.6, a torque density of 2 Nm/kg was achieved. When comparing this result to the state-of-the-art, it was concluded that there was

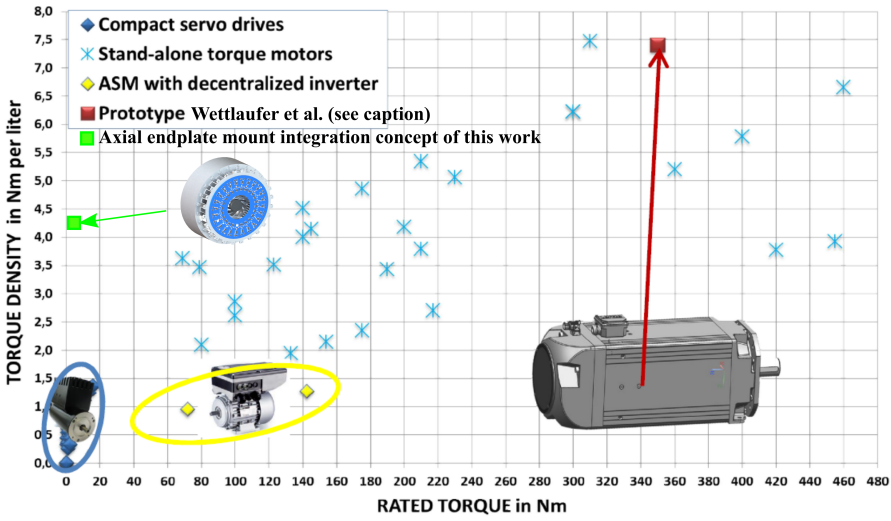

Figure 2.10: Volumetric torque density versus rated torque for various commercially available servo drives, torque motors, an IMD prototype from [29] and the IMD in this work (figure adapted from [29])

still room for improvement. The type of conductor and the rotor mass were identified as key bottlenecks for the torque density.

References

[1] F. Aghili, J. M. Hollerbach, and M. Buehler, "A modular and high-precision motion control system with an integrated motor," *IEEE/ASME Transactions on Mechatronics*, vol. 12, no. 3, pp. 317–329, 2007.

[2] S. Chowdhury, E. Gurpinar, G.-J. Su, T. Raminosoa, T. A. Burress, and B. Ozpineci, "Enabling technologies for compact integrated electric drives for automotive traction applications," in *2019 IEEE Transportation Electrification Conference and Expo (ITEC)*, 2019, pp. 1–8.

[3] T. M. Jahns and H. Dai, "The past, present, and future of power electronics integration technology in motor drives," *CPSS Transactions on Power Electronics and Applications*, vol. 2, no. 3, pp. 197–216, 2017.

[4] A. H. Mohamed, H. Vansompel, and P. Sergeant, "An integrated modular motor drive with shared cooling for axial flux motor drives," *IEEE Transactions on Industrial Electronics*, vol. 68, no. 11, pp. 10 467–10 476, 2021.

[5] J. Van Damme, L. Verkroost, H. Vansompel, F. De Belie, and P. Sergeant, "A holistic dc link architecture design method for multiphase integrated modular motor drives," in *2019 IEEE International Electric Machines and Drives Conference (IEMDC)*, 2019, pp. 1593–1598.

[6] D. Schwarzer, F. Avcilar, A. Giedymin, C. Dinca, and U. Schäfer, "Foldable motor integrated low voltage inverter for an electrical power steering application," in *2018 20th European Conference on Power Electronics and Applications (EPE'18 ECCE Europe)*, 2018, pp. P.1–P.9.

[7] P. Brockerhoff, W. Schön, P. Blaha, P. Vaclavek, and Y. Burkhardt, "Disc inverter in highly integrated 9-phase drivetrain for e-mobility," in *2015 17th European Conference on Power Electronics and Applications (EPE'15 ECCE-Europe)*, 2015, pp. 1–9.

[8] M. Waldhof, A. Echle, and N. Parspour, "A novel drive train concept for personalized upper body exoskeletons with a multiphase axial flux machine," in *2019 IEEE International Electric Machines and Drives Conference (IEMDC)*, 2019, pp. 2160–2166.

[9] M. Marz, A. Schletz, B. Eckardt, S. Egelkraut, and H. Rauh, "Power electronics system integration for electric and hybrid vehicles," in *2010 6th International Conference on Integrated Power Electronics Systems*, 2010, pp. 1–10.

[10] L. Verkroost, J. Van Damme, D. V. Bozalakov, F. De Belie, P. Sergeant, and H. Vansompel, "Simultaneous dc-link and stator current ripple reduction with interleaved carriers in multiphase controlled integrated modular motor drives," *IEEE Transactions on Industrial Electronics*, vol. 68, no. 7, pp. 5616–5625, 2021.

[11] A. H. Mohamed, H. Vansompel, and P. Sergeant, "Design of an integrated dc-link structure for reconfigurable integrated modular motor drives," *IEEE Transactions on Industrial Electronics*, vol. 69, no. 3, pp. 2312–2321, 2022.

[12] Ring shaped capacitor design - tdk corporation. Available at https://www.electronicdesign.com/technologies/passive-components/article/21198098/power-capacitors-ringshaped-design-for-emobility (accessed: 26-05-2023).

[13] R. U. A. Shaikh, A. Saeed, and R. Kumar, "Review on present and future integration techniques for capacitors in motor drives," in *2018 International Conference on Computing, Mathematics and Engineering Technologies (iCoMET)*, 2018, pp. 1–8.

[14] Benjamin katz - mit - blogpost. Available at https://build-its-inprogress.blogspot.com/2018/ (accessed: 16-05-2023).

[15] F. Sugai, K. Kojima, Y. Kakiuchi, K. Okada, and M. Inaba, "Design of tiny high-power motor driver without liquid cooling for humanoid jaxon," in *2018 IEEE-RAS 18th International Conference on Humanoid Robots (Humanoids)*, 2018, pp. 1059–1066.

[16] J. A. Melkebeek, *Electrical Machines and Drives*. Springer International Publishing, 2018.

[17] R. Abebe, G. Vakil, G. Lo Calzo, T. Cox, S. Lambert, M. Johnson, C. Gerada, and B. Mecrow, "Integrated motor drives: state of the art and future trends," *IET Electric Power Applications*, vol. 10, no. 8, pp. 757–771, 2016.

[18] R. Wrobel, "A technology overview of thermal management of integrated motor drives- electrical machines," *Thermal Science and Engineering Progress*, vol. 29, p. 101222, 2022.

[19] A. J. Jeffrey, P. H. Connor, G. Vakil, P. Evans, P. Wheeler, and S. Hart, "Cooling system sizing using lptn analysis and multiphysics modelling for an axial flux machine and integrated drive," in *2022 International Conference on Electrical Machines (ICEM)*, 2022, pp. 1376–1382.

[20] H. D. Baehr and K. Stephan, *Wärme- und Stoffübertragung*. Springer Berlin Heidelberg, 2019.

[21] S. Pickering, P. Wheeler, F. Thovex, and K. Bradley, "Thermal design of an integrated motor drive," in *IECON 2006 - 32nd Annual Conference on IEEE Industrial Electronics*, 2006, pp. 4794–4799.

[22] T. Bringezu and J. Biela, "Cooling limits of passively cooled integrated motor drives," in *2021 23rd European Conference on Power Electronics and Applications (EPE'21 ECCE Europe)*, 2021, pp. P.1–P.11.

[23] D. Howey, "Thermal design of air-cooled axial flux permanent magnet machines," Doctoral Thesis, Imperial College London, Zurich, 2010.

[24] J. Stafford, E. Walsh, and V. Egan, "A study on the flow field and local heat transfer performance due to geometric scaling of centrifugal fans," *International Journal of Heat and Fluid Flow*, vol. 32, no. 6, pp. 1160–1172, 2011.

[25] Datasheet infineon si mosfet bsz097n10ns5atma1. Available at https://www.infineon.com/cms/en/product/power/mosfet/n-channel/bsz097n10ns5/ (accessed: 5-06-2023).

[26] Rasekh, Alireza, "Computational study of convective cooling and windage losses of axial flux permanent magnet synchronous machines," Ph.D. dissertation, Ghent University, 2017.

[27] U. H. Lee, C.-W. Pan, and E. J. Rouse, "Empirical characterization of a high-performance exterior-rotor type brushless dc motor and drive," in *2019 IEEE/RSJ International Conference on Intelligent Robots and Systems (IROS)*, 2019, pp. 8018–8025.

[28] M. G. Angle, J. H. Lang, J. L. Kirtley, S. Kim, and D. Otten, "Optimization of surface-mount permanent magnet synchronous machines for low duty-cycle, high-torque applications," in *2017 IEEE International Electric Machines and Drives Conference (IEMDC)*, 2017, pp. 1–6.

[29] J. Wettlaufer, H. Borcherding, F. Klute, and T. Jonsky, "A compact servo drive: Five phase, air cooled, with highly integrated inverter for industrial use," in *2015 17th European Conference on Power Electronics and Applications (EPE'15 ECCE-Europe)*. IEEE, 9 2015, pp. 1–10.

Chapter 3

Anodized Aluminum Foil Winding Axial Flux Machine for Quasi-Direct-Drive Robotic Applications: Preliminary Design and Manufacturing

This chapter aims to address the mechanical challenges related to the use of anodized aluminum foil as already mentioned in Section 1.4.

This is -to the author's best knowledge- the first description in the publicly available scientific literature of a functional rotating electrical machine with anodized aluminum foil. The brittle nature of the aluminum-oxide layer and the fragile nature of the thin foil make manual processing of the foil extremely difficult. This possibly explains why no rotating machine using this foil has been reported yet. Additionally, bending the foil creates hairline cracks in the anodization layer which result in a decreased breakdown voltage. In this chapter, the use of a Yokeless and Segmented Armature Axial Flux Permanent Magnet Synchronous Machine (YASA AFPMSM) topology is proposed to cope with the particular mechanical properties of the foil. The inherent segmented nature of the YASA AFPMSM make it possible to rely on conventional foil winding methods used in inductor and transformer manufacturing. This chapter describes the preliminary design of the YASA AFPMSM studied extensively in Chapter 4 for a quasi-direct-drive robotic application. The focus of this dissertation is not on optimizing the electromagnetic design but rather to evaluate the use of anodized aluminum foil in a YASA AFPMSM.

Another mechanical challenge studied in this chapter is related to creating an electrical connection between another conductor and anodized aluminum

foil. The high melting temperature and hardness of the oxide layer impede the use of conventional soldering methods as used for connecting copper wires. In this chapter two methods have been tested: ultrasonic welding of a copper wire onto the anodized aluminum foil and soldering onto a nickel-plated pad of the anodized aluminum foil.

Anodized Aluminum Foil Winding Axial Flux Machine for Quasi-Direct-Drive Robotic Applications: Preliminary Design and Manufacturing

Adapted from: J. Van Damme, H. Vansompel, G. Crevecoeur, K. Faes, R. Nunes and R. Tack, "Anodized Aluminium Foil Winding Axial Flux Machine for (Quasi-)Direct-Drive Robotic Applications: Preliminary Design and Manufacturing," *2022 12th International Electric Drives Production Conference (EDPC)*, Regensburg, Germany, 2022, pp. 1-9, doi: 10.1109/EDPC56367.2022.10019769.

Abstract: Motivated by the need for higher torque density actuators in novel (quasi-)direct-drive robotics applications, a Yokeless and Segmented Armature Axial Flux Permanent Magnet Synchronous machine with anodized aluminum foil conductors instead of enamelled copper wire is considered in this work. Based on a requirements analysis of (quasi-)direct-drive actuators, a prototype axial flux machine is designed. Several design aspects are discussed keeping the application requirements in mind. It could be concluded that the combination of the machine topology and conductor material results in a high fill factor and excellent thermal properties, making it particularly promising for high torque density, low speed applications. A prototype was manufactured to demonstrate the feasibility of the design. The interconnection of aluminum foil to copper wire appeared to be challenging, two interconnection methods were tested and compared qualitatively.

3.1 Introduction

In novel robotic applications such as cobots, legged mobile robots and exoskeletons, there is the tendency to go towards low gear ratio actuators. These are called (Quasi-)Direct-Drive ((Q)DD) actuators and have a gear ratio ranging from 1:1 to 10:1 [1]. (Q)DD actuators inherently have a higher backdrivability which enables safer, more dexterous and dynamic robots which are

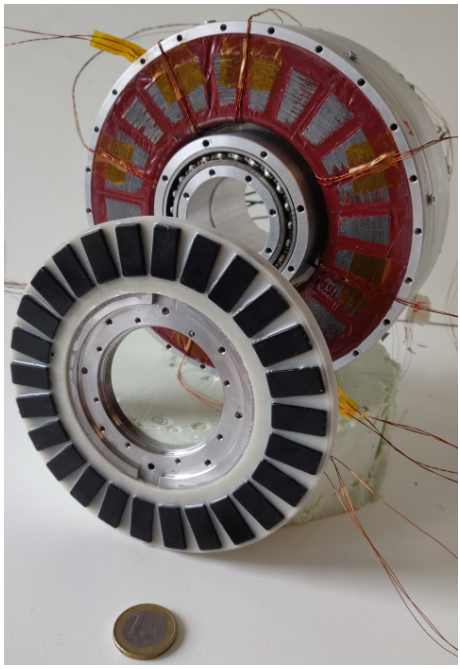

Figure 3.1: Assembled prototype YASA AFPMSM with anodized aluminum foil winding

capable of dealing with uncertain, unstructured and changing environments [2–5].

Despite the attractive features offered by (Q)DD actuators, they suffer from a low torque density caused by their low gear ratio, which limits the robot performance. For example, for an articulated robot to handle a useful payload and fulfil useful tasks, a system torque density of at least 10 Nm/kg is required [6, 7]. Several researchers have proposed techniques to increase the torque density of the electric motor in (Q)DD robotic actuators. In [8], the authors relied on Cobalt-Iron to achieve a high torque density since it has a higher saturation flux density compared to conventional electrical steel grades. In [6, 9, 10], stator winding encapsulation was proposed to improve the heat transfer in the stator and hence increase the torque density. A water-jacket cooling was used in [6, 9, 11] and evaporative cooling in [12] to improve the torque density. Despite the effectiveness of the mentioned techniques, the torque density is still limited by the low slot fill factor and thermal conductivity of the winding body often found in small electric motors for robotic applications. Either a distributed winding is used which typically has a fill factor between 35 - 45 % [13], or a concentrated fractional slot winding is used which has a higher fill factor, however it is still limited to 50 - 65 %[13] in large volume manufac-

turing processes that rely on needle or flyer winding of a full stator [14, 15]. Although potting and encapsulation techniques have been proposed to improve the equivalent thermal conductivity of the winding body, the insulation enamel and potting material are still an important bottleneck in the heat dissipation path [16].

In this work, a Yokeless and Segmented Armature (YASA) Axial Flux Permanent Magnet Synchronous Machine (AFPMSM) [17] with anodized aluminum foil is proposed to realize a high torque density electric motor through the combination of a high fill factor and superior thermal properties. The YASA AFPMSM topology, the foil winding topology and finally the limited thickness of the aluminum-oxide insulation layer of anodized aluminum conductors all contribute to a high fill factor. Note that the latter is not possible with copper foil. The foil winding topology and the aluminum-oxide electrical insulation layer of the anodized aluminum foil give rise to superior thermal properties.

First, in Section 3.2 the requirements of (Q)DD actuators for novel robotic applications are analysed. Subsequently, the design aspects of a YASA AFPMSM is described in Section 3.3 with special focus on how the properties of the considered motor topology and conductor material combination fulfils the requirements. Finally, the manufactured prototype is presented in Section 3.4 and several manufacturing challenges are described together with possible solutions. Special attention is paid to the electrical interconnection between the aluminum foil coil and its power electronic supply in Section 3.5. To this end, several interconnection methods were tested and compared qualitatively.

3.2 Requirements of (Quasi-)Direct-Drive Robotic Actuators

In this section the requirements for electric motors in (Q)DD actuators will be derived from the application needs in novel robotic applications such as cobots, legged mobile robots and exoskeletons.

A low gear ratio is often beneficial from an application point of view since it improves the backdrivability [10] and enables proprioceptive force sensing [18]. However, reducing the gear ratio requires an increasing motor torque to obtain the same actuator output torque. Additionally, a low actuator mass is required since this reduces the actuator output torque requirements in both static and dynamic situations [19]. Hence both high torque and torque density are important requirements in (Q)DD robotic applications.

The actuator output speed requirements in (Q)DD robotic applications are low, typically the maximum output speed remains below 350 rpm in highly dynamic legged mobile robots [3], even lower output speed requirements are

found in cobots or humanoid robots [20] and exoskeletons [21]. In these applications, the output speed does often not exceed 150 rpm. For direct-drive actuators, the mentioned output speeds equal the motor speed. For quasi-direct-drive applications, assuming a maximum gear ratio of 10:1 [1], the maximum required motor speed remains below 3500 rpm. Design aspects for both a direct- and quasi-direct-drive actuator will be discussed in Section 3.3.

A common requirement in cobots or humanoid robots, legged mobile robots and exoskeletons is the need to safely cooperate with humans in their environment. To this end, (Q)DD actuators were introduced, to ensure safe mechanical interaction between humans and robotic devices. However, ensuring electrical safety might be even more important. Therefore, the motor should be capable of operating from a three-phase inverter with a low DC bus voltage. A DC bus voltage level of 48 V is selected for the prototype design in this work, since it is considered the highest safe voltage in common use [22].

The authors in [4] have illustrated the benefits of large airgap radius motors for (Q)DD robotic applications. However, since motor mass is often constrained in dynamic robotic applications, this results in the requirement for pancake shaped motors.

Finally, the mentioned novel robotic applications are often characterised by highly dynamic motions, hence requiring large accelerations. Therefore the maximum motor acceleration which is determined by the ratio of maximum motor torque over motor inertia is also an important design goal [23].

3.3 Design Aspects

The main geometric dimensions and properties of the prototype YASA AFPMSM with anodized aluminum foil winding are listed in Table 3.1. This section provides motivations for the most important design parameters keeping in mind the application requirements. Note however, that these parameters are not necessarily optimal in terms of torque (density), and inertia. This would require a thorough optimization study involving finite element electromagnetic models. This is beyond the scope of this article since the aim is not to optimize, but to check the feasibility and qualitatively evaluate the performance of using a YASA AFPMSM with anodized aluminum foil winding in a (Q)DD actuator application.

The analytical electromagnetic model for the flux density distribution in the stator teeth from [24] was used to evaluate the back-emf and determine the number of turns. The resulting induced voltage is both compatible with three-phase and 24-phase operation by changing the number of coils in series. For three-phase operation, 8 coils are connected in series and a maximum speed of 300 rpm can be obtained which satisfies the requirements of a direct-drive

Table 3.1: Specifications of the prototype YASA AFPMSM

Parameter	Symbol	Value	Unit
DC bus voltage	V_{DC}	48	V
Number of pole pairs	N_{p}	13	/
Number of slots	Q_{s}	24	/
Number of phases	n_{ph}	3 or 24	/
Maximum speed	Ω_{max}	300 or 2400	rpm
Nominal torque	T_{nom}	5	Nm
Number of turns per tooth coil	n_{turns}	35	/
Nominal phase current	I_{nom}	4.4	A_{RMS}
Outer diameter stator iron core	D_{o}	138.5	mm
Inner diameter stator iron core	D_{i}	98.5	mm
Axial length stator iron core	h_{stat}	15	mm
Axial slot length	h_{slot}	10	mm
Slot width	b_{slot}	6	mm
Airgap height	h_{air}	1.5	mm
Magnet height	h_{mag}	5	mm
Rotor yoke height	h_{mag}	6	mm
Rotor inertia	J_{rotor}	$50{\cdot}10^{-4}$	kgm^2

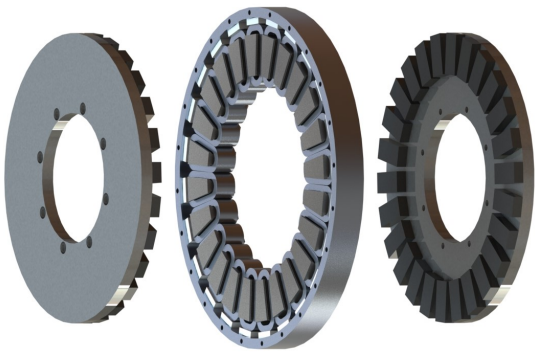

Figure 3.2: CAD drawing of the test case YASA AFPMSM

application, whereas for 24-phase operation, no coils are connected in series and the maximum speed is 2400 rpm, this is suitable for a QDD application. A CAD drawing and image of the prototype YASA AFPMSM are given in Fig. 3.2 and Fig. 3.1 respectively. The stator tooth coils were mechanically fixed by applying an epoxy potting technique.

3.3.1 Motor Topology and Main Dimension

A Yokeless and Segmented Armature Axial Flux machine topology was selected. Motivated by its modularity and fault tolerant capabilities, The YASA Axial Flux machine topology was already considered for an (Q)DD exoskeleton actuator application in [25]. This topology is known to have a high torque density since it is characterised by the absence of a stator yoke which reduces the iron losses and weight [17]. Based on the insights in [4]. The largest possible outer diameter that complies with the space constraints of the application is selected. The other geometric parameters were determined based on the guidelines in [25–27].

3.3.2 Number of Poles and Rotor Back-Iron Thickness

Since dynamic robot applications requires low inertia rotors, a high number of pole pairs is selected ($N_{\mathrm{p}} = 13$ for the prototype case). A rule of thumb states that the minimum thickness of the rotor iron yoke equals one fourth of the magnet width. Therefore increasing the number of poles for a constant rotor diameter, allows to reduce the rotor thickness and thus the inertia. However, a minimum rotor thickness is required to limit the deformation due to the attractive force between rotor and stator. The deformation also depends on the bearing arrangement. In the prototype YASA AFPMSM, the bearings are located at the inner diameter hence the inner diameter of the rotor disc is fixed, however the outer diameter can deform under the attractive forces. The deformation was calculated using analytical formulas from [28] and verified through mechanical finite element simulation (see Fig. 3.3). According to the following rule of thumb for the preliminary sizing of the rotor back-iron:

$$t_{\text{back-iron}} = \frac{B_{\text{rem}}}{B_{\text{sat}}} \frac{w_{\text{magnet}}}{2} \tag{3.1}$$

where $t_{\text{back-iron}}$ is the thickness of the back-iron, B_{rem} is the remanent magnetic flux of the magnets, B_{sat} is the saturation flux density of the back-iron steel and w_{magnet} is the width of a magnet, the thickness of the back-iron is 3.5 mm. However, to limit the deformation of the rotor discs to 3% of the airgap height, a thickness of 6 mm is selected, resulting in a heavy rotor with large inertia. Note that the use of an inner and outer diameter bearing would result in a thinner rotor back-iron. In the single rotor, dual stator AFPMSM topology, the rotor back-iron is even completely eliminated [6, 29]. However, in this case the rotor thermal management requires special attention i.e. appropriate cooling of the magnets is required or alternatively magnets with high temperature grade can be used.

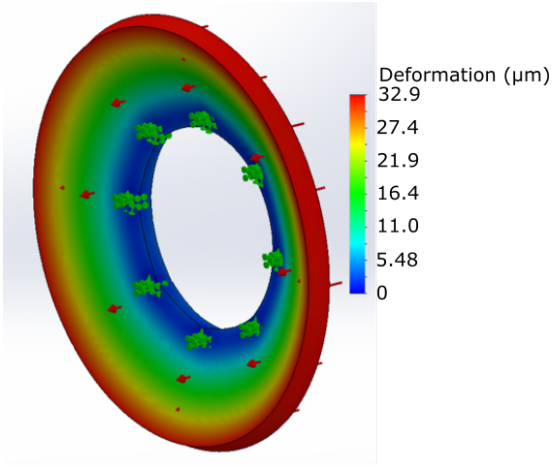

Figure 3.3: Mechanical Finite Element Analysis of the rotor deformation due to stator-rotor attraction: the maximum deformation is 33μm which is 2.2% of the airgap height

3.3.3 Concentrated Winding Tooth Coil

The prototype YASA AFPMSM consists of 24 concentrated winding tooth coils as was already illustrated in Figures 3.2 and 3.1. In this paragraph, the fill factor, thermal properties and AC losses of an anodized aluminum foil wound tooth coil will be discussed and compared qualitatively to its copper wire equivalent. The prototype tooth coils are shown in Fig. 3.4.

Conductor Material

Anodized aluminum foil was selected as conductor material. It consists of aluminum foil with an electrolytically grown aluminum oxide (Al_2O_3) -also known as alumina- layer on both sides of the foil. The aluminum oxide layer constitutes the electrical insulation.

In [30], it was shown that the use of aluminum conductors can result in a higher torque/power density and efficiency compared to a copper wire wound equivalent. aluminum has already been used for a long time as conductor in electric machines due to its attractive properties [30]:

- Aluminum is almost 3 times lighter than copper.
- Aluminum has a lower price volatility [31, 32] and cost [30, 33].
- Aluminum windings enable an increased recyclability of an electric motor [30].

Figure 3.4: Prototype tooth coils: (left) enamelled copper wire (right) anodized aluminum foil

- The use of aluminum in electric motors has a lower impact on the environment compared to copper [34]

However, the electrical conductivity of aluminum is 37% lower than that of copper which reduces the torque density significantly [35]. To overcome this issue and make aluminum a viable competitor to copper in terms of torque density, researchers have relied on innovative techniques to manufacture preformed aluminum coils with round [16, 30], flat [33, 34, 36–41] or foil [42] conductors. Preformed coils exhibit a high fill factor and a good thermal conductivity which are both attractive features when designing high torque density motors [39, 43–45]. A limitation of the use of preformed coils is the requirement to use either a segmented or separated teeth stator [46], or stator teeth with open slots [47, 48]. Additionally, existing electric motors with aluminum conductors typically use organic insulation [30, 33, 39, 42]. Despite its excellent insulating and mechanical properties, its poor thermal conductivity limits the heat transfer in the winding body [16].

In this article, the use of an anodized aluminum foil in a YASA AFPMSM is proposed to overcome these issues. This will be illustrated in the following paragraphs. In the past, anodized aluminum foil has already been used in inductors, transformers and electromagnets [49–52] because of its attractive features:

- The aluminum oxide electrical insulation has a high thermal conductiv-

ity (approximately 1.6 W/mK [53])

- The inorganic anodization layer allows a higher operating temperature [50, 51, 54, 55].

Fill Factor

A high fill factor reduces the DC resistance and hence the losses, resulting in a higher torque density. A very high fill factor can be obtained in a YASA Axial Flux machine topology with anodized aluminum foil, since:

- The YASA Axial Flux machine topology is particularly suited for a foil winding: the inherent segmented structure allows winding of the coils prior to assembly, this allows to use (semi-)closed slots. In radial flux machines, either open slot [48] or a segmented stator [46] are required if a foil winding is used.
- Foil windings allow a high fill factor [48, 56].
- Anodized aluminum foil allows very thin electrical insulation: for very thin copper foils (<0.5 mm), the fill factor drops drastically since the typical insulation thickness for thin copper foils is a multiple of 50 μm [56]. Given the number of turns and the slot area, the foil thickness of the prototype YASA AFPMSM is 86 μm. This would result in an unacceptably low fill factor when using the same insulation as used for copper foil. However, aluminum-oxide electrical insulation layers can be as thin as 3 μm [57].
- Using a foil winding in a YASA Axial Flux machine topology allows to eliminate the free space between adjacent tooth coils as illustrated in Fig. 3.5.

Fig. 3.4 shows a single tooth with anodized aluminum foil and a tooth coil with enamelled copper wire for comparison. The main parameters of both coils are given in Table 3.2. The aluminum foil was anodized via an industrial continuous anodizing process. The process parameters are the intellectual property of the anodized aluminum foil supplier.

It might be argued from looking at Fig. 3.4 that the aluminum foil coil occupies more slot area, this is caused by the springiness of the aluminum. However after assembly into the stator, it can be seen from Fig. 3.6 that both coils occupy the same slot area. It is worth stressing that both tooth coils exhibit approximately the same DC resistance despite the higher resistivity of aluminum. This is due to the very high fill factor of anodized aluminum foil YASA AFPMSM. Hence, a YASA Axial Flux machine topology with anodized

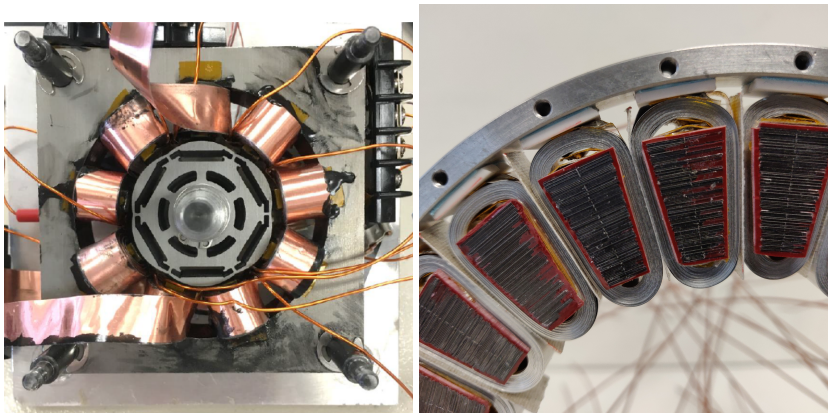

Figure 3.5: Foil wound electric machines: (left) Radial flux machine with significant free space between adjacent coils [48] (right) Prototype YASA AFPMSM prior to epoxy impregnation, only mica sheet (0.2 mm) between adjacent coils

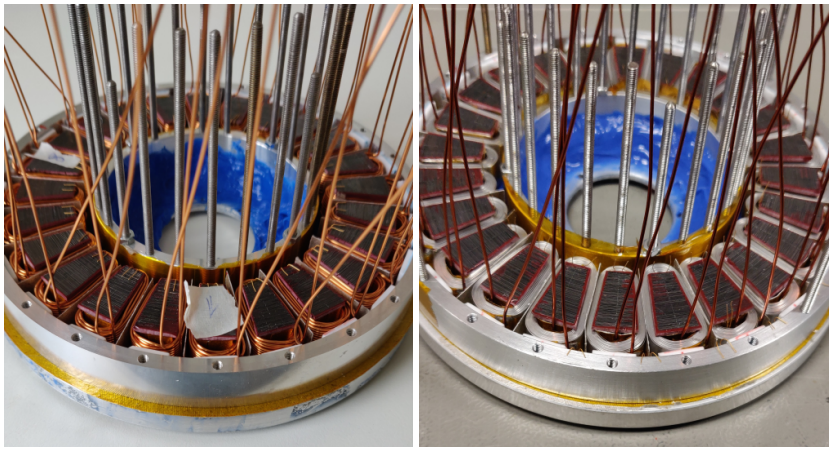

Figure 3.6: Round copper wire (left) and anodized aluminum foil (right) stator prototypes prior to epoxy impregnation

foil winding offers designers an option to increase the fill factor in small electric motors for robotic applications, which was previously only possible for motors with segmented stators or open slots. Note that round copper wire was not chosen arbitrarily as benchmark case. The majority of electric motors for robotics applications uses round wire conductors [58–60].

Table 3.2: Specifications of the prototype tooth coil

Enamelled round copper wire (Grade I, IEC 60317-13)	**Symbol**	**Value**	**Unit**
Nominal outer diameter	$d_{\text{Cu,o}}$	0.8425	mm
Conductor diameter	$d_{\text{Cu,i}}$	0.8	mm
Height laminated iron core	h_{core}	20	mm
measured DC resistance (at 25°C)	$R_{\text{DC,Cu}}$	94.54	mΩ
Weight of tooth coil	$m_{\text{Cu+SiFe}}$	31.3	g
Resistivity copper (100% IACS)	ρ_{Cu}	$1.72 \cdot 10^{-8}$	Ωm
Dielectrical strength (acc. to IEC 60317-0-1)	E_{max}	87	V_{RMS}/μm
Price/kg		16.64	EUR/kg
Anodized aluminum foil (all values according to supplier datasheet)			
foil width	h_{Al}	10	mm
total foil thickness	$t_{\text{Al,tot}}$	86	$^{\text{A}}\mu$m
thickness alumina insulation layer	t_{AlOx}	4.6	$^{\text{A}}\mu$m
Height laminated iron core	h_{core}	20	mm
measured DC resistance (at 25°C)	$R_{\text{DC,Al}}$	95.83	mΩ
Weight of tooth coil	$m_{\text{Al+SiFe}}$	25.8	g
Resistivity aluminum	ρ_{Al}	$2.74 \cdot 10^{-8}$	Ωm
Dielectrical strength (acc. to ISO 2376)	E_{max}	26.5	V_{RMS}/μm
Price/kg		685[1]	EUR/kg

[1]Note that this is the cost for a minimum order quantity of 2 kg, for larger order quantities the cost will be lower.

Thermal Properties

The use of inorganic aluminum oxide insulation improves the thermal conductivity of the winding body. This was already shown experimentally for a winding material sample in [61]. The authors measured an equivalent thermal conductivity of 6.5 W/mK for the anodized aluminum wire sample and 2.5 W/mK for the enamelled copper wires sample. The improved thermal behaviour was also shown in a simulation study for the case of an automotive solenoid actuator in [57]. Moreover, a foil winding allows a high fill factor and exhibits superior thermal properties as was reported for copper foil windings in [48, 62]. Hence, both the use of aluminum oxide insulated aluminum conductors and the foil winding topology promise to improve the thermal properties and hence the torque density. Additionally, the good thermal conductivity in the plane of the foil opens opportunities to cool the windings effectively via

the airgap both in radial and axial flux machines. A thorough thermal comparison of an anodized aluminum foil winding and enamelled round copper wire winding in a YASA AFPMSM can be found in [63].

AC Losses in Foil Coils

Several authors have studied AC winding losses in foil wound rotating electrical machines [47, 64, 65]. They have concluded that AC winding losses can be an important part of the total winding losses especially in high-speed machines. They recommended to use foil windings only in low speed applications [64] and/or in case of short axial length in case of axial flux machines or short slot height in case of radial flux machines [66]. The axial length of the prototype YASA AFPMSM is kept short (15 mm) and the electrical frequency at 300 rpm is 65 Hz, hence no significant increase in AC losses is expected. However, at 2400 rpm the electrical frequency is 520 Hz, potentially resulting in a significant contribution of the AC losses, making this prototype YASA AFPMSM more suitable for direct-drive applications.

3.4 Manufacturing Aspects

The nature of the anodized aluminum foil conductor material and the small size of the stator core elements gives rise to manufacturing challenges not frequently encountered in electric machine production. Identification of these challenges is important to guide further research efforts concerning the use of anodized aluminum foil. In this section, challenges are identified an possible solutions are discussed.

3.4.1 Aluminum Foil Annealing

The temper of the anodized aluminum foil was H18, which means it was strain hardened. In industrial foil winding processes, the foil tension is continuously controlled. However, this is not possible in a manual winding process, resulting in a voluminous coil body with large air gaps between the foil layers due to the spring-back behaviour of the strain-hardened aluminum foil. An annealing process was carried out under atmospheric conditions to soften the aluminum foil, make it more ductile and reduce the spring-back during winding. The foil was put into an oven which was heated to 412 °C at a rate of 100°C/h. It was kept at this temperature for 3 hours and then slowly cooled down (uncontrolled). In Fig. 3.7, the spring-back behaviour of annealed and non-annealed foil are compared qualitatively for a coil with 15 turns. It can be concluded that annealing significantly reduces the spring-back behaviour.

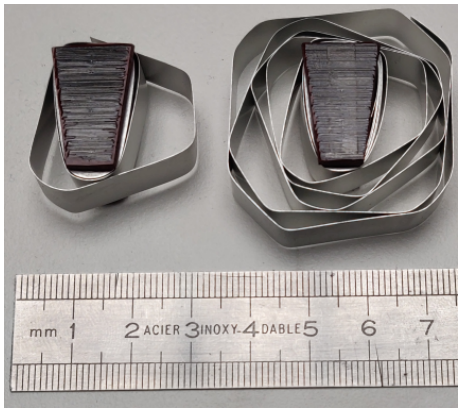

Figure 3.7: Influence of annealing process on spring-back behaviour of aluminum foil: (left) annealed foil (right) non-annealed foil, temper H18

Figure 3.8: Epoxy potted stator tooth tips before (left) and after (right) mechanical grinding

3.4.2 Adhesive Bonding of Iron Core Laminations

Given the small size of the iron core elements, bonding of the core laminations appeared to be quite difficult. Several manufacturers of stator stacks reported that they could not guarantee the mechanical integrity of the small core elements produced from laminations with pre-applied bonding varnish. Therefore a very low viscosity two-part epoxy (Loctite Stycast 3050 + Cat 28) was used to pot the stator tooth tips only. The result can be seen in Fig. 3.8. The low viscosity epoxy flowed between the laminations, effectively bonding the stack, and guaranteeing the mechanical integrity even after the large burr around the tooth tip was removed by mechanical grinding.

3.5 Electrical Interconnection Methods

The high melting temperature of the aluminum-oxide insulation layer makes it very difficult to solder aluminum conductors to each other or to copper using regular lead-based solder and flux for electronic applications. In [30], cold-pressure welding was used to establish a wire-to-wire interconnection. However given the limited thickness of the foil considered in this work, this interconnection process was not an option. This section describes several interconnection methods for foil-to-wire that have been tested experimentally, their performance is discussed and compared qualitatively. The dimensions of the used foil and wire are given in Table 3.2. Copper wire was selected to connect the aluminum foil coils to an external device since it exhibits superior handling and manipulation capabilities compared to foil. In the considered methods in this section, the wire is connected orthogonally to the foil. The interconnection methods will be evaluated with respect to two criteria: (1) realizing a stable electrical contact (2) Providing sufficient mechanical strength during the assembly process of the motor. Epoxy resin provides the necessary mechanical strength after assembly and impregnation.

3.5.1 Soldering on Electrolytic Nickel-Plated Aluminum

The authors of [56] recommended nickel plating of the aluminum surface prior to soldering. An electrolytic nickel plating and soldering process was developed in this work. A 0.9 mm diameter copper wire soldered on nickel plated aluminum foil (86 μm thickness) is shown in Fig. 3.9. Kapton® tape was used to protect the aluminum-oxide layer of the untreated surface. Pretreatment of the nickel-plated aluminum foil surface is an absolute requirement for obtaining a stable and solderable nickel coating. This involves degreasing, removing of the aluminum-oxide layer by etching in 5 wt% NaOH solution, and finally a dip in a zincate solution (33 wt% zincate), this removes the aluminum oxide and applies a layer of zinc to prevent re-oxidation. The process parameters of the electrolytic nickel coating strongly depend on the electrolyte concentration and electrode geometries and should therefore be determined for each case individually. To validate the mechanical properties a complete stator prototype was assembled as shown in Fig. 3.6; it was impregnated with epoxy resin and cured for 4 hours at 120°C. The electrical resistance of the coils was measured before and after the potting process using an LCR-meter. The average electrical resistance before potting was 95.83 $\pm$0.67 Ω and 96.08 $\pm$0.60 after potting. Hence, no significant increase in electrical resistance of the coil was observed after potting. This indicates that the developed nickel plating and soldering method guarantees sufficient mechanical strength during the assembly process prior to epoxy impregnation and results in a stable electrical contact.

Figure 3.9: Soldered copper wire (0.9 mm diameter) to nickel plated aluminum foil with lead-free solder paste (Sn96.5/Ag3.5)

On a laboratory scale, the nickel-plating and soldering process is quite time-consuming since it requires a large number of process steps (approx. 15 minutes per terminal), and because the foil should be handled with great care to avoid damaging during manipulation. Moreover, the quality of the nickel coating is very sensitive to variations of the process parameters; e.g. regularly replacing the electrolyte was required to obtain a solderable nickel coating. However, since both the nickel-plating and soldering are well-established industrial processes, this interconnection method can be automated. This would significantly decrease the process time and maybe more important: increase the repeatability.

3.5.2 Ultrasonic Welding

Ultrasonic welding [67] was recommended by the manufacturer of the anodized foil for foil-to-foil interconnections [49]. Therefore, the use of ultrasonic welding for foil-to-wire interconnections is explored in this work.

Ultrasonic Welding Device

The ultrasonic welding devices used in this work is the Telsonic MPX as shown in Fig. 3.10. It uses a fixed mechanical vibration frequency of 20 kHz and has a maximum power of 3.6 kW. The welding amplitude, time and force can be varied to optimize the weld quality. The vibration amplitude can vary between 33μm (50%) and 66μm (100%). This work aims to find the welding parameters that result in maximal weld strength.

Figure 3.10: Ultrasonic welding press Telsonic MPX used in this work

Description of Experiments

The interesting range for each parameter (amplitude, time and pressure) was determined using exploratory welds. To improve the repeatability of the experiments, a special clamping module was constructed as shown in Fig. 3.11 to obtain a repeatable positioning of the foil and wire. Note that clamping of the foil can only be used during a test phase to find the optimal parameters. Once the parameters are found, clamping should be avoided since it can damage the insulation of the foil. The enamel of the copper wire was removed mechanically before welding, the aluminum oxide was not removed from the aluminum foil. The explored parameter combinations can be found in Table 3.3. For each combination at least 4 welds are performed, three welds are used for tensile strength tests and the fourth is subject to a metallographic examination.

Tensile Test Results

The tensile strength of the welds are determined using the MultiTest2.5-dV motorised force tester with the AFG 50 loadcell. To subject the weld to a pure shear force, the foil is fully clamped between two metal plates, with a recess in the metal plates at the location of the copper wire. The test configuration is schematically shown in Fig. 3.12. The results of the tensile test can be found in Table 3.3. The strongest welds are obtained for the highest amplitude and shortest welding time, these welds also exhibit the highest repeatability. For all parameter combinations, the Olympus MX51 microscope was used to examine a metallographic cross-section. For the poor welds, more remains of the aluminum oxide (black flakes) were visible in the weld zone resulting in a poor bond between the copper and aluminum, the influence of removing the alu-

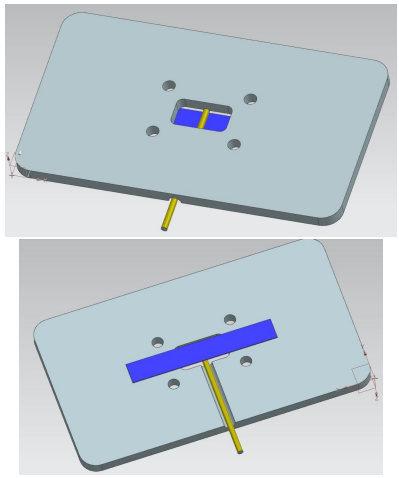

Figure 3.11: Clamping module used to secure the workpieces in a repeatable manner with a cut-out for the sonotrode, aluminum foil in dark blue and copper wire in yellow: (a) top view (b) bottom view with cut-out for wire

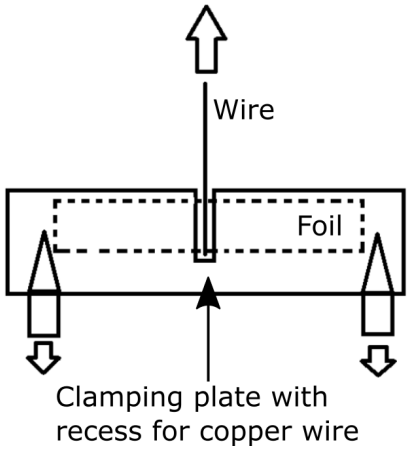

Figure 3.12: Schematic representation of the tensile strength test

minum oxide prior to welding should therefore be studied in future research. Moreover, due to the pressure and vibrations, the copper wire tends to penetrate into the aluminum foil especially for large pressures and welding times. This is clearly shown in Fig. 3.13a. For a good weld, very little remains of the aluminum-oxide are present in the weld zone and the weld exhibits a large contact surface (see e.g. Fig. 3.13b).

Table 3.3: Tensile strength for the tested welding parameter combinations

Parameters			**Results**
amplitude [%]	time [s]	pressure [bar]	tensile strength mean (±std) [N]
50	0.2	0.2	21.3±8
50	0.2	0.8	17.3±15
50	0.6	0.2	17.9±16
50	0.6	0.8	0
70	0.2	0.2	38.7±5
70	0.2	0.8	34.7±2.8
70	0.6	0.2	14.8±13
70	0.6	0.8	13.9±13

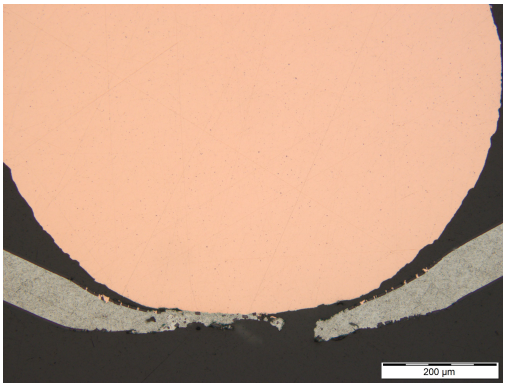

(a) Poor weld (Amplitude 70%, time: 0.6s, pressure: 0.2 bar)

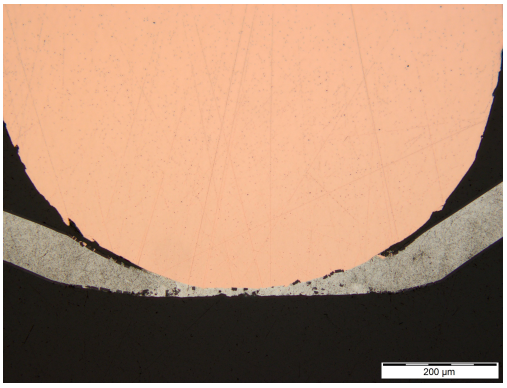

(b) Good weld (Amplitude 50%, time: 0.2s, pressure: 0.2 bar)

Figure 3.13: Metallographic examination of the weld

3.5.3 Conclusion

Despite sufficient mechanical strength was obtained for certain parameter combinations with the ultrasonic welding process, due to the issue of damaging the insulation during the welding, this method was not used for the foil-to-wire interconnections in the prototype motor. Instead, the nickel-plating and soldering interconnection method was used although it is very time consuming. Other interesting interconnection methods that are not discussed in this work are electron-beam welding and laser welding [51].

3.6 Conclusion and Future Work

To fulfil the need for higher torque density electric motors in novel robotic applications, a YASA AFPMSM with anodized aluminum foil winding was proposed in this work. Considering its high fill factor and excellent thermal properties, it can be concluded that this motor topology and winding material combination is an attractive candidate to push the torque density limit, especially in small, pancake-shaped motors for (quasi-)direct-drive robotic applications. In future work, the torque density of the anodized aluminum foil prototype YASA AFPMSM will be evaluated experimentally and compared to the torque density of its copper wire equivalent.

Regarding the manufacturing aspects, creating a galvanic contact between the aluminum foil and a copper terminal wire appeared to be the most challenging aspect. However, it was demonstrated in this work that a galvanic contact could be obtained through both soldering copper wire to nickel-plated aluminum foil and ultrasonic welding.

References

[1] F. Ostyn, B. Vanderborght, and G. Crevecoeur, "Design and control of a quasi-direct drive robotic gripper for collision tolerant picking at high speed," *IEEE Robotics and Automation Letters*, pp. 1–8, 2022.

[2] G. Kenneally, A. De, and D. E. Koditschek, "Design principles for a family of direct-drive legged robots," *IEEE Robotics and Automation Letters*, vol. 1, pp. 900–907, 7 2016.

[3] A. Singh, N. Kashiri, and N. Tsagarakis, "Design of a quasi direct drive actuator for dynamic motions." MDPI, 11 2020, p. 8516.

[4] P. M. Wensing, A. Wang, S. Seok, D. Otten, J. Lang, and S. Kim, "Proprioceptive actuator design in the mit cheetah: Impact mitigation and

high-bandwidth physical interaction for dynamic legged robots," *IEEE Transactions on Robotics*, vol. 33, pp. 509–522, 6 2017.

[5] S. Yu, T. H. Huang, X. Yang, C. Jiao, J. Yang, Y. Chen, J. Yi, and H. Su, "Quasi-direct drive actuation for a lightweight hip exoskeleton with high backdrivability and high bandwidth," *IEEE/ASME Transactions on Mechatronics*, vol. 25, pp. 1794–1802, 8 2020.

[6] J. Hollerbach, I. Hunter, J. Lang, S. Umans, R. Sepe, E. Vaaler, and I. Garabieta, "The mcgill/mit direct drive motor project." IEEE Comput. Soc. Press, pp. 611–617.

[7] Igus rebel: Fully integrated single joint. Available at https://www.igus.eu/info/rebel-gearbox-system (accessed: 16-05-2021).

[8] M. G. Angle, J. H. Lang, J. L. Kirtley, S. Kim, and D. Otten, "Optimization of surface-mount permanent magnet synchronous machines for low duty-cycle, high-torque applications." IEEE, 5 2017, pp. 1–6.

[9] T. Zhu, J. Hooks, and D. Hong, "Design, modeling, and analysis of a liquid cooled proprioceptive actuator for legged robots." IEEE, 7 2019, pp. 36–43.

[10] H. Zhu, C. Nesler, N. Divekar, M. T. Ahmad, and R. D. Gregg, "Design and validation of a partial-assist knee orthosis with compact, backdrivable actuation." IEEE, 6 2019, pp. 917–924.

[11] J. Urata, Y. Nakanishi, K. Okada, and M. Inaba, "Design of high torque and high speed leg module for high power humanoid." IEEE, 10 2010, pp. 4497–4502.

[12] U. Hochberg, A. Dietsche, and K. Dorer, "Evaporative cooling of actuators for humanoid robots," 10 2013.

[13] A. EL-Refaie, "Fractional-slot concentrated-windings synchronous permanent magnet machines: Opportunities and challenges," *IEEE Transactions on Industrial Electronics*, vol. 57, pp. 107–121, 1 2010.

[14] J. Hagedorn, F. S.-L. Blanc, and J. Fleischer, *Handbook of Coil Winding*, J. Hagedorn, F. S.-L. Blanc, and J. Fleischer, Eds. Springer Berlin Heidelberg, 2018.

[15] F. Meier, Ph.D. dissertation.

[16] R. Wrobel, N. Simpson, P. H. Mellor, J. Goss, and D. A. Staton, "Design of a brushless pm starter generator for low-cost manufacture and a high-aspect-ratio mechanical space envelope," *IEEE Transactions on Industry Applications*, vol. 53, pp. 1038–1048, 3 2017.

[17] H. Vansompel, P. Leijnen, and P. Sergeant, "Multiphysics analysis of a stator construction method in yokeless and segmented armature axial flux pm machines," *IEEE Transactions on Energy Conversion*, vol. 34, pp. 139–146, 2019.

[18] G. Kenneally, W.-H. Chen, and D. E. Koditschek, "Actuator transparency and the energetic cost of proprioception," 2020.

[19] H. Asada and K. Youcef-Toumi, *Direct-Drive Robots*. The MIT Press, 1987.

[20] M. Grebenstein, A. Albu-Schaffer, T. Bahls, M. Chalon, O. Eiberger, W. Friedl, R. Gruber, S. Haddadin, U. Hagn, R. Haslinger, H. Hoppner, S. Jorg, M. Nickl, A. Nothhelfer, F. Petit, J. Reill, N. Seitz, T. Wimbock, S. Wolf, T. Wusthoff, and G. Hirzinger, "The dlr hand arm system." IEEE, 5 2011, pp. 3175–3182.

[21] J. Zhu, C. Jiao, I. Dominguez, S. Yu, and H. Su, "Design and backdrivability modeling of a portable high torque robotic knee prosthesis with intrinsic compliance for agile activities," *IEEE/ASME Transactions on Mechatronics*, pp. 1–10, 2022.

[22] A. Husain. The rise of the 48v robots. Available at https://www.powerelectronicsnews.com/the-rise-of-the-48v-robots/ (accessed: 16-06-2022).

[23] J. W. Sensinger, "Selecting motors for robots using biomimetic trajectories: Optimum benchmarks, windings, and other considerations." IEEE, 5 2010, pp. 4175–4181.

[24] H. Vansompel, P. Sergeant, and L. Dupré, "Optimized design considering the mass influence of an axial flux permanent-magnet synchronous generator with concentrated pole windings," *IEEE Transactions on Magnetics*, vol. 46, pp. 4101–4107, 12 2010.

[25] M. Waldhof, A. Echle, and N. Parspour, "A novel drive train concept for personalized upper body exoskeletons with a multiphase axial flux machine." IEEE, 5 2019, pp. 2160–2166.

[26] P. Sergeant, H. Vansompel, and L. Dupré, "Influence of stator slot openings on losses and torque in axial flux permanent magnet machines," *Mathematics and Computers in Simulation*, vol. 130, pp. 22–31, 12 2016.

[27] G. Dajaku, "Advanced multi-phase fractional slot concentrated windings: characteristics and potentials," *Electrical Engineering*, vol. 103, pp. 397–406, 2 2021.

[28] S. Timoshenko, *Theory of Plates and Shells*, 1959.

[29] "Highly dynamic motors for lightweight robots and cobots," Schaeffler Gmbh, Tech. Rep., 2022.

[30] J. D. Widmer, C. M. Spargo, G. J. Atkinson, and B. C. Mecrow, "Solar plane propulsion motors with precompressed aluminum stator windings," *IEEE Transactions on Energy Conversion*, vol. 29, pp. 681–688, 9 2014.

[31] Uk-alumotor research project. Available at https://gtr.ukri.org/projects?ref=77130#/tabOverview (accessed: 16-06-2022).

[32] C. R. Sullivan, "Aluminum windings and other strategies for high-frequency magnetics design in an era of high copper and energy costs." IEEE, 2 2007, pp. 78–84.

[33] G. Cakal and O. Keysan, "Flat winding made of aluminum or copper sheet for axial flux machines," *IET Electric Power Applications*, vol. 15, pp. 429–440, 4 2021.

[34] A. Acquaviva, M. Diana, B. Raghuraman, L. Petersson, and S. Nategh, "Sustainability aspects of electrical machines for e-mobility applications part ii: Aluminium hairpin vs. copper hairpin." IEEE, 10 2021, pp. 1–6.

[35] P. Arumugam, E. Amankwah, A. Walker, and C. Gerada, "Design optimization of a short-term duty electrical machine for extreme environment," *IEEE Transactions on Industrial Electronics*, vol. 64, pp. 9784–9794, 12 2017.

[36] M. Groninger, F. Horch, A. Kock, M. Jakob, and B. Ponick, "Cast coils for electrical machines and their application in automotive and industrial drive systems." IEEE, 9 2014, pp. 1–7.

[37] C. Wohlers, P. Juris, S. Kabelac, and B. Ponick, "Design and direct liquid cooling of tooth-coil windings," *Electrical Engineering*, vol. 100, pp. 2299–2308, 12 2018.

[38] M. Bach, A. Babl, and D. Gerling, "Integration of forming manufacturing technology into the component production of innovative electric motor concepts." IEEE, 12 2020, pp. 1–8.

[39] N. Simpson, D. J. North, S. M. Collins, and P. H. Mellor, "Additive manufacturing of shaped profile windings for minimal ac loss in electrical machines," *IEEE Transactions on Industry Applications*, vol. 56, pp. 2510–2519, 5 2020.

[40] F. Wu, A. EL-Refaie, and A. Al-Qarni, "Additively manufactured hollow conductors integrated with heat pipes: Design tradeoffs and hardware demonstration," *IEEE Transactions on Industry Applications*, vol. 57, pp. 3632–3642, 7 2021.

[41] A. Selema, M. N. Ibrahim, and P. Sergeant, "Additively-manufactured ultra-light shaped-profile windings for hf electrical machines and weight-sensitive applications," *IEEE Transactions on Transportation Electrification*, pp. 1–1, 2022.

[42] P. Melendez-Vega and G. Venkataramanan, "Aluminum foil coils for human scale wind turbines." IEEE, 10 2012, pp. 1–5.

[43] R. Wrobel and P. Mellor, "Design considerations of a direct drive brushless machine with concentrated windings," *IEEE Transactions on Energy Conversion*, vol. 23, pp. 1–8, 3 2008.

[44] M. Galea, T. Hamiti, and C. Gerada, "Torque density improvements for high performance machines." IEEE, 5 2013, pp. 1066–1073.

[45] S. Ayat, H. Liu, M. Kulan, and R. Wrobel, "Estimation of equivalent thermal conductivity for electrical windings with high conductor fill factor." IEEE, 9 2018, pp. 6529–6536.

[46] P. Arumugam, T. Hamiti, and C. Gerada, "Fault tolerant winding design - a compromise between losses and fault tolerant capability," 2012, pp. 2559–2565.

[47] C. Gerada, "Estimation of eddy current loss in semi-closed slot vertical conductor permanent magnet synchronous machines considering eddy current reaction effect," *IEEE Transactions on Magnetics*, vol. 49, pp. 5326–5335, 2013.

[48] M. Rios and G. Venkataramanan, "Design and construction of a foil winding permanent magnet machine." IEEE, 10 2020, pp. 2026–2033.

[49] Applications of anodised aluminium foil. Available at https://anofol.de/anwendungen (accessed: 16-05-2021).

[50] R. D. Carlson and R. J. Schiltz, "Power transformer for use in highly radioactive environments," Argonne National Laboratory (ANL), Tech. Rep., 8 1961.

[51] H. Jordan, "Anodized aluminum foil coil with 538° c capabilities. final report," Historical Energy Database (United States), Tech. Rep., 11 1980.

[52] D. A. Hewitt, "Approaches to improving thermal performance of inductors with a view to improving power density," Ph.D. dissertation, 2015.

[53] A. Cai, L. P. Yang, J. P. Chen, T. G. Xi, S. G. Xin, and W. Wu, "Thermal conductivity of anodic alumina film at (220 to 480) k by laser flash technique," *Journal of Chemical and Engineering Data*, vol. 55, pp. 4840–4843, 11 2010.

[54] S. Babicz, S. A. A. Djennad, and G. Velu, "Preliminary study of using anodized aluminum strip for electrical motor windings." Institute of Electrical and Electronics Engineers Inc., 12 2014, pp. 176–179.

[55] S. Babicz, S. Ait-Amar, G. Velu, A. Cavallini, and P. Mancinelli, "Behavior of anodized aluminum strip under sine and square wave voltage," *IEEE Transactions on Dielectrics and Electrical Insulation*, vol. 24, pp. 39–46, 2 2017.

[56] V. C. Valchev and A. V. den Bossche, *Inductors and Transformers for Power Electronics*. CRC Press, 10 2018.

[57] L. Reissenweber, A. Stadler, J. v. Lindenfels, and J. Franke, "Improved thermal behavior of an electromagnetic linear actuator with different winding types and the influence on the complex impedance." IEEE, 12 2019, pp. 1–6.

[58] "Tecnotion: Frameless torque motor series," Tecnotion, Tech. Rep., 2019.

[59] "Ilm frameless servo kits," TQ-Robodrive, Tech. Rep., 2020.

[60] "Kollmorgen frameless motor selection guide," Kollmorgen, Tech. Rep., 2012.

[61] N. Simpson, R. Wrobel, and P. H. Mellor, "Estimation of equivalent thermal parameters of impregnated electrical windings," *IEEE Transactions on Industry Applications*, vol. 49, pp. 2505–2515, 11 2013.

[62] M. Rios, G. Venkataramanan, A. Muetze, and H. Eickhoff, "Thermal performance modeling of foil conductor concentrated windings in electric machines," *IEEE Transactions on Industry Applications*, vol. 54, pp. 4104–4113, 9 2018.

[63] J. Van Damme, H. Vansompel, and G. Crevecoeur, "Anodised aluminium foil winding axial flux machine for direct-drive robotic applications (under review)," *IEEE Transactions on Industrial Electronics*, 2022.

[64] P. Arumugam, T. Hamiti, C. Brunson, and C. Gerada, "Analysis of vertical strip wound fault-tolerant permanent magnet synchronous machines," *IEEE Transactions on Industrial Electronics*, vol. 61, pp. 1158–1168, 3 2014.

[65] R. M. Wojciechowski and C. Jedryczka, "The analysis of stray losses in tape wound concentrated windings of the permanent magnet synchronous motor," *COMPEL - The international journal for computation and mathematics in electrical and electronic engineering*, vol. 34, pp. 766–777, 5 2015.

[66] F. Franchini, E. Poskovic, L. Ferraris, A. Cavagnino, and G. Bramerdorfer, "Application of new magnetic materials for axial flux machine prototypes." IEEE, 5 2017, pp. 1–6.

[67] M. Matheny and K. Graff, *Ultrasonic welding of metals*. Elsevier, 2015.

Chapter 4

Anodized Aluminum Foil Winding Axial Flux Machine for Direct-Drive Robotic Applications

This chapter aims to address the first challenge mentioned in Section 1.4: the poor fill factor and thermal conductivity of a round enamelled copper wire winding.

The performance of even the best design is eventually limited by the properties of the used materials and manufacturing methods. Therefore, to realize a significant leap in the torque density of the electric motor in a quasi-direct-drive robotic actuator, the use of a novel type of conductor is studied in this chapter: anodized aluminum foil. Today, most small actuators for robot applications use round enamelled copper wire. With anodized aluminum foil, an aluminum-oxide layer constitutes the turn-to-turn electrical insulation. This ceramic material exhibits a higher thermal conductivity and temperature limit compared to the organic enamel. Also, aluminum is three times lighter than copper and a foil can be stacked more efficiently than a wire resulting in a higher fill factor.

On the other side, aluminum features a higher resistivity resulting in high DC winding losses. Due to the cross-slot flux impinging the large foil surface, the AC winding losses tend to be higher, however this might be partially counteracted by the higher resistivity of aluminum.

The discussion here above illustrates that anodized aluminum foil will not lead to a higher torque density in all design scenarios. To learn in which scenarios it might lead to a higher torque density, the use of anodized aluminum foil in an axial flux permanent magnet synchronous machine is studied in this

chapter. The geometrically and electromagnetically identical electrical machine with round enamelled copper wire from the IMD in Chapter 2 will serve as a benchmark. First, the DC and AC winding losses are evaluated experimentally by measuring the resistance of the stator winding for various frequencies. Subsequently, the influence of the type of conductor on the thermal properties of a single tooth coil and a complete stator are evaluated. A 3D thermal Finite Element (FE) model is then constructed based on the experimental data. This model is used to study the influence of various design parameters on the torque density for both types of conductor. Finally, each motor is put on a testbench to compare the torque density experimentally.

The title of this chapter puts the focus on direct-drive robotic applications because the rotational speed of the motor remained below 350 rpm during all experiments mentioned in this chapter. The motor was not tested at higher rotational speeds to avoid the risk of irreversible damage due to mechanical issues related to limited mechanical balancing and bearing alignment.

Anodized Aluminum Foil Winding Axial Flux Machine for Direct-Drive Robotic Applications

Adapted from: J. Van Damme, H. Vansompel and G. Crevecoeur, "Anodized Aluminum Foil Winding Axial Flux Machine for Direct-Drive Robotic Applications," in *IEEE Transactions on Industrial Electronics*, vol. 70, no. 10, pp. 10409-10419, Oct. 2023, doi: 10.1109/TIE.2022.3220894.

Abstract: There is a need for higher torque density electric actuators in novel direct-drive robotic applications. Since the torque density is inherently limited by material properties, designers have to look at novel materials to push the torque density limit further. In this article, anodized aluminum foil is considered as an alternative to enamelled copper wire in a yokeless and segmented armature axial flux machine. This machine topology has a high torque density and is particularly suited for an anodized aluminum foil winding. The DC resistance, thermal properties and eventually the torque density of a prototype test case machine are compared for both winding materials. A 3D thermal finite element model is used to analyse the influence of the thermal interface between winding body and housing, and the influence of the cooling performance on the torque density. To conclude, anodized aluminum foil winding offers a higher torque density in direct-drive yokeless and segmented armature axial flux actuators where the winding body thermal resistance is dominant in the thermal path from heat source to heat sink. It is experimentally shown that for the prototype machine, the torque per kg active stator mass increases 13% through the use of anodized aluminum foil.

4.1 Introduction

Electric machines with high torque density (Nm/kg) are gaining interest to advance upon the development of novel (quasi-)direct-drive robotic applications [1–4]. The Yokeless And Segmented Armature Axial Flux Permanent Magnet Synchronous Machine (YASA AFPMSM) topology is an interesting candidate for these applications since it allows to obtain a high torque density due to

a high fill factor and the absence of a stator yoke [5, 6]. This topology was already considered for a direct-drive articulated robot in [7] and quasi-direct-drive exoskeleton actuator in [8]. However, a key challenge is that the torque density is inherently limited by material temperature limits [9]. Therefore researcher have started to look at alternative materials to further increase the torque and/or power density. In [10], it was shown that aluminum conductors offer an interesting alternative to copper. Already for a long time, aluminum as conductor material has been used in electric machines due to its attractive properties [10]:

- Aluminum is almost 3 times lighter than copper.
- Aluminum has a lower price volatility [11] and cost [10, 12].
- Aluminum windings enable an increased recyclability of an electric motor [10].
- The use of aluminum in electric motors has a lower impact on the environment compared to copper [13]

However, the electrical conductivity of aluminum is 37% lower than that of copper. Although this can be beneficial for high-frequency machines [14], it is often detrimental for the torque density of low frequency machines where DC winding losses tend to dominate [15]. To overcome this issue and make aluminum a viable competitor to copper in terms of machine torque density, researchers have relied on innovative techniques to manufacture preformed aluminum coils with round [10, 16], flat [9, 12–14, 17–20] or foil [21] conductors. Preformed coils exhibit a high fill factor and a good thermal conductivity which are both attractive features when designing high torque density motors [19, 22–24]. However, existing electric motors with aluminum conductors typically use organic insulation [10, 12, 19, 21]. Despite its excellent insulating and mechanical properties, its poor thermal conductivity limits the heat transfer in the winding body [16].

In this article, the use of an anodized aluminum foil is proposed to overcome this issue. It consists of aluminum foil with an electrolytically grown aluminum oxide (Al_2O_3) -also known as alumina- layer on both sides of the foil. In the past, anodized aluminum foil has already been used in inductors, transformers and electromagnets [25–27] because of its attractive features:

- Aluminum oxide has a high thermal conductivity (approximately 1.6 W/mK [28]) which allows to significantly increase the thermal conductivity of the winding body [24].
- The inorganic anodization layer allows an operating temperature up to 500°C [26, 29].

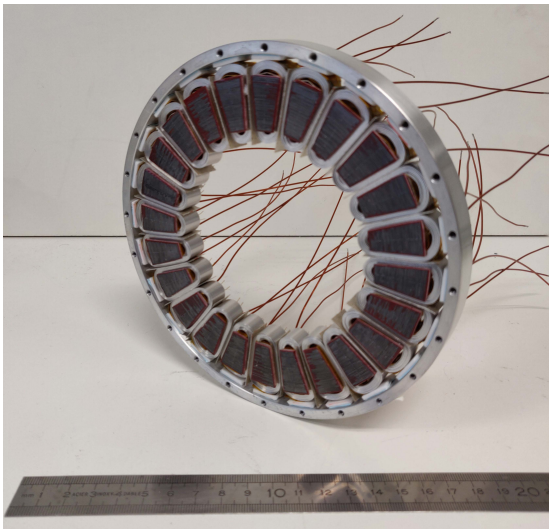

Figure 4.1: Prototype axial flux machine stator with anodized aluminum foil tooth coils (before potting)

The use of inorganic aluminum oxide insulation improves the thermal conductivity of the winding body. This was already shown experimentally for a winding material sample in [24] and in a simulation study for an automotive solenoid actuator in [30]. Moreover, a foil winding allows a high fill factor and exhibits superior thermal properties as was reported for copper foil windings in [31, 32]. Hence, both the use of aluminum oxide insulated aluminum conductors and the foil winding topology promise to improve the torque density.

This paper aims to evaluate the torque density of a YASA AFPMSM with anodized aluminum foil winding in comparison to an electromagnetically identical machine with enamelled copper wire. The influence of the thermal interface between winding body and housing, and the influence of the cooling performance will be studied specifically.

First, Section 4.2 motivates the need for higher torque density motors in direct-drive robot applications and specifies the test case YASA AFPMSM that will be used throughout this comparative study. Subsequently, in Section 4.3 the winding losses are analysed and compared for both an anodized foil winding and a copper wire winding YASA AFPMSM. In Section 4.4, the equivalent thermal properties of a winding body are determined experimentally and compared for both winding materials. These parameters are used in 3D thermal Finite Element (FE) model of the test case YASA AFPMSM to study the influence of the thermal interface between winding body and housing on the stator thermal performance. Finally, in Section 4.5, the torque density of the test case YASA AFPMSM is determined experimentally for both winding materials,

Table 4.1: Application requirements for electric motors in (quasi-)direct-drive robotic actuators

Requirement	Motivation
High (specific) torque	System torque density $>$ 10Nm/kg [1, 34]
Low speed	Maximum 300 rpm in direct-drive applications [1, 2] Maximum 3000 rpm for quasi-direct-drive applications [35]
Low DC bus voltage	To ensure sufficient electrical safety, a common DC bus voltage level is 48 V [36, 37].
Pancake-shaped motor	Offers highest torque density if the mass is constrained in low gear ratio actuators [3].

and the influence of the cooling performance on the torque density is studied using the losses from Section 4.3 and the thermal model from Section 4.4.

4.2 YASA Axial Flux PMSM for Direct-Drive Robot Applications

In novel robotic applications such as cobots, legged mobile robots, exoskeletons, and collision tolerant grippers there is the tendency to go towards (quasi-)direct drive actuators. They have a gear ratio ranging between 1:1 to 10:1 [33]. (Quasi-)Direct drive actuators inherently have a higher backdrivability which enables safer, more dexterous and dynamic robots which are capable of dealing with uncertain, unstructured and changing environments [2–4, 33].

Despite the attractive features offered by (quasi-)direct-drive actuators they suffer from a low torque density caused by their low gear ratio. This limits the robot performance. For example, for an articulated robot to handle a useful payload, a system torque density of at least 10 Nm/kg is required according to [1, 34]. Additional requirements for the electric motor in (quasi-)direct-drive actuators are given in Table 4.1.

As already mentioned in the introduction, the YASA AFPMSM holds high potential to further push the torque density limits for robotic applications [6]. Table 4.2 gives the design parameters of the test case YASA AFPMSM used in this work. The stator of the test case machine with anodized aluminum foil winding is shown in Fig. 4.1 for illustration. An analytical electromagnetic model for the flux distribution in the stator core from [38] was used to calculate

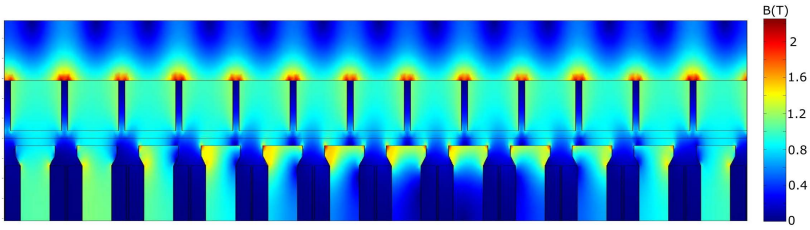

Figure 4.2: 2D finite element magnetostatic simulation of the magnetic flux density at the inner radius for a phase current density of $5 A_{\text{RMS}}/\text{mm}^2$

the number of turns that satisfies the DC bus voltage and maximum speed requirements of Table 4.1. The final design was simulated using a multislice 2D finite element magnetostatic model to check for excessive saturation in the stator teeth. Fig. 4.2 shows the magnetic flux density at the inner radius of the machine for a current density of 5 $A_{\text{RMS}}/\text{mm}^2$. It is clear that the stator teeth do not exhibit excessive saturation. In fact the maximum flux density in the iron stator teeth is only around 1.3 T which is much smaller than the saturation flux density. Note that the electromagnetic design was based on first hand design rules and previous experience from [6, 38] and has not been the subject to a thorough optimization. Although a higher flux density in the iron is possible and would also increase the efficiency and continuous torque, it would also reduce the peak torque which might be an equally important metric in robotic applications.

This test case machine is used throughout this work to evaluate the use of anodized aluminum foil. This is done by comparing its performance in terms of winding losses, thermal properties and torque density to a benchmark situation. An electromagnetically identical machine with enamelled copper wire and with the same number of turns per tooth coil is chosen as benchmark because most electric motors in robotic applications use this type of conductor [36]. The conductor dimensions and properties for both the enamelled round copper wire and anodized aluminum foil are given in Table 4.3. Note that the dielectric strength of the anodized aluminum foil conductors is more than three times lower compared to enamelled copper wire moreover, this dielectric strength strongly decreases with decreasing bending radius of the foil. Because aluminum-oxide is a ceramic material, it is brittle. Hairline cracks start to appear on the surface of the foil when it is bend. It was shown in [29] that when arcing happens, it is typically between two opposed cracks. The manufacturer reported a breakdown voltage of 194.2 V_{RMS} for a bending radius of 5 mm, hence breakdown will not occur in the considered test case machine since the total DC bus voltage is only 48 V.

Table 4.2: Specifications of the test case YASA AFPMSM

Parameter	Symbol	Value	Unit
Three-phase inverter DC bus voltage	V_{DC}	48	V
Maximum speed	Ω_{max}	300	rpm
Number of pole pairs	N_{p}	13	/
Number of slots	Q_{s}	24	/
Number of phases	n_{ph}	3	/
Number of turns per tooth coil	n_{turns}	35	/
Outer diameter stator iron core	D_{o}	138.5	mm
Inner diameter stator iron core	D_{i}	98.5	mm
Axial length stator iron core	h_{stat}	15	mm
Axial slot length	h_{slot}	10	mm
Total axial length (incl. housing)	l_{tot}	62.5	mm
Slot width	b_{slot}	6	mm
Airgap thickness	h_{air}	1.5	mm
Magnet height	h_{mag}	5	mm
Rotor yoke height	h_{mag}	6	mm

Fig.4.3a gives a CAD drawing of the test case machine, the realised prototype is shown in Fig. 4.3b. The stator is impregnated with epoxy resin for mechanical stability [6]. This also protects the edges of the foil which are very prone to deformation due to the limited thickness of the foil, the impregnation also improves the thermal conductivity [39]. The stator consists of 24 concentrated winding tooth coils as shown in Fig. 4.4. Its inherent segmented structure allows winding of the coils prior to assembly into the stator [6]. This simplifies the foil winding process and allows to avoid open slots or a segmented stator which are required in the case of a radial flux machine [32, 40]. It also allows to eliminate the free space in a slot as found between two adjacent winding phases in foil wound radial flux machines [32].

4.3 Winding Loss Evaluation and Comparison

In this section, the influence of the use of anodized aluminum foil on the winding losses in comparison to copper wire will be discussed.

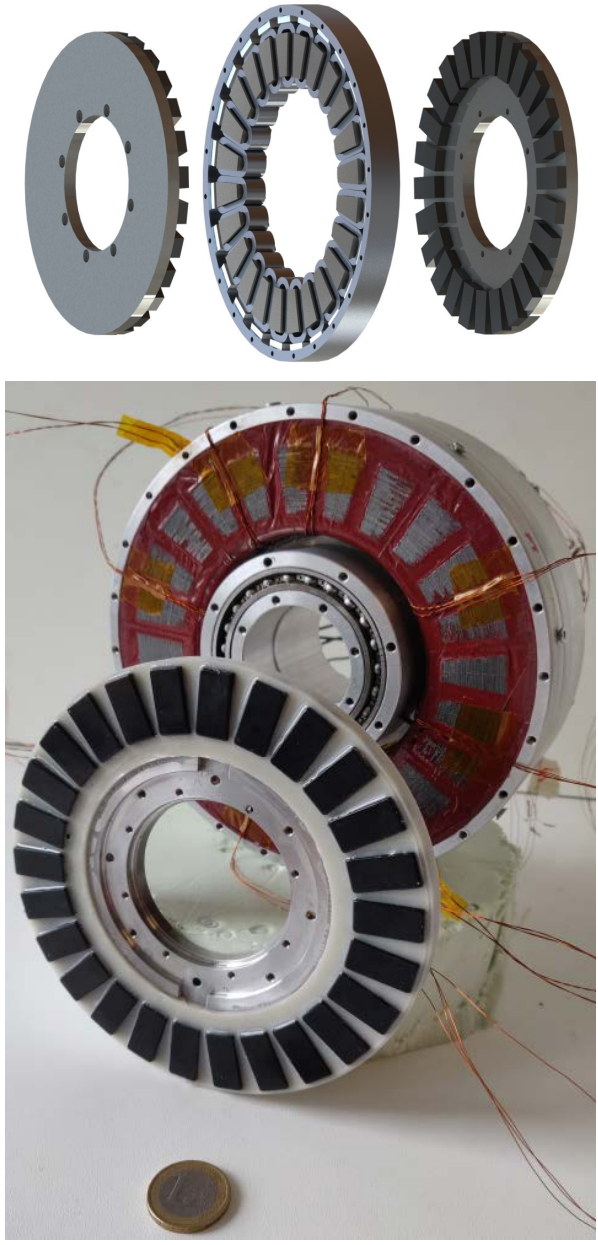

Figure 4.3: (a) CAD drawing of the test case YASA AFPMSM (b) Assembled prototype stator and rotor, both enamelled copper wire and anodized aluminum foil stator look identical after epoxy impregnation

Figure 4.4: Prototype tooth coils. Left: enamelled copper wire tooth coil, Right: anodized aluminum foil tooth coil

DC Winding Resistance

To compare the DC winding losses for both conductor materials, the DC resistance is calculated using the law of Pouillet:

$$R_{\mathrm{DC}}(T) = \frac{\rho \cdot l \cdot (1 + \alpha \cdot (T - 20°\mathrm{C}))}{S} \tag{4.1}$$

Where R_{DC} is the DC winding resistance at temperature T, ρ is the electrical resistivity at 20°C, l is the total length of the winding and S is the conductor cross-section. Using geometrical data obtained from the prototype tooth coils shown in Fig. 4.4, the DC resistance is calculated. For the copper wire tooth coil $R_{\mathrm{DC,Cu}}(T = 25°C) = 95.7\ m\Omega$, and for the anodized aluminum foil tooth coil $R_{\mathrm{DC,Al}}(T = 25°C) = 101.9\ m\Omega$. This results in a theoretical ratio of copper wire coil DC resistance over anodized aluminum foil coil DC resistance of 0.94, whereas experimentally it was observed that this ratio is 0.99. This discrepancy can be explained by the fact that there can be some deviation in the electrical resistivity from its nominal value. The allowed deviation is specified in standard IEC 60317-0-1 for enamelled copper wire. For the anodized aluminum foil, no standards exists yet that specifies the allowed deviation on the electrical resistivity and the tolerances on the dimensions, therefore the deviation between the estimated and real value is larger than for the copper wire.

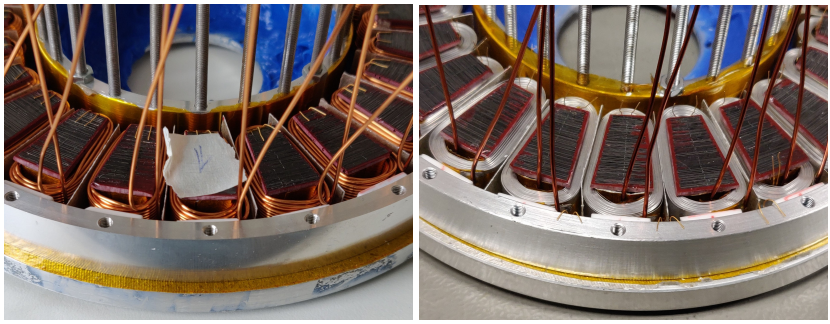

Figure 4.5: Enamelled copper wire (a) and anodized aluminum foil (b) stator prototypes prior to epoxy impregnation

Note that although, the electric resistivity of aluminum is 59% larger compared to copper, the winding DC resistance of the anodized aluminum foil tooth coil is only 1% larger. This is mainly the consequence of the large difference in conductor cross-section. It is possible to use a larger cross-section for the foil coil because the foil winding configuration allows a more efficient utilization of the available slot space. This can also be seen when comparing the fill factors for both tooth coils in Table 4.3, the fill factor is defined here as the number of turns times the conductor cross-section divided by the available slot space. In the test case machine the available slot space is 10 x 3.58 mm^2. Note that the anodized aluminum foil tooth coil weighs 18% less than its copper equivalent.

AC Winding Resistance

Several authors have studied AC winding losses in copper foil wound rotating electrical machines [41, 42]. They have concluded that AC winding losses can be an important part of the total winding losses especially in high-frequency machines. Therefore they recommended to use foil windings only in low frequency applications [42] and/or in case of short axial length in axial flux machines or short slot height in radial flux machines [43]. In direct-drive robotic applications where the maximum motor speed is typically low (300 rpm) and short axial length, pancake shaped motors are frequently used, these recommendation are typically fulfilled. A prototype YASA AFPMSM with both anodized aluminum foil and enamelled copper wire as specified in Table 4.2 and 4.3 respectively is constructed as shown in Figures 4.3 and 4.5. The phase winding resistance of both prototypes was measured for various frequencies using an LCR-meter (Rhode and Schwarz HM 8118, accuracy: 0.3% of reading). For the resistance measurements the rotors were removed from the stator. Fig. 4.6 provides the ratio of phase resistance $R_{\mathrm{DC+AC}}$ over DC phase resis-

Table 4.3: Specifications of the prototype tooth coil

Enamelled copper wire (Grade I, IEC 60317-13)	**Symbol**	**Value**	**Unit**
Number of turns	n_{turns}	35	/
Nominal outer diameter	$d_{\text{Cu,o}}$	0.8425	mm
Conductor diameter	$d_{\text{Cu,i}}$	0.8	mm
Winding length (incl. terminals)	l_{Cu}	276	cm
measured DC resistance (@ 25°C)	$R_{\text{DC,Cu}}$	94.54±0.37[1]	mΩ
Height laminated iron core	h_{core}	20	mm
Weight of tooth coil	$m_{\text{Cu+SiFe}}$	31.3	g
Resistivity copper	ρ_{Cu}	$1.72 \cdot 10^{-8}$	Ωm
Resistance temperature coeff.	α_{Cu}	3.93×10^{-3}	K^{-1}
Fill factor	$f_{\text{Cu,coil}}$	49	%
Dielectrical strength (IEC 60317-0-1)	E_{max}	87	V_{RMS}/μm
Price/kg		16.64	EUR/kg
anodized aluminum foil			
Number of turns	n_{turns}	35	/
foil width	h_{Al}	10	mm
total foil thickness	$t_{\text{Al,tot}}$	86	$^{\text{A}}\mu$m
thickness Al_2O_3 layer	t_{AlOx}	4.6	$^{\text{A}}\mu$m
Foil length (excl. terminals)	l_{Cu}	250	cm
Cu terminal length (dia. 0.9 mm)	l_{term}	40	cm
measured DC resistance (@ 25°C)	$R_{\text{DC,Al}}$	95.83±0.6[1]	mΩ
Height laminated iron core	h_{core}	20	mm
Weight of tooth coil	$m_{\text{Al+SiFe}}$	25.8	g
Resistivity aluminum	ρ_{Al}	$2.74 \cdot 10^{-8}$	Ωm
Resistance temperature coeff.	α_{Al}	4.03×10^{-3}	K^{-1}
Fill factor	$f_{\text{Al,coil}}$	75	%
Dielectrical strength (ISO 2376)	E_{max}	26.5	V_{RMS}/μm
Price/kg		685[2]	EUR/kg

[1]mean and standard deviation over 24 tooth coils,
resistance measured using an LCR-meter (Rhode and Schwarz HM 8118)
with an accuracy of 0.3% on the measured value.
[2]Note that this is the cost for a small order quantity of 2 kg,
for larger order quantities the cost will be lower.

tance as a function of the electrical excitation frequency at 25°C. The circles indicate measured data points. For the maximum excitation frequency of the prototype YASA AFPMSM (65 Hz @ 300 rpm), the resistance increase for both the anodized aluminum foil and copper wire variant, remains below 0.5%. However, at higher frequencies, Fig. 4.6 confirms the findings of the authors in [41, 42] that foil windings suffer from higher AC losses. This is also illustrated clearly in Fig. 4.7, where the ratio $R_{\text{AC}}/R_{\text{DC}}$ versus frequency is plotted up to 2600 Hz. Above 600 Hz, the ratio was determined by extrapolating the low frequency measurements from Fig. 4.6 using a quadratic scaling law. This allows to determine the frequency where R_{AC} becomes larger than R_{DC}. This is called the crossover frequency $f_{\text{crossover}}$. For the anodized aluminum foil winding, this is already at 1466 Hz, whereas for the enamelled copper wire winding this is only at 2492 Hz.

In contrast to the DC resistance, the AC resistance decreases for increasing temperatures. Equation 4.2 from [44] was used to calculate the ratio $R_{\text{DC+AC}}/R_{\text{DC}}$ for an average winding temperature of $T = 150°\text{C}$ using experimental data obtained at $T_0 = 25°\text{C}$:

$$(R_{\text{DC+AC}}/R_{\text{DC}})|_{\text{T}} = \frac{(R_{\text{DC+AC}}/R_{\text{DC}})|_{\text{T}_0} - 1}{(1 + \alpha(T - T_0))^{\frac{3}{2}}} + 1 \tag{4.2}$$

With α the temperature coefficient of resistivity for copper and aluminum respectively from Table 4.3. The resulting graphs are plotted in dashed lines in Fig. 4.6. The anodized aluminum foil coil still exhibits a higher AC resistance. However, the difference in AC resistance between the anodized aluminum foil coil and copper wire coil decreases at higher temperatures. Since the AC resistance at the maximum excitation frequency of the prototype motor at ambient temperature could be neglected, and it decreases with increasing temperature, the AC losses are neglected in the remainder of this work.

4.4 Thermal Performance Evaluation and Comparison

This section aims to study the influence of the use of anodized aluminum foil on the stator thermal performance in comparison to enamelled copper wire. The thermal performance of anodized aluminum foil and enamelled copper wire will be compared through both thermal measurements on a tooth coil, stator and a rotating motor, and through 3D thermal FE simulations. The parameters of the 3D thermal FE model will be determined experimentally through a similar procedure as described in [45]. The 3D thermal FE model is then used to study the influence of the winding-housing thermal interface and cooling on

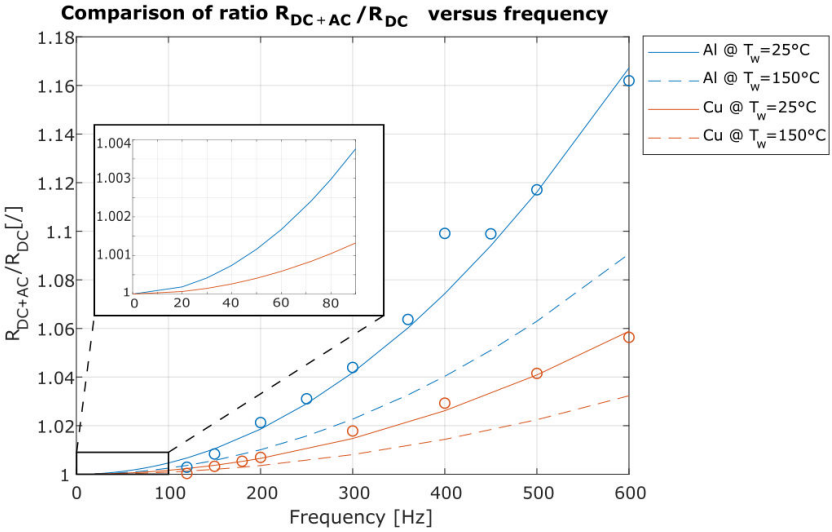

Figure 4.6: Comparison of the R_{DC+AC}/R_{DC} ratio between the anodized aluminum foil and copper wire prototype YASA AFPMSM as a function of the electrical excitation frequency, both for 25°C (measured data points are indicated with circles) and 150°C (trendline calculated according to [44])

the thermal performance for both conductor materials

4.4.1 Identification and Comparison of Equivalent Thermal Conductivities

A winding body is an amalgam of different materials: conductor, insulation and impregnation material. However, it is difficult to represent all these materials individually in a thermal FE model [39]. Several authors have overcome this issue through homogenization of the winding body in which a winding body is considered as a homogeneous material with an equivalent thermal conductivity tensor depending on the conductivities of the constituting materials [6, 39]. In this paragraph, the unknown equivalent thermal conductivity parameters for a 3D thermal FE model are determined by fitting the thermal FE model steady-state temperature predictions to temperatures measured on a dedicated identification tooth coil setup.

The anodized aluminum foil winding body consists of stacked layers of aluminum, aluminum oxide and epoxy impregnation. Since the thermal conductivity of aluminum is much larger, the equivalent thermal conductivity in the plane of the foil will be much larger than perpendicular to this plane. To

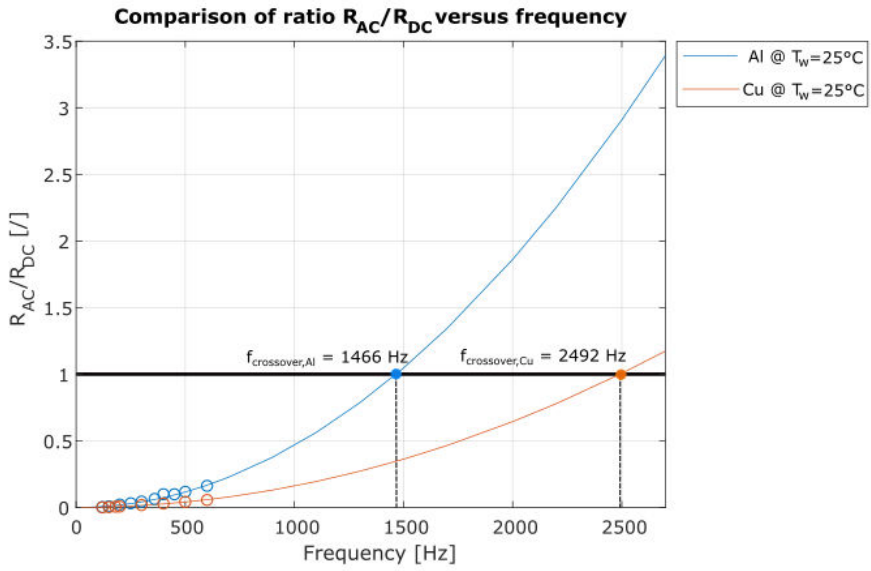

Figure 4.7: Comparison of the $R_{\mathrm{AC}}/R_{\mathrm{DC}}$ ratio between the anodized aluminum foil and copper wire prototype YASA AFPMSM as a function of the electrical excitation frequency (measured data points are indicated with circles), the frequency where R_{AC} becomes larger than R_{DC} is denoted by $f_{\mathrm{crossover}}$

include this phenomenon, one equivalent thermal conductivity for the good thermally conducting direction (in the plane of the foil) and one for the poor thermally conducting direction (perpendicular to the foil) are defined. Instead of directly fitting the equivalent thermal conductivities, they are first expressed in terms of the volume fractions (or fill factor) and thermal conductivities of the constituting materials. A grid search over these parameters is then performed to identify the parameters that result in the best fit between measurements and FE model predictions. For the good thermally conducting direction, the equivalent thermal conductivity can be calculated using the parallel material model from [39]:

$$k_{1,\mathrm{wi}}^{\mathrm{Al}} = f_{\mathrm{wi}}^{\mathrm{Al}} \cdot k_{1,\mathrm{anofol}} + (1 - f_{\mathrm{wi}}^{\mathrm{Al}}) \cdot k_{\mathrm{Ep}} \tag{4.3}$$

Where $f_{\mathrm{wi}}^{\mathrm{Al}}$ is the fill factor of the impregnated winding body, $k_{1,\mathrm{anofol}}$, the equivalent thermal conductivity of the anodized foil in the plane of the foil and k_{Ep}, the thermal conductivity of the epoxy resin. For the thermally poor conducting direction, the equivalent thermal conductivity can be calculated using the series material model from [39]:

$$k_{2,\mathrm{wi}}^{\mathrm{Al}} = \frac{k_{2,\mathrm{anofol}} \cdot k_{\mathrm{Ep}}}{(1 - f_{\mathrm{wi}}^{\mathrm{Al}}) \cdot k_{2,\mathrm{anofol}} + f_{\mathrm{wi}}^{\mathrm{Al}} \cdot k_{\mathrm{Ep}}} \tag{4.4}$$

Where $k_{2,\text{anofol}}$ is the equivalent thermal conductivity of the anodized foil perpendicular to the plane of the foil. $k_{1,\text{anofol}}$ and $k_{2,\text{anofol}}$ are also determined using the parallel and series material models respectively for the aluminum - aluminum-oxide amalgam:

$$k_{1,\text{anofol}} = f_{\text{anofol}} \cdot k_{\text{Al}} + (1 - f_{\text{anofol}}) \cdot k_{\text{AlOx}} \tag{4.5}$$

$$k_{2,\text{anofol}} = \frac{k_{\text{Al}} \cdot k_{\text{AlOx}}}{(1 - f_{\text{anofol}}) \cdot k_{\text{Al}} + f_{\text{anofol}} \cdot k_{\text{AlOx}}} \tag{4.6}$$

With k_{Al} and k_{AlOx}, the thermal conductivity of aluminum and aluminum-oxide respectively. The fill factor for this combination is defined as:

$$f_{\text{anofol}} = \frac{t_{\text{Al,tot}} - 2 \cdot t_{\text{AlOx}}}{t_{\text{Al,tot}}} \tag{4.7}$$

For the epoxy impregnated, enamelled copper wire winding body, the equivalent thermal conductivities are calculated through the use of the Hashin and Shriktman approximation [39]:

$$k_{1,\text{wi}}^{\text{Cu}} = f_{\text{wi}}^{\text{Cu}} \cdot k_{\text{Cu}} + (1 - f_{\text{wi}}^{\text{Cu}}) \cdot k_{\text{Ep}} \tag{4.8}$$

$$k_{2,\text{wi}}^{\text{Cu}} = k_{\text{Ep}} \cdot \frac{(1 + f_{\text{wi}}^{\text{Cu}}) \cdot k_{\text{Cu}} + (1 - f_{\text{wi}}^{\text{Cu}}) \cdot k_{\text{Ep}}}{(1 - f_{\text{wi}}^{\text{Cu}}) \cdot k_{\text{Cu}} + (1 + f_{\text{wi}}^{\text{Cu}}) \cdot k_{\text{Ep}}} \tag{4.9}$$

With $f_{\text{wi}}^{\text{Cu}}$ the fill factor the the impregnated copper coil and k_{Cu}, the thermal conductivity of copper. It is assumed that the copper wire enamel has the same thermal conductivity as epoxy and therefore it is not considered separately and taken into account via the fill factor.

The fill factors $f_{\text{wi}}^{\text{Cu}}$ and $f_{\text{wi}}^{\text{Al}}$ and k_{Ep} will now be determined through experimental parameter identification. To this end, a dedicated identification tooth coil was constructed and equipped with temperature sensors at critical locations. These locations were determined based on insights from [6]. Fig. 4.8 shows the stator teeth that are used for identification, the locations of the temperature sensors in the centre half plane are indicated with red dots. An equal and constant power is dissipated in both coils and the steady-state temperatures are recorded. It is assumed that the temperature are in steady-state when their time derivative drops below 0.5°C/10 min. To keep the dissipated power constant, the current has to be adjusted to compensate for the increase in DC resistance at higher temperatures. To obtain similar conditions as in the prototype YASA AFPMSM (Fig. 4.3) where the heat dissipation via the air gap is assumed to be negligible [6], all faces of the sample are insulated with thermal insulating wool except the aluminum housing '1', which is cooled by natural convection. Two aluminum-oxide pads are inserted between the housing

and the conductor material to guarantee sufficient electrical insulation without adding significant thermal resistance. Fig. 4.9 shows the modelled geometry

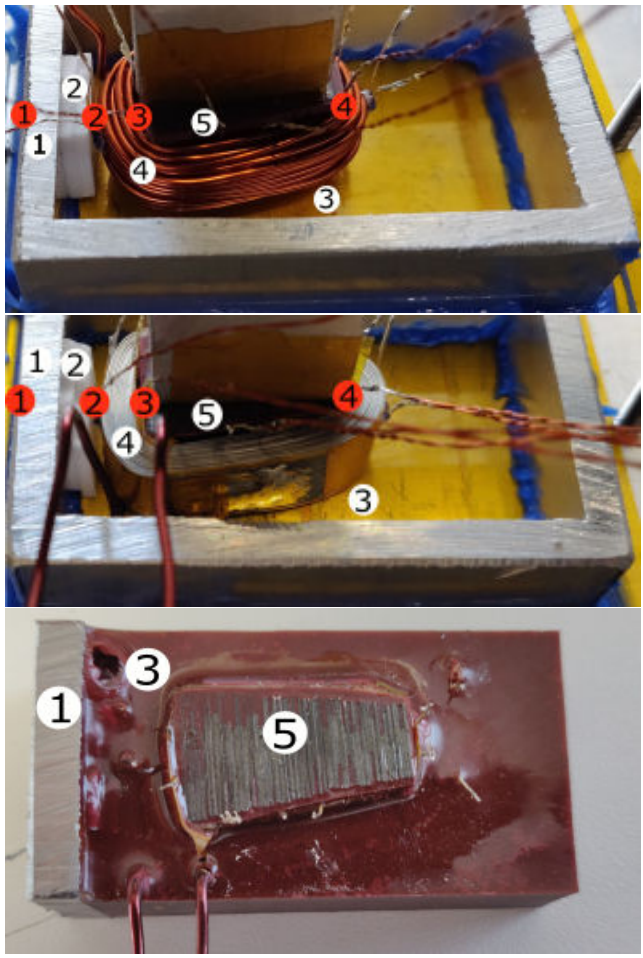

Figure 4.8: Mock-up stator tooth for identification of fill factor and thermal conductivity of epoxy (a & b prior to impregnation, c after impregnation): (1) aluminum housing (2) aluminum-oxide pads (3) Epoxy impregnation (4a) Enamelled copper wire (4b) anodized aluminum foil (5) Iron core; Red dots indicate PT100 temperature sensor locations

of the corresponding FE model. Due to thermal symmetry, it is sufficient to model only one quarter of a single tooth coil. It consists of 5 different domains with different thermal properties. It is assumed that all heat is evacuated from the motor via the outer radial surface of the aluminum housing via convection. In agreement with the tooth coil samples, thermal insulation is assumed for all other faces. The fill factor $f_{\mathrm{wi}}^{\mathrm{x}}$ ($\mathrm{x} = \{\mathrm{Al,Cu}\}$) and epoxy thermal conductivity

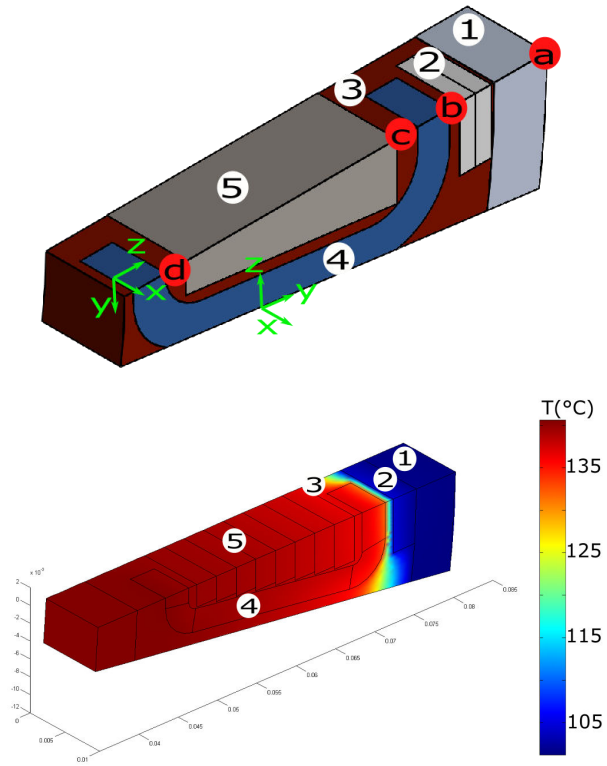

Figure 4.9: (a) 3D Thermal FEM quarter tooth coil model (b) Temperature distribution for 3.6 W losses in the aluminum winding: (1) aluminum housing (2) aluminum oxide thermal pad (3) Epoxy (4) anodized aluminum foil or enamelled copper wire (5) iron core; The red dots indicate the temperature sensor locations

k_{Ep} are identified through a grid search over all possible combinations to find the combination which minimizes the cost:

$$\min_{\forall f_{\mathrm{wi}}^{\mathrm{x}}, k_{\mathrm{Ep}}} \sum_{i=2}^{4} (T_{\mathrm{i}}^{\mathrm{FE}}(f_{\mathrm{wi}}, k_{\mathrm{Ep}}) - T_{\mathrm{i}}^{\mathrm{meas}})^2 \text{ for x=\{Al,Cu\}} \tag{4.10}$$

$T_{\mathrm{i}}^{\mathrm{FE}}$ and $T_{\mathrm{i}}^{\mathrm{meas}}$ are the predicted and measured temperatures at location i respectively. The locations are indicated on Fig. 4.8 . The results of the identification are given in Table 4.4. The equivalent thermal conductivities k_{x}, k_{y}, k_{z} are calculated using equations 5.11 through 5.7.

Table 4.4: Experimentally identified thermal parameters

Parameter	**Anodized aluminum**		**Enamelled copper**	
$f_{\mathrm{wi}}^{\mathrm{x}}$ [/]	0.9		0.33	
k_{Ep} [W/mK]	0.73		0.73	
k_{x} [W/mK]	$k_{1,\mathrm{wi}}^{\mathrm{Al}}$	212	$k_{2,\mathrm{wi}}^{\mathrm{Cu}}$	1.37
k_{y} [W/mK]	$k_{1,\mathrm{wi}}^{\mathrm{Al}}$	212	$k_{1,\mathrm{wi}}^{\mathrm{Cu}}$	124
k_{z} [W/mK]	$k_{2,\mathrm{wi}}^{\mathrm{Al}}$	7.1	$k_{2,\mathrm{wi}}^{\mathrm{Cu}}$	1.37

The equivalent thermal conductivity for the thermally poor conducting direction, k_{z}, of the anodized aluminum foil is 3.6 times larger than for the copper coil. Moreover k_{z} of the anodized aluminum foil winding is in good agreement with the values reported for an anodized aluminum wire amalgam in [16, 24, 39], confirming the validity of the modelling and estimation procedure. Note that a temperature sensor at location '1' is an absolute requirement for the unique identification of the parameters, however this is only possible in a mock-up setup because the temperature sensor creates an epoxy-filled gap between the winding and the aluminum-oxide pads which significantly increases the thermal resistance as will be shown in the following paragraph.

Note the discrepancy between the fill factors in Table 4.4 and Table 4.3. Table 5.4 gives thermal conductivity values and fill factors that better match the fill factors in Table 4.4. This is because the identification based on fitting measurements to FE model predictions is a non-linear problem and multiple solution candidates exist. New insights and a more accurate grid search has resulted in the improved solution of Table 5.4. An uncertainty analysis would require Monte Carlo simulations which is beyond the scope of this work.

4.4.2 Stator Thermal Performance and Influence of Winding-Housing Thermal Interface

The influence of the conductor material on the stator performance is analysed in this section using the identified parameters from Section 4.4.1 in a 3D thermal FE model. The FE model from Section 4.4.1 is adapted by removing the gap between the winding body and the aluminum-oxide pads created by the temperature sensor. However, a small void or gap remains because of the irregularity of the winding body top surface. Due to the low viscosity of the used epoxy, this gap is also filled with epoxy during impregnation. Despite the irregular and complex geometry of this gap, it is represented by an equivalent thin layer with uniform thickness $t_{\mathrm{gap,equi}}$ in the 3D thermal FE model. However, this equivalent gap thickness is difficult to determine a priori and strongly depends on the material and manufacturing tolerances. Therefore influence of

the conductor material on the stator thermal performance is analysed as a function of the equivalent fill factor of the space between the winding body and the housing $f_{\text{interface}}$, which is defined by:

$$f_{\text{interface}} = \frac{t_{\text{AlOx-pads}}}{t_{\text{AlOx-pads}} + t_{\text{gap,equi}}} \tag{4.11}$$

With $t_{\text{AlOx-pads}}$, the thickness of the aluminum-oxide thermal pads between the winding body and housing. The stator thermal performance will be expressed in terms of the thermal resistance between the hotspot and the outer surface of the housing:

$$R_{\text{hotspot}} = \frac{T_{\text{hotspot}} - T_{\text{housing}}}{P_{\text{dissipated losses}}} \tag{4.12}$$

With $P_{\text{dissipated losses}}$, the losses in a single tooth coil of the stator. The hotspot location coincides with the location of temperature sensor 'd' [6]. The hotspot temperature is of interest because the losses (and thus the torque) for which this temperature corresponds to the material temperature limit, determines the torque density. The thermal FE model with parameters from Table 4.4 is used to calculate R_{hotspot} for both the anodized aluminum foil and copper wire winding stators as a function of $f_{\text{interface}}$. The results are given in Fig. 4.10. Over the complete range of $f_{\text{interface}}$ the thermal resistance of the anodized aluminum foil winding stator is lower compared to the copper wire winding stator, this could be expected from the results in Section 4.4.1, however it should be noted that the relative difference in thermal resistance increases for increasing $f_{\text{interface}}$. The temperature difference $[T_{\text{Cu-wire}} - T_{\text{Al-foil}}]_{\forall(\text{x,y,z})}$ is plotted for two extreme cases $f_{\text{interface}} = 1$ and $f_{\text{interface}} = 0.5$. For the ideal case of $f_{\text{interface}} = 1$, the thermal resistance of the aluminum stator is 39% lower compared to its copper counterpart, whereas for $f_{\text{interface}} = 0.5$, representing a very poor thermally conducting interface between winding body and housing, it is only 4% lower.

The true thermal resistance between the hotspot and the housing was measured for both conductor materials, both in a single stator tooth and a full stator prototype as shown in Fig. 4.11. Fig. 4.11a and b show the tooth coils prior to epoxy impregnation. After epoxy impregnation the samples look identical to Fig. 4.8c. The small gap between winding body and thermal pads is indicated with a red circle. During the measurements all surfaces are thermally insulated with 2 cm thermal insulating wool except the aluminum housing surface '1' which is cooled by natural convection. Fig. 4.11c shows the stator prototype after epoxy impregnation. Both copper and aluminum winding prototypes look identical after impregnation. The top and bottom surface are insulated with XPS insulation, however for clarity the top insulating cover is not shown on Fig. 4.11c. The stator prototypes are cooled via a water cooled cold plate.

The motor aluminum housing '1' is thermally connected via silicone thermal pads '9', an aluminum interconnection shell '10', and silicone thermal paste '11' to the aluminum cold plate '8'. The thermal resistance was determined by dissipating a constant and equal power in both winding bodies and recording the steady-state hotspot 'd' and housing temperature 'a'. It was assumed that the temperatures are in steady-state when their time derivative drops below 0.5°/10 min. For the full stator prototype, the average over 8 different coils is used. To keep the dissipated power constant, the current has to be adjusted to compensate for the increase in DC resistance at higher temperatures. The results are indicated on Fig. 4.10. This allows to estimate the $f_{\text{interface}}$ for the tooth coil and stator prototypes from Fig. 4.11. In all cases, the estimated fill factor $f_{\text{interface}} < 1$, thus confirming the presence of epoxy between the winding body and the aluminum-oxide thermal pads. The reduction in thermal resistance compared to a winding body with enamelled copper wire is 14% for the tooth coil prototypes and 1% in favour of copper for the full stator prototypes. The latter is caused by a lower $f_{\text{interface}}$ for the aluminum winding stator case due to tolerances in the manufacturing process of the prototype. These results allows us to conclude that the use of anodized aluminum foil can only result in a significantly lower thermal resistance between hotspot and housing in case the winding body represents a significant fraction of this thermal resistance.

4.5 Torque Density Comparison

In previous sections, the losses and thermal properties have been studied since both aspects affect the torque density of an electrical machine. In this section, the torque density of the anodized aluminum foil and copper wire test case YASA AFPMSM are determined experimentally on a rotating setup. Additionally, experimental loss data and the 3D thermal FE model from section 4.4 are used to study the influence of the cooling performance on the torque density.

4.5.1 Prototype YASA AFPMSM Scenario

The prototype YASA AFPMSMs are compared experimentally on a rotating test bench both under same hotspot temperature conditions (i.e. the hotspot in both motors is identical) and under same current conditions (i.e. the phase current in both motors is identical). One set of bearings and rotor discs was used for both motors to eliminate as many error sources as possible. Fig. 4.12 shows the testbench that was used to determine the torque density. The prototype YASA AFPMSM as shown in Fig. 4.3 is connected via a torque

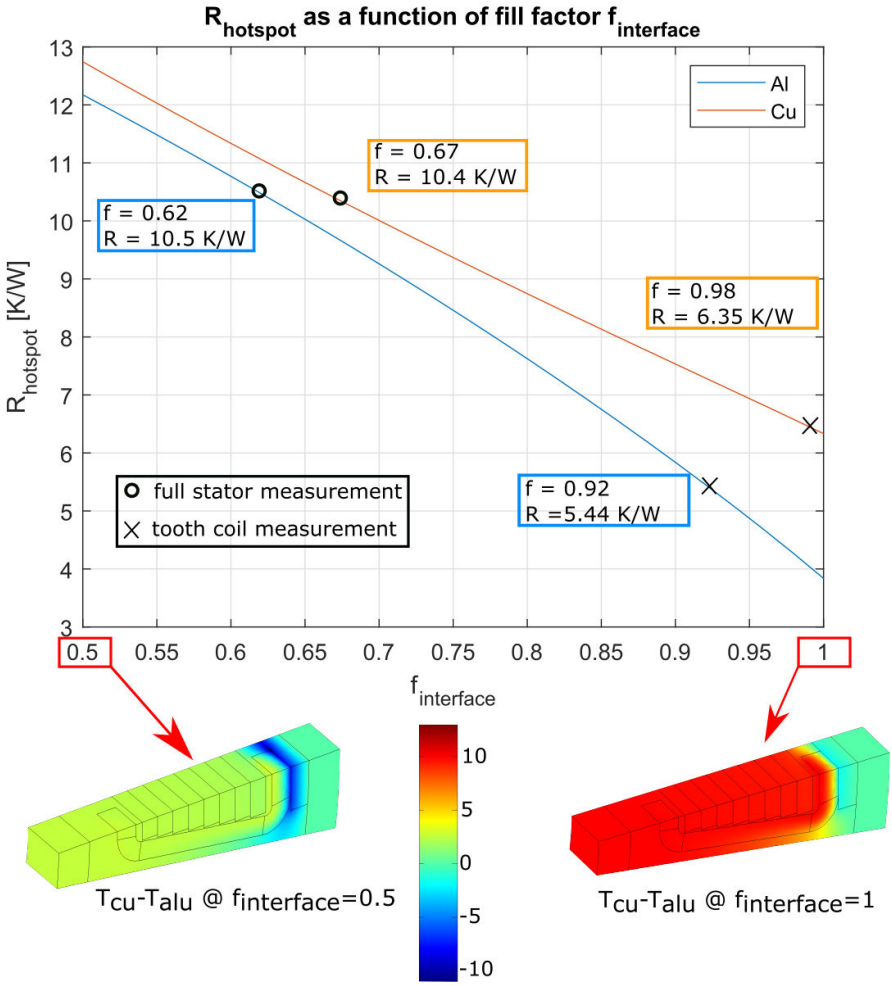

Figure 4.10: (Top) Thermal resistance between hotspot and housing as a function of the fill factor $f_{\text{interface}}$ of the thermal interface between winding and housing for both anodized aluminum foil and copper wire winding stators, 'circles' indicate measurements on a full stator (standard deviation 0.3 K/W) and 'x' indicates measurements on a tooth coil (bottom) $[T_{\text{Cu-wire}} - T_{\text{Al-foil}}]_{\forall(x,y,z)}$ for $f_{\text{interface}} = 0.5$ (left) and $f_{\text{interface}} = 1$ (right)

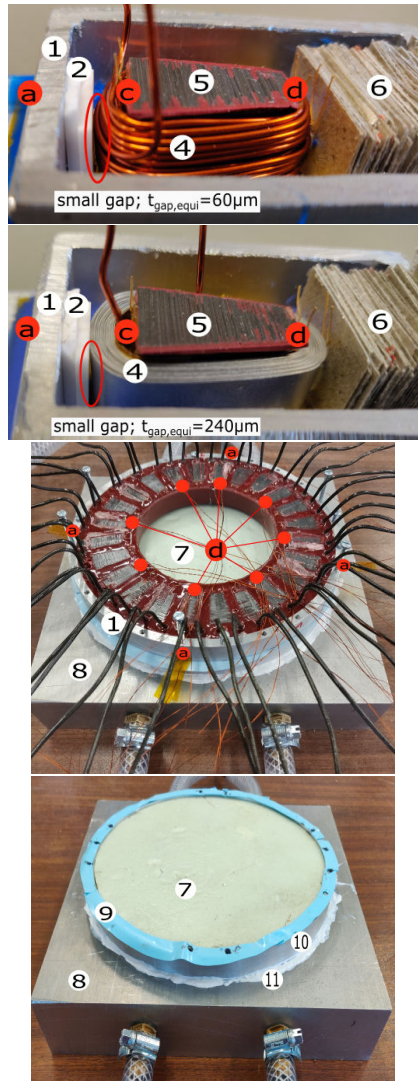

Figure 4.11: (a and b) stator tooth coil prototype prior to epoxy impregnation (c) full stator prototype on cold plate: aluminum and copper variant look identical after impregnation (d) thermal interface between stator prototype and cold plate. (1) aluminum housing (2) aluminum-oxide pads (4a) Enamelled copper wire (4b) anodized aluminum foil (5) Iron core (6) Mica paper stack, to press winding body against thermal pads (7) XPS insulation (8) Cold plate (9) Silicone thermal pad (10) aluminum interconnection shell (11) Silicone thermal paste. Red dots indicate PT100 temperature sensor locations

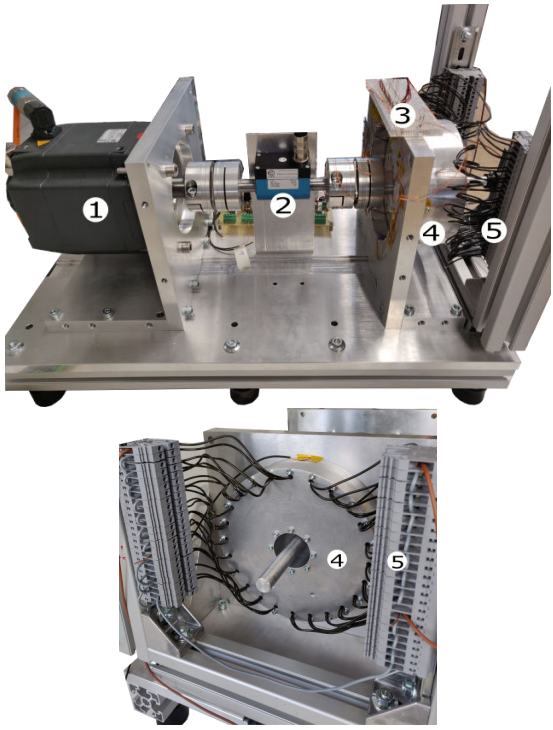

Figure 4.12: Prototype testbench: (1) Load motor (2) Torque sensor (Lorenz DR-2112, ±50 Nm) (3) PT100 terminal board (4) prototype YASA AFPMSM, both aluminum and copper variant look identical (5) motor terminal interconnection rail

sensor (Lorenz DR-2112, ±50 Nm, accuracy: 0.1 Nm) to a load motor. A magnetic absolute encoder (RLS AksIM-2) was used to measure the position. The YASA AFPMSM is supplied from a custom three-phase two-level voltage source inverter ($V_{\mathrm{DC}} = 48V$) and uses Allegro ACS730KLCTR-40AB-T phase current sensors, a dSPACE MicroLabBox was used to implement standard field oriented PI current controllers. The same temperature sensors as indicated on Fig. 4.11c are used to measure the hotspot temperature. The YASA AFPMSM housing is thermally insulated from its mounting flange via 0.4 mm mica sheet and cooled via natural convection over its radial and axial housing surface. The results are given in Table 4.5 and 4.6. Note that since the same measurement equipment was used for both the motors, the deterministic measurement error is the same for both and has no influence on the conclusions when relatively comparing the results. The stochastic measurement error was eliminated by averaging over sufficiently measurements. In the 'same hotspot temperature'-scenario, the anodized aluminum foil wound

prototype shows a 13% increase with respect to the copper winding variant in terms of torque per kg active stator mass. However, in terms of the other metrics, the copper winding variant shows a better performance. This is explained by the fact that the copper wire winding prototype exhibits a higher torque constant and a slightly lower thermal resistance (see Fig. 4.10). The difference in thermal resistance was already explained in Section 4.4.2. The difference in torque constant is the consequence of small differences between the two prototypes in the radial positions of the stator teeth. This was caused by the manual manufacturing process. In the 'same phase current'-scenario, it can be seen in Table 4.6 that the winding losses in the aluminum foil motor are slightly higher, due to its slightly larger DC resistance. Also the hotspot temperature is larger due to the larger losses and the larger thermal resistance. Despite its lower torque constant and slightly higher thermal resistance, the anodized aluminum foil winding prototype YASA AFPMSM still demonstrates a higher torque per kg of active stator mass on the testbench. This affirms the potential of anodized aluminum foil wound YASA AFPMSMs to obtain a higher torque density compared to enamelled copper wire variants.

The measured efficiency of both motors is also given in Table 4.5 and 4.6. The efficiency is quite low because of the low operating speed. Note however that it was not the aim of this study to optimize efficiency.

In Fig. 4.13, the measured transient thermal response of the housing and hotspot temperatures for a step change in the winding losses are given for both the anodized aluminum foil and copper wire winding prototype motors operating at 300 rpm. It should be noted that no significant difference in transient behaviour could be observed on this time scale because the thermal time constant is mainly determined by the housing and mounting frame. Additionally, the estimated transient thermal responses are shown in Fig. 4.13. The 3D thermal FE model from Section 4.4.2 was adapted and used to calculate the responses. A convective boundary condition was used for the airgap surface and the mounting frame was included into the model. The unknown parameters were identified through a grid search to find the parameters for which the estimated temperature rise best fitted the measured temperature rise. The maximum difference between the estimated and measured temperature rise is smaller than 1 °C, this again confirms the validity of the modelling approach followed in Section 4.4.

4.5.2 Improved Winding Body Thermal Interface Scenario and Influence of Cooling Performance

In this section, the torque density is determined for the ideal case $f_{\text{interface}} = 1$ described in Section 4.4.2 in function of the cooling performance. To this end, the thermal FE model from Section 4.4.2 is used with the losses determined

Table 4.5: Comparison of prototype YASA AFPMSM @ [Ω_m =300 rpm, $T_{\text{hotspot}} = 61.35°C$, $T_{\text{ambient}} = 25°C$]

	Anodized aluminum foil	**Enamelled Cu wire**	**Al/Cu**
Phase current [A_{RMS}]	3.47	3.62	0.96
T_{hotspot} [$°C$]	61.4	61.4	1
Torque [Nm]	2.88	3.09	0.93
Torque constant [Nm/A]	0.83	0.85	0.97
Efficiency (%)	69	71	0.97
Torque density			
Nm/kg active stator mass[1]	4.65	4.11	1.13
Nm/kg active mass[2]	1.24	1.25	0.99
Nm/kg active+non-active mass[3]	0.83	0.86	0.97
Torque density			
Nm/litre active stator volume	10.6	11.35	0.93
Nm/litre active volume	4.77	5.12	0.93
Power and Losses			
P_{DC}, DC input power [W]	128	136	0.94
P_m, mechanical power [W]	90.6	97.0	0.93
$P_{\text{no-load}}$ no-load losses [W][4]	4.60	4.56	1.01
P_{PE}, inverter losses[W][5]	1.86	2.01	0.93
P_{w}, winding losses [W][6]	30.6	32.5	0.94

[1]Stator active mass for Cu: 0.75 kg, Al: 0.62 kg
[2]Active mass for Cu: 2.46 kg, Al: 2.33 kg
[3]Total mass for Cu: 3.59 kg, Al: 3.46 kg
[4]Measured mechanical power when $I_{\text{phase}} = 0$; includes mechanical losses and iron losses
[5]Determined via transient calorimetric loss measurement method from [46]
[6]$P_w = P_{\text{DC}} - P_m - P_{\text{no-load}} - P_{\text{PE}}$

in Section 4.3. A convective boundary condition on the motor housing is assumed with convective heat transfer coefficient h_{housing} which is varied in order to examine the influence of the cooling performance. The results are given in Fig. 4.14. The anodized aluminum foil winding prototype has a higher torque per kg of active stator mass over the complete range of h_{housing}. The difference between the aluminum and copper winding variants increases for increasing cooling performance. This is in agreement with the findings from Section 4.4.2. The more dominant the winding body becomes in the thermal resistance between the hotspot and the ambient, the larger the difference in favour of the

Table 4.6: Comparison of prototype YASA AFPMSM @ [Ω_m =300 rpm, Phase current = 3.62 A_{RMS}, $T_{\text{ambient}} = 25°C$]

	Anodized aluminum foil	**Enamelled Cu wire**	**Al/Cu**
Phase current [A_{RMS}]	3.62	3.62	1
T_{hotspot} [$°C$]	63.5	61.4	1.03
Torque [Nm]	2.92	3.09	0.93
Torque constant [Nm/A]	0.81	0.85	0.95
Efficiency (%)	69	71	0.97
Torque density			
Nm/kg active stator mass[1]	4.71	4.11	1.15
Nm/kg active mass[2]	1.26	1.25	1.01
Nm/kg active+non-active mass[3]	0.84	0.86	0.98
Torque density			
Nm/litre active stator volume	10.74	11.35	0.95
Nm/litre active volume	4.84	5.12	0.94
Power and Losses			
P_{DC}, DC input power [W]	132.5	136	0.97
P_m, mechanical power [W]	92	97.0	0.95
$P_{\text{no-load}}$ no-load losses [W][4]	4.9	4.56	1.07
P_{PE}, inverter losses[W][5]	2.01	2.01	1
P_{w}, winding losses [W][6]	33.59	32.5	1.03

[1]Stator active mass for Cu: 0.75 kg, Al: 0.62 kg
[2]Active mass for Cu: 2.46 kg, Al: 2.33 kg
[3]Total mass for Cu: 3.59 kg, Al: 3.46 kg
[4]Measured mechanical power when $I_{\text{phase}} = 0$; includes mechanical losses and iron losses
[5]Determined via transient calorimetric loss measurement method from [46]
[6]$P_w = P_{\text{DC}} - P_m - P_{\text{no-load}} - P_{\text{PE}}$

aluminum winding body caused by its higher equivalent thermal conductivities. In case of a high performance cooling system ($h_{\text{housing}} = 600\text{W/m}^2\text{K}$), the anodized aluminum foil winding test case machine exhibits a 37% higher torque per kg active stator volume.

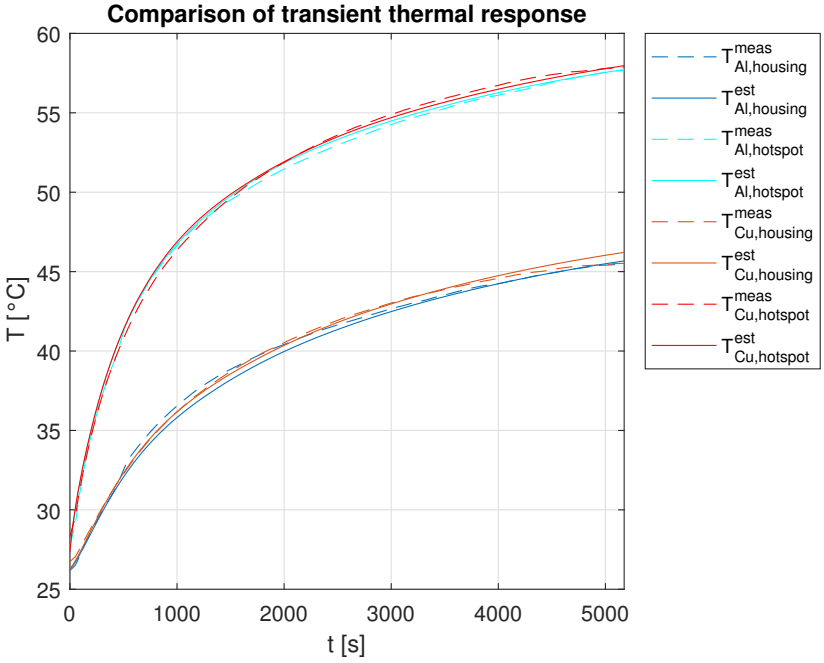

Figure 4.13: Comparison of the predicted and measured temperature rise of the housing and the hotspot (location 'd' in Fig. 4.11) for a step change in the winding losses from 0 W to 30.5 W. The winding losses are kept constant during the transient by adjusting the q-axis current. The operating speed is kept constant to Ω_m = 300 rpm

4.6 Conclusion

In this work, the use of anodized aluminum foil as an alternative to enamelled copper wire was considered to improve the torque density of a YASA AFPMSM for a direct-drive robotic application. Anodized aluminum foil allows a higher fill factor. This resulted in an almost equal DC resistance for a test case YASA AFPMSM. The higher thermal conductivity of the aluminum-oxide insulation and the foil topology result in higher equivalent thermal conductivities of the winding body. Both the higher fill factor and the better thermal properties contribute to a higher torque density. A 13% increase in torque per kg active stator mass was measured experimentally for a test case YASA AFPMSM. Relying on experimental data and a 3D thermal FE model, it was shown that anodized aluminum foil winding offers a higher torque density in low speed YASA axial flux motors where the winding body thermal resistance is dominant in the thermal path from heat source to heat sink.

To conclude, the potential of anodized aluminum foil YASA AFPMSM

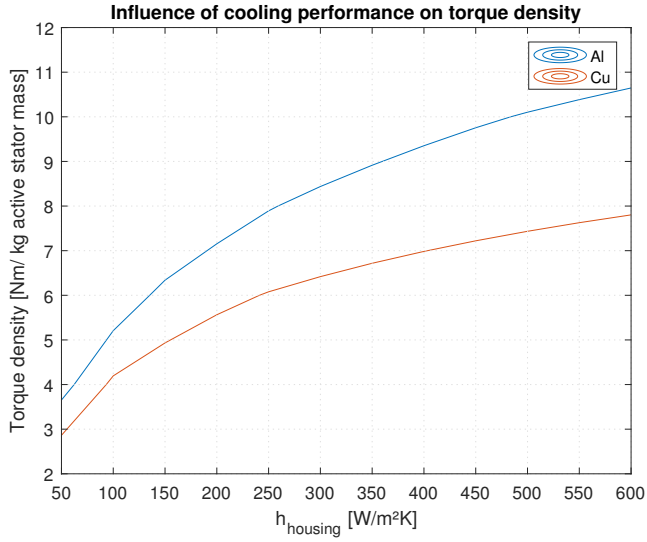

Figure 4.14: Torque per kg of active stator mass comparison as a function of the convective heat transfer coefficient of the motor housing surface h_{housing} @ [Ω_m = 300 rpm, $T_{\text{hotspot}} = 150°C$, $T_{\text{ambient}} = 50°C$]

to push the torque density limit of direct-drive robotic actuators was clearly illustrated in this work. Despite the improvement, the resulting torque density of the prototype motor is still far below the required 10 Nm/kg to realise useful tasks [1, 34]. Advanced cooling strategies and integration of electronics and motor can be considered to further push the torque density limit.

References

[1] J. Hollerbach, I. Hunter, J. Lang, S. Umans, R. Sepe, E. Vaaler, and I. Garabieta, "The mcgill/mit direct drive motor project." IEEE Comput. Soc. Press, pp. 611–617.

[2] G. Kenneally, A. De, and D. E. Koditschek, "Design principles for a family of direct-drive legged robots," *IEEE Robotics and Automation Letters*, vol. 1, pp. 900–907, 7 2016.

[3] P. M. Wensing, A. Wang, S. Seok, D. Otten, J. Lang, and S. Kim, "Proprioceptive actuator design in the mit cheetah: Impact mitigation and high-bandwidth physical interaction for dynamic legged robots," *IEEE Transactions on Robotics*, vol. 33, pp. 509–522, 6 2017.

[4] S. Yu, T. H. Huang, X. Yang, C. Jiao, J. Yang, Y. Chen, J. Yi, and

H. Su, "Quasi-direct drive actuation for a lightweight hip exoskeleton with high backdrivability and high bandwidth," *IEEE/ASME Transactions on Mechatronics*, vol. 25, pp. 1794–1802, 8 2020.

[5] B. Zhang, T. Seidler, R. Dierken, and M. Doppelbauer, "Development of a yokeless and segmented armature axial flux machine," *IEEE Transactions on Industrial Electronics*, pp. 1–1, 2015.

[6] H. Vansompel, P. Leijnen, and P. Sergeant, "Multiphysics analysis of a stator construction method in yokeless and segmented armature axial flux pm machines," *IEEE Transactions on Energy Conversion*, vol. 34, pp. 139–146, 2019.

[7] J. Klassen, S. Chamberlain, and H. K. Ka, "Electric machine comprising a safety ring," Patent, 2018.

[8] M. Waldhof, A. Echle, and N. Parspour, "A novel drive train concept for personalized upper body exoskeletons with a multiphase axial flux machine." IEEE, 5 2019, pp. 2160–2166.

[9] C. Wohlers, P. Juris, S. Kabelac, and B. Ponick, "Design and direct liquid cooling of tooth-coil windings," *Electrical Engineering*, vol. 100, pp. 2299–2308, 12 2018.

[10] J. D. Widmer, C. M. Spargo, G. J. Atkinson, and B. C. Mecrow, "Solar plane propulsion motors with precompressed aluminum stator windings," *IEEE Transactions on Energy Conversion*, vol. 29, pp. 681–688, 9 2014.

[11] C. R. Sullivan, "Aluminum windings and other strategies for high-frequency magnetics design in an era of high copper and energy costs." IEEE, 2 2007, pp. 78–84.

[12] G. Cakal and O. Keysan, "Flat winding made of aluminum or copper sheet for axial flux machines," *IET Electric Power Applications*, vol. 15, pp. 429–440, 4 2021.

[13] A. Acquaviva, M. Diana, B. Raghuraman, L. Petersson, and S. Nategh, "Sustainability aspects of electrical machines for e-mobility applications part ii: Aluminium hairpin vs. copper hairpin." IEEE, 10 2021, pp. 1–6.

[14] A. Selema, M. N. Ibrahim, and P. Sergeant, "Additively-manufactured ultra-light shaped-profile windings for hf electrical machines and weight-sensitive applications," *IEEE Transactions on Transportation Electrification*, pp. 1–1, 2022.

[15] P. Arumugam, E. Amankwah, A. Walker, and C. Gerada, "Design optimization of a short-term duty electrical machine for extreme environment," *IEEE Transactions on Industrial Electronics*, vol. 64, pp. 9784–9794, 12 2017.

[16] R. Wrobel, N. Simpson, P. H. Mellor, J. Goss, and D. A. Staton, "Design of a brushless pm starter generator for low-cost manufacture and a high-aspect-ratio mechanical space envelope," *IEEE Transactions on Industry Applications*, vol. 53, pp. 1038–1048, 3 2017.

[17] M. Groninger, F. Horch, A. Kock, M. Jakob, and B. Ponick, "Cast coils for electrical machines and their application in automotive and industrial drive systems." IEEE, 9 2014, pp. 1–7.

[18] M. Bach, A. Babl, and D. Gerling, "Integration of forming manufacturing technology into the component production of innovative electric motor concepts." IEEE, 12 2020, pp. 1–8.

[19] N. Simpson, D. J. North, S. M. Collins, and P. H. Mellor, "Additive manufacturing of shaped profile windings for minimal ac loss in electrical machines," *IEEE Transactions on Industry Applications*, vol. 56, pp. 2510–2519, 5 2020.

[20] F. Wu, A. EL-Refaie, and A. Al-Qarni, "Additively manufactured hollow conductors integrated with heat pipes: Design tradeoffs and hardware demonstration," *IEEE Transactions on Industry Applications*, vol. 57, pp. 3632–3642, 7 2021.

[21] P. Melendez-Vega and G. Venkataramanan, "Aluminum foil coils for human scale wind turbines." IEEE, 10 2012, pp. 1–5.

[22] R. Wrobel and P. Mellor, "Design considerations of a direct drive brushless machine with concentrated windings," *IEEE Transactions on Energy Conversion*, vol. 23, pp. 1–8, 3 2008.

[23] M. Galea, T. Hamiti, and C. Gerada, "Torque density improvements for high performance machines." IEEE, 5 2013, pp. 1066–1073.

[24] S. Ayat, H. Liu, M. Kulan, and R. Wrobel, "Estimation of equivalent thermal conductivity for electrical windings with high conductor fill factor." IEEE, 9 2018, pp. 6529–6536.

[25] Applications of anodised aluminium foil. Available at https://anofol.de/anwendungen (accessed: 16-05-2021).

[26] H. Jordan, "Anodized aluminum foil coil with 538° c capabilities. final report," Historical Energy Database (United States), Tech. Rep., 11 1980.

[27] D. A. Hewitt, "Approaches to improving thermal performance of inductors with a view to improving power density," Ph.D. dissertation, 2015.

[28] A. Cai, L. P. Yang, J. P. Chen, T. G. Xi, S. G. Xin, and W. Wu, "Thermal conductivity of anodic alumina film at (220 to 480) k by laser flash technique," *Journal of Chemical and Engineering Data*, vol. 55, pp. 4840–4843, 11 2010.

[29] S. Babicz, S. A. A. Djennad, and G. Velu, "Preliminary study of using anodized aluminum strip for electrical motor windings." Institute of Electrical and Electronics Engineers Inc., 12 2014, pp. 176–179.

[30] L. Reissenweber, A. Stadler, J. v. Lindenfels, and J. Franke, "Improved thermal behavior of an electromagnetic linear actuator with different winding types and the influence on the complex impedance." IEEE, 12 2019, pp. 1–6.

[31] M. Rios, G. Venkataramanan, A. Muetze, and H. Eickhoff, "Thermal performance modeling of foil conductor concentrated windings in electric machines," *IEEE Transactions on Industry Applications*, vol. 54, pp. 4104–4113, 9 2018.

[32] M. Rios and G. Venkataramanan, "Design and construction of a foil winding permanent magnet machine." IEEE, 10 2020, pp. 2026–2033.

[33] F. Ostyn, B. Vanderborght, and G. Crevecoeur, "Design and control of a quasi-direct drive robotic gripper for collision tolerant picking at high speed," *IEEE Robotics and Automation Letters*, pp. 1–8, 2022.

[34] Igus rebel: Fully integrated single joint. Available at https://www.igus.eu/info/rebel-gearbox-system (accessed: 16-05-2021).

[35] A. Singh, N. Kashiri, and N. Tsagarakis, "Design of a quasi direct drive actuator for dynamic motions." MDPI, 11 2020, p. 8516.

[36] "Ilm frameless servo kits," TQ-Robodrive, Tech. Rep., 2020.

[37] A. Husain. The rise of the 48v robots. Available at https://www.powerelectronicsnews.com/the-rise-of-the-48v-robots/ (accessed: 16-06-2022).

[38] H. Vansompel, P. Sergeant, and L. Dupre, "Optimized design considering the mass influence of an axial flux permanent-magnet synchronous generator with concentrated pole windings," *IEEE Transactions on Magnetics*, vol. 46, pp. 4101–4107, 12 2010.

[39] N. Simpson, R. Wrobel, and P. H. Mellor, "Estimation of equivalent thermal parameters of impregnated electrical windings," *IEEE Transactions on Industry Applications*, vol. 49, pp. 2505–2515, 11 2013.

[40] P. Arumugam, T. Hamiti, and C. Gerada, "Fault tolerant winding design - a compromise between losses and fault tolerant capability," 2012, pp. 2559–2565.

[41] C. Gerada, "Estimation of eddy current loss in semi-closed slot vertical conductor permanent magnet synchronous machines considering eddy current reaction effect," *IEEE Transactions on Magnetics*, vol. 49, pp. 5326–5335, 2013.

[42] P. Arumugam, T. Hamiti, C. Brunson, and C. Gerada, "Analysis of vertical strip wound fault-tolerant permanent magnet synchronous machines," *IEEE Transactions on Industrial Electronics*, vol. 61, pp. 1158–1168, 3 2014.

[43] F. Franchini, E. Poskovic, L. Ferraris, A. Cavagnino, and G. Bramerdorfer, "Application of new magnetic materials for axial flux machine prototypes." IEEE, 5 2017, pp. 1–6.

[44] R. Wrobel, A. Mlot, and P. H. Mellor, "Contribution of end-winding proximity losses to temperature variation in electromagnetic devices," *IEEE Transactions on Industrial Electronics*, vol. 59, no. 2, pp. 848–857, 2012.

[45] H. Vansompel, A. Yarantseva, P. Sergeant, and G. Crevecoeur, "An inverse thermal modeling approach for thermal parameter and loss identification in an axial flux permanent magnet machine," *IEEE Transactions on Industrial Electronics*, vol. 66, no. 3, pp. 1727–1735, 2019.

[46] D. Neumayr, M. Guacci, D. Bortis, and J. W. Kolar, "New calorimetric power transistor soft-switching loss measurement based on accurate temperature rise monitoring," in *2017 29th International Symposium on Power Semiconductor Devices and IC's (ISPSD)*, 2017, pp. 447–450.

Chapter 5

Stall Torque Performance Analysis of a YASA Axial Flux Permanent Magnet Synchronous Machine

Now that we have evaluated the use of anodized aluminum foil in Chapter 4 and presented solutions to overcome its mechanical challenges in Chapter 3. In this chapter, the last challenge mentioned in Section 1.4 is addressed: the overheating due to the uneven loss distribution at standstill.

The actuators in novel service robot applications like exoskeletons, legged quadruped robots or humanoids have to be capable to deliver a high torque at almost standstill, this is also sometimes referred to as stall torque. This is not only the case in a gripper which has to hold a brittle object as explained already in Section 1.4 but also when a legged robot or humanoid is transporting a heavy and vulnerable payload in a post-disaster environment. This is typically characterized by narrow spaces, filled with unstable obstacles, where they cannot use their brakes to lock their joints while e.g. waiting for assistance, updating a path plan or clearing the road using other limbs.

During stall torque, the majority of the conduction losses are concentrated in a single phase of the motor. For the worst-case rotor position, when the motor generates its rated torque, two times the rated losses are generated in a single phase resulting in overheating of the motor. Although this is a known problem, its analysis received little attention so far. In this chapter, the influence of three key parameters on the stall torque performance is studied: the slot/pole combination, the end-winding thermal interconnection and the thermal conductivity of the winding. The focus is on these parameters as they directly influence heat transport in the tangential direction.

The influence of these parameters is studied experimentally by injecting a DC current in the stator. The stator winding is configured in such a way that the same loss distribution is obtained as if the stator was assembled in a motor producing stall torque. The thermal resistance between the hotspot in the stator and the housing is then determined by measuring the injected losses and the temperature difference. A stall torque derating factor, which is the ratio of the maximum torque at standstill over the maximum torque, is then calculated using the thermal resistance. This factor allows to assess the influence of the considered parameters on the stall torque performance.

Stall Torque Performance Analysis of a YASA Axial Flux Permanent Magnet Synchronous Machine

Adapted from: J. Van Damme, H. Vansompel, and G. Crevecoeur, "Stall Torque Performance Analysis of a YASA Axial Flux Permanent Magnet Synchronous Machine," *Machines*, vol. 11, no. 4, p. 487, 2023.

Abstract: There is a trend to go towards low gear-ratio or even direct-drive actuators in novel robotic applications in which high-torque density electric motors are required. The Yokeless and Segmented Armature Axial Flux Permanent Magnet Synchronous Machine is therefore considered in this work. In these applications, the motors should be capable to deliver high torque at standstill for long periods of time. This can cause overheating of the motors due to a concentration of the losses in a single phase; hence, it becomes necessary to derate the motor torque. In this work the influence of the slot/pole combination, the addition of a thermal end-winding interconnection and the equivalent thermal conductivity of the winding body on the torque performance at standstill will be studied both experimentally via temperature measurements on a prototype stator, and via a calibrated 3D thermal Finite Element model. It was found that both a good choice of the slot/pole combination and the addition of a thermal end-winding interconnection have a significant influence on the torque performance at standstill, and allow up to 8% increase in torque at standstill in comparison to a reference design.

5.1 Introduction

Owing to its high torque density and energy efficiency, Yokeless and Segmented Armature (YASA) Axial Flux Permanent Magnet Synchronous Machines (AFPMSM) have proven their benefits in several application areas such as transportation and wind energy generation [1, 2]. This axial flux motor topology consists of two rotors and a central stator, as illustrated in Figure 5.1. Motivated by the merits in these applications, more recently, this machine topology was also considered for use in quasi-direct-drive and direct-drive actuators of novel robotic applications [3, 4].

In some robotic applications however, the electric motor has to generate its maximum torque at (quasi-)standstill during a significant fraction of the load cycle. This is, e.g., the case in force-controlled robotic grippers [5] (See also Figure 5.1), or when a robot has to hold a vertical load against gravity for a long time [6]. This leads to a concentration of the losses in a single phase of the motor. For the worst-case commutation position, twice the rated conduction losses are dissipated in a single phase when the motor produces its rated torque at standstill. Although the sum of the conduction losses of all phases in this case does not exceed the rated conduction losses, due to the uneven loss distribution, this can eventually lead to overheating of the motor at standstill. This problem is well-known in academic and industrial literature [6, 7]. To avoid overheating, the stall torque, i.e. the maximum torque that a motor can produce under certain cooling conditions in steady-state at standstill, is typically lower than the rated torque.

Alternatively, brakes can be used to generate a stall torque and hold a load. There exist various kind of brakes [8], and most of them use an electromagnetic actuator such as a solenoid to engage or disengage friction discs. These friction discs provide the required holding torque without consuming energy. Hence, they can generate a higher stall torque. However, in certain applications, e.g., force-controlled robotic grippers where soft objects need to be grasped, the force of the gripper needs to be precisely controlled in order to avoid damage to the soft object [5]. Traditional grippers that use brakes cannot be used in this case since they rely on applying a sufficiently large torque to hold the object and then engage their holding brake. This would harm the soft object. To conclude, brakes can generate much higher stall torques; however, they are not usable in every application.

So far, no solutions have been presented yet to overcome the problem of overheating at standstill. Researchers have predominantly focussed on strategies that improve the overall thermal performance of YASA AFPMSMs through either an improved cooling (i.e., liquid instead of air cooling [9, 10]), through impregnating the windings [2] or through the introduction of radially inward heat extraction fins [1]. Although these strategies are very effective in increasing the total dissipated power losses, they are less effective in mitigating local overheating due to the uneven loss distribution caused by high torque at (quasi-)standstill. The problem of uneven temperature distribution due to partial immersion of the stator in an oil-cooled outer rotor radial flux machine was discussed in [11]. Oil storage slots were presented as an effective solution to reduce the local overheating. Although the presented solution appears to be very effective at rated speed, at (quasi-)standstill, the oil flows under the action of gravity to the bottom half of the motor, which drastically reduces its cooling effectiveness.

In this work, the problem of overheating during standstill due to the uneven

loss distribution will be analysed. Based on physical insights from previous studies on the thermal behaviour of YASA AFPMSMs [1, 2, 9], three key design parameters have been identified that potentially have a significant impact on the redistribution of the heat from the phase with the highest losses to the phases with lower losses. The influence of these three key design parameters on the stall torque performance is studied in this work (See Figure 5.1):

1. *Slot/pole combination:* This aspect influences both the fundamental winding factor and back-emf constant, which directly impact the torque. It also influences the number of adjacent slots belonging to the same phase. As heat has to flow from the phase with the highest losses to phases with lower losses, it can be expected that the number of adjacent slots influences the thermal performance under uneven loss distribution.

2. *Thermal end-winding interconnection:* From previous studies, it is known that the end-winding at the inner diameter is often the hottest area of a YASA AFPMSM [2, 10]; therefore, a good thermally conducting ring which interconnects all end-windings can redistribute the heat from the phase with the highest losses to the other phases.

3. *Equivalent winding body thermal conductivity:* Since in a YASA AFPMSM there is no iron stator yoke which has a good thermal connection with all slots, the equivalent thermal conductivity of the winding body can have a significant influence on the heat transfer between phases.

Note that also the axial flux machine topology can have an influence on the results, especially in the double stator, single rotor or single stator, single rotor topologies where the stator has an iron yoke providing a good thermal connection between the coils. However, this analysis falls beyond the scope of this work. The focus in this work is on the single stator, double rotor topology, which is known to have a higher torque density and energy efficiency [1, 2].

The analysis results in this work will lead to a better understanding of the stall torque performance and can be used in the design of motors for applications where high torque at (quasi)-standstill is important. Other applications might also benefit from the results. For example, in [12, 13], the problem of local overheating due to unbalanced supply voltage or inter-turn short circuits in induction motors was analysed. The studied key design parameters in this work can also improve the performance in these applications by redistributing the heat from the location with a higher loss concentration. However, this is beyond the scope of this article.

To study the influence of the aforementioned design parameters on the stall torque performance, a prototype YASA AFPMSM shown in Figure 5.2 is considered. Its main specifications are given in Table 5.1. The influence of the

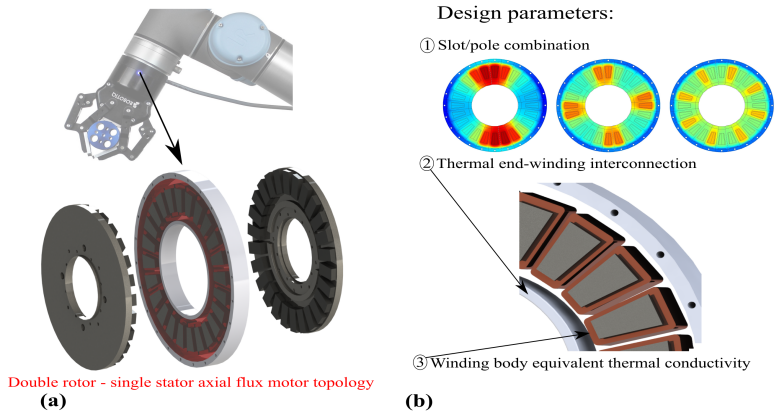

Figure 5.1: (**a**) The motor in a force controlled gripper has to generate high torque at (quasi)-standstill [14]. (**b**) Overview of the studied parameters in this work that potentially have a significant impact on the stall torque performance.

key design parameters will first be studied experimentally, the corresponding measurements will also be used to identify a 3D thermal Finite Element (FE) model. This model will allow to further analyse and improve the understanding of the experimental findings.

This paper is organised as follows: first, the three studied parameters are described in detail and illustrated for the prototype YASA AFPMSM in Section 5.2. Subsequently, the experimental setup is described in Section 5.3.1. The 3D thermal FE model is outlined in Section 5.3.2. Finally, the results of the experimental and simulation parameter study are presented in Section 5.4.

5.2 Design Parameters Affecting Tangential Heat Transfer

5.2.1 Loss Distribution

From previous work on thermal analysis of YASA AFPMSMs, it is known that there is no heat transfer between adjacent tooth coils under a uniform loss distribution and cooling [2]. However, when the motor produces torque at (quasi-)standstill, the phase currents are (quasi-)DC currents whose magnitude depends on the rotor position. Since the actual standstill rotor position is very application-specific and can vary with the operating scenario, the design should account for the worst-case standstill rotor position. This is the posi-

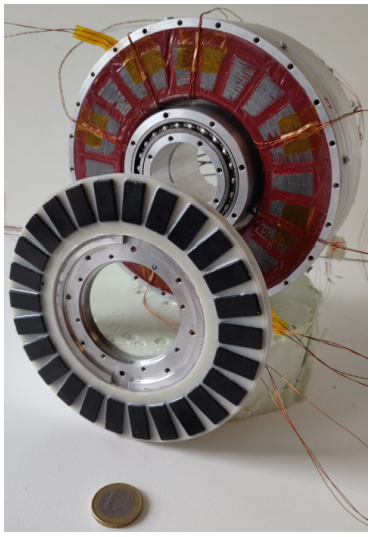

Figure 5.2: Prototype Yokeless and Segmented Armature Axial Flux Permanent Magnet Synchronous Machine used throughout this work; it has two rotors and a single stator. For visualization purposes only a single rotor is shown here. Its specifications are given in Table 5.1.

Table 5.1: Specifications of the test case YASA AFPMSM.

Parameter	**Symbol**	**Value**	**Unit**
Three-phase inverter DC bus voltage	V_{DC}	48	V
Maximum speed	Ω_{max}	300	rpm
Number of pole pairs	N_{p}	13	/
Number of slots	Q_{s}	24	/
Number of phases	n_{ph}	3	/
Number of turns per tooth coil	n_{turns}	35	/
Outer diameter stator iron core	D_{o}	138.5	mm
Inner diameter stator iron core	D_{i}	98.5	mm
Axial length stator iron core	h_{stat}	15	mm
Axial slot length	h_{slot}	10	mm
Total axial length (incl. housing)	l_{tot}	62.5	mm
Slot width	b_{slot}	6	mm
Airgap thickness	h_{air}	1.5	mm
Magnet height	h_{mag}	5	mm
Rotor yoke height	h_{mag}	6	mm

Table 5.2: Number of poles with $\xi > 0.866$ for a stator with 24 slots. (Note: no symmetric three phase winding is possible with 18 or 30 poles)

Q_s		Number of Poles (p)							
		16	**18**	**20**	**22**	**26**	**28**	**30**	**32**
24	ξ	0.866		0.933	0.9495	0.9495	0.933		0.866
	k'_ϕ	0.324		0.353	0.358	0.354	0.346		0.329
	$k'_\phi \cdot \xi$	0.281		0.329	0.340	0.336	0.323		0.285

tion where $I_\mathrm{u} = 2 \cdot I_\mathrm{v} = 2 \cdot I_\mathrm{w} = \sqrt{2} \cdot I_\mathrm{nom,RMS}$ [6]. With $I_\mathrm{u}, I_\mathrm{v}, I_\mathrm{w}$ the (quasi-)DC phase currents and $I_\mathrm{nom,RMS}$ the rated motor RMS current. Recall that for this worst-case position, the conduction losses in phase U equal twice the rated conduction losses and that the total conduction losses in the windings equal the rated conduction losses. Heat transfer between phases can be expected in this case, i.e., heat transfer in the tangential direction. This worst-case scenario will be considered throughout this work. Note that phase *U* was chosen arbitrarily as the phase with the highest losses in this work.

5.2.2 Slot/Pole Combination

The slot/pole combination influences the stall torque performance in different ways. The (stall) torque is given by [15]:

$$T = 3 \cdot \xi \cdot k'_\phi \cdot I, \tag{5.1}$$

with ξ, the fundamental winding factor, k'_ϕ, the back-emf constant and I the RMS phase current. A first way is via the fundamental winding factor. It is given by the product of the pitch factor ξ_p and distribution factor ξ_d. For a 3-phase, fractional slot concentrated two layer winding, the fundamental winding factor is given by:

$$\xi = \xi_\mathrm{p} \cdot \xi_\mathrm{d} = \sin\left(\frac{N_\mathrm{p}\pi}{Q_\mathrm{s}}\right) \cdot \frac{\sin\left(\frac{\pi}{6}\right)}{z \cdot \sin\left(\frac{\pi}{6 \cdot z}\right)} \tag{5.2}$$

where z is the numerator of q reduced to the lowest terms:

$$q = \frac{Q_s}{6 \cdot N_p} = \frac{z}{a}. \tag{5.3}$$

Table 5.2 gives the number of poles that result in a fundamental winding factor higher than 0.866 for a stator with 24 slots.

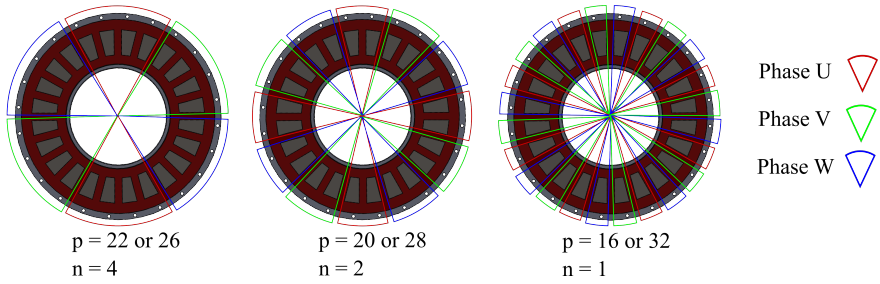

Figure 5.3: Winding diagrams and the number of adjacent coils belonging to the same phase n for the feasible slot/pole combinations from Table 5.2.

The second way is via the back-emf constant k'_ϕ:

$$k'_\phi = \frac{E_p}{\xi \cdot \Omega}, \tag{5.4}$$

with E_p the no-load back-emf (RMS value) of a phase at the mechanical speed Ω. The back-emf constant for different slot/combinations is determined using the analytical model for the flux density distribution in the iron core from [16, 17], the results can be found in Table 5.2. The prototype YASA AFPMSM has 24 slots, 26 poles and a fundamental winding factor equal to 0.9495. Although 22 and 26 poles result in the highest fundamental winding factor, other pole pair numbers will also be considered since these have a different winding diagram. The winding diagram indicates which coils belong to each phase. A different slot/pole combination results in a different winding diagram and thus a different number of adjacent coils belonging to the same phase. It can be expected that the distance between the centre of a phase with high losses and a phase with lower losses, respectively, will influence the tangential heat transfer. This is the third way via which the slot/pole combination influences the heat transfer in the tangential direction. Figure 5.3 gives the winding diagrams and the number of adjacent coils belonging to the same phase n for the feasible slot/pole combinations from Table 5.2.

5.2.3 Thermal End-Winding Interconnection

In Figure 5.4 the thermal end-winding interconnection ring (1) is shown. The concept is illustrated here for an epoxy potted YASA AFPMSM stator which is cooled via its housing at the outer diameter (3). The end-winding interconnection ring is therefore located at the inner diameter of the stator. In order to act as a highway for redistributing the heat between phases, it consists of a good thermally conducting material, e.g., aluminum or aluminum-oxide.

Figure 5.4: Yokeless and Segmented Armature Axial Flux Permanent Magnet Synchronous Machine: (1) Thermal end-winding interconnection ring (2) Concentrated winding tooth coil (3) Aluminum housing (4) Epoxy impregnation (5) Permanent magnet rotor.

In [18], a copper foam end-winding interconnection ring filled with phase change material was proposed for an outer-rotor radial flux machine to improve its peak load capabilities. Different from the proposed end-winding ring in this work, the ring in [18] interconnects the end-windings of the outer-rotor radial flux machine at the coldest axial face of the motor, i.e., the face where most heat leaves the motor. Therefore, the ring only acts as a thermal buffer during peak loads, but it is less effective in redistributing the heat between phases since it is located at the colder axial side of the motor. Although the concept of a thermal end-winding interconnection ring for redistributing the heat is illustrated in this work for a YASA AFPMSM, it is also applicable for radial flux machines.

At standstill no eddy-currents are induced in the end-winding ring; however, if the application both requires standstill and high speed operation, eddy current losses can occur in the end-winding ring if the electrical frequency is sufficiently high. The eddy current losses can be limited by choosing aluminum-oxide, or copper or aluminum foam instead of a solid aluminum ring. Therefore, this aspect will not be studied in further detail in this work.

5.2.4 Equivalent Winding Body Thermal Conductivity

A winding body consists of different materials with different thermal properties, this is often represented by equivalent thermal conductivities that depend on the thermal conductivities and volume fractions of the constituting materials [19]. Additionally, a winding body has anisotropic thermal properties due to its stranded or layered nature. Therefore, two different equivalent ther-

mal conductivities are defined: one for the direction along the conductor and one for the direction perpendicular to the conductor. Typically, the latter is the lowest one. In previous works, it was shown that the equivalent thermal conductivity perpendicular to the conductor can be much larger for a winding body consisting of anodized aluminum [4, 19]. Since the thermal conductivity of a winding body can have large influence on the thermal properties of the stator [2], it is expected that this can also have an influence on the tangential heat transfer. Therefore, the effect of the equivalent thermal conductivity of a winding body on the heat transfer in the tangential direction, and thus the stall torque performance, will be studied in this work. To this end, a YASA AFPMSM stator consisting of conventional concentrated winding tooth coils with round enamelled copper wire will be compared to a geometrically identical stator with anodized aluminum foil, which has superior equivalent thermal conductivities in both directions [4].

5.3 Materials and Methods

5.3.1 Experimental Setup

To study the influence of the slot/pole combination, the thermal end-winding interconnection and the winding body equivalent thermal conductivity on the heat transfer in the tangential direction and subsequently on the stall torque performance, the experimental setup shown in Figure 5.5 is used. It consists only of the stator of the prototype YASA AFPMSM motor from Figure 5.2. The rotor is not considered in this work since at standstill the rotor losses and convective heat transfer between stator and rotor is negligible [20]. Moreover, this allows to study different slot/pole combinations with a single stator. This avoids the need to manufacture multiple rotors and/or stators and eliminates the variability in the measurements caused by variability in the rotor/stator properties due to manufacturing imperfections.

Since it was assumed that the convective heat transfer between rotor and stator is negligible, both the top and bottom airgap surface of the stator are insulated with thermal insulation wool and XPS insulation (see (4) and (5) on Figure 5.5). All heat leaves the stator at the outer diameter via forced convection over the housing surface. The airflow is generated by two cooling fans (see (3) on Figure 5.5) located above the stator.

As already mentioned in Section 5.2.1, only the worst-case uneven loss distribution has to be considered. This is the position where $I_{\mathrm{u}} = 2 \cdot I_{\mathrm{v}} = 2 \cdot I_{\mathrm{w}} = \sqrt{2} \cdot I_{\mathrm{nom,RMS}}$ [6]. To emulate this worst-case situation, phase *U* is connected in series with a parallel connection of phases *V* and *W*, as shown in Figure 5.6. All coils belonging to the same phase are connected in series. A programmable DC power supply is used to inject a constant current

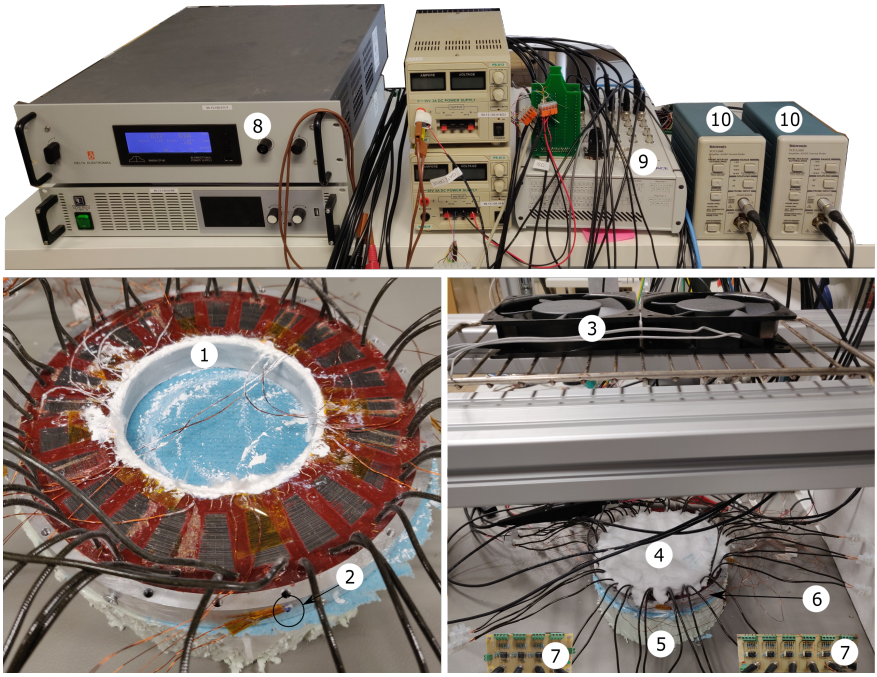

Figure 5.5: Experimental test setup. (left) Detailed view of prototype stator (1) thermal end-winding interconnection (2) PT100 temperature sensor on aluminum housing (right) Overview of setup: (3) cooling fans (4) thermal insulation wool (5) Expanded Polystyrene Insulation (XPS) (6) prototype stator between insulation (7) PT100 temperature sensor signal conditioning board (8) DC power supply (9) dSPACE MicroLabBox® real time control and data processing unit (10) Tektronix® TCPA 300 current amplifier.

in phase U. This way, the same loss distribution is obtained, as if the motor would produce a certain torque at standstill.

To study the influence of the equivalent winding body thermal conductivity, two geometrically identical stators were constructed: one with enamelled round copper wire as conductor and one with anodized aluminum foil as conductor. Figure 5.7 shows a single tooth coil for both conductor types and Table 5.3 provides the detailed specifications for each tooth coil. Note that both tooth coils have the same number of turns and approximately the same resistance. This means both coils produce approximately the same losses for a given current (and thus torque). The main reason for this is the larger cross-section of the aluminum foil conductor, which is possible due to a more space-efficient stacking of the foil and a thinner electrical insulation layer. For mechanical stability reasons both stators were impregnated in an epoxy resin; therefore, they

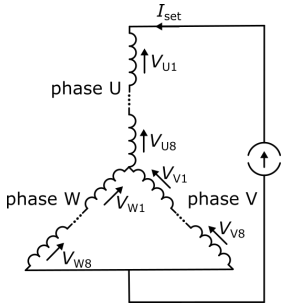

Figure 5.6: Phase connection to emulate worst-case loss distribution.

Figure 5.7: Prototype tooth coils. Left: enamelled copper wire tooth coil, Right: anodized aluminum foil tooth coil.

exhibit the same appearance after impregnation and only one stator is shown in Figure 5.5.

Since both terminals of each coil are accessible, all slot/pole combinations of Figure 5.3 can be realised experimentally. It also enables the measurement of the voltage over every single tooth coil and thus the determination of the dissipated power in each tooth coil. This enables the consideration of the difference in resistance between tooth coils due to a different average coil temperature.

To study the influence of a thermal end-winding interconnection, a removable aluminum ring with a thickness of 3.5 mm is used at the inner diameter of the stator (see (1) on Figure 5.5). Thermal paste is used to ensure a good thermal contact between the ring and the end-winding region. Since the stator with round enamelled copper wire and the stator with anodized aluminum foil are geometrically identical, the ring fits in both stators.

Every single tooth coil of both stator variants is instrumented with a PT100 temperature sensor at the inner diameter of each iron core segment (see Figure 5.8). This is the hotspot location in a stator in case of uniform losses [2].

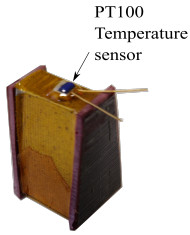

Figure 5.8: Indication of the PT100 temperature sensor location.

Additionally, PT100 temperature sensors have been placed at certain locations at the outer diameter of the aluminum housing as well (e.g., see (2) in Figure 5.5). Due to spatial periodicity in the worst-case loss distribution, it is not necessary to measure the temperature of every tooth coil. For the slot/pole combinations that result in 4 and 2 adjacent tooth coils ($n = 4$ or 2), it is sufficient to consider only one quarter of the stator. For $n = 1$, $1/8$th of a stator is even sufficient. To account for variations in the thermal properties between coils due to manufacturing imperfections, the hotspot temperature (i.e., the temperature in the centre of phase *U*) in two different spatial periods of the stator is measured. At the same angular location as the hotspot, also the temperature at the outer diameter of the housing is measured.

Besides temperature measurements, also the voltage over every single tooth coil in the half stator of Figure 5.5 is measured. The currents in phase *U* and *V* are measured using a Tektronix® TCPA 300 current amplifier. A dSPACE MicroLabBox® platform was used for data-acquisition. All signals were sampled at 1 kHz and filtered with a moving average filter over 100 ksamples effectively eliminating the influence of random errors. Since the same measurement equipment is used and the quantities are only compared relatively, the influence of deterministic error is also minimized.

5.3.2 3D Thermal FE Model

To support the analysis of the experimental data, a 3D thermal FE model is developed in this section. The model will first be calibrated using experimental data to find the model parameters that result in a good agreement between model predictions and measurements.

Geometry

As already mentioned in Section 5.3.1, it is sufficient to consider only one quarter of a full stator due to the periodicity in the worst-case loss distribution. The full geometry of the FE model thus consists of 6 adjacent tooth coils. Figure 5.9 depicts a single tooth coil of the modelled geometry of the 3D ther-

Table 5.3: Specifications of the prototype tooth coil.

Enamelled Copper Wire (Grade I, IEC 60317-13)	**Symbol**	**Value**	**Unit**
Number of turns	n_{turns}	35	/
Nominal outer diameter	$d_{\text{Cu,o}}$	0.8425	mm
Conductor diameter	$d_{\text{Cu,i}}$	0.8	mm
Winding length (incl. terminals)	l_{Cu}	276	cm
measured DC resistance (@ 25 °C)	$R_{\text{DC,Cu}}$	94.54 ± 0.37 [1]	mΩ
Height laminated iron core	h_{core}	20	mm
Weight of tooth coil	$m_{\text{Cu+SiFe}}$	31.3	g
Resistivity copper	ρ_{Cu}	1.72×10^{-8}	Ωm
Resistance temperature coeff.	α_{Cu}	3.93×10^{-3}	K^{-1}
Fill factor	$f_{\text{Cu,coil}}$	49	%
Dielectrical strength (IEC 60317-0-1)	E_{max}	87	V_{RMS}/μm
Price/kg		16.64	EUR/kg
Anodized aluminum foil			
Number of turns	n_{turns}	35	/
foil width	h_{Al}	10	mm
total foil thickness	$t_{\text{Al,tot}}$	86	$^{\text{A}}\mu$m
thickness Al_2O_3 layer	t_{AlOx}	4.6	$^{\text{A}}\mu$m
Foil length (excl. terminals)	l_{Cu}	250	cm
Cu terminal length (dia. 0.9 mm)	l_{term}	40	cm
measured DC resistance (@ 25 °C)	$R_{\text{DC,Al}}$	95.83 ± 0.6 [1]	mΩ
Height laminated iron core	h_{core}	20	mm
Weight of tooth coil	$m_{\text{Al+SiFe}}$	25.8	g
Resistivity aluminum	ρ_{Al}	2.74×10^{-8}	Ωm
Resistance temperature coeff.	α_{Al}	4.03×10^{-3}	K^{-1}
Fill factor	$f_{\text{Al,coil}}$	75	%
Dielectrical strength (ISO 2376)	E_{max}	26.5	V_{RMS}/μm
Price/kg		685 [2]	EUR/kg

[1] mean and standard deviation over 24 tooth coils. [2] Note that this is the cost for a small order quantity of 2 kg; for larger order quantities, the cost will be lower.

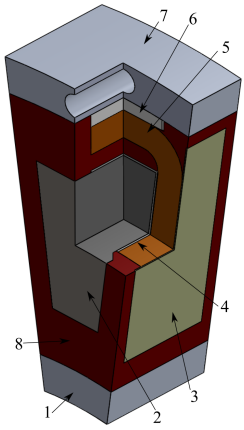

Figure 5.9: Concentrated winding tooth coil: (1) Aluminum thermal end-winding interconnection ring; (2) Laminated iron core; (3) Mica inter coil insulation sheet; (4) Mica slot liner; (5) Winding body; (6) Aluminum-oxide thermal pad; (7) Aluminum housing; (8) Epoxy potting.

mal FE model. It consists of a winding body of either round enamelled copper wire or anodized aluminum foil (5) wound on a laminated iron core (2). A mica sheet (3) with a thickness of 0.2 mm is used as inter coil insulation and a solid aluminum-oxide pad (6) is used as electrical insulation between coil and housing (phase-to-ground insulation). Optionally, a thermal end-winding interconnection ring (1) can be included in the model as well. The coil assembly was potted in a low viscosity epoxy resin.

Thermal Interfaces

The gap between the end-winding and the thermal end-winding ring is filled with epoxy. This gap is modelled in full detail and can be varied from 0 to 3.7 mm.

Since the phase-to-ground insulation consists of a rigid, non-deformable material (aluminum-oxide), the low viscosity potting resin also flows in the small gaps between the winding body and the housing. Since it is not feasible to model these gaps in full detail, a fill factor f_{pad} is introduced:

$$f_{\text{pad}} = \frac{t_{\text{AlOx-pad}}}{t_{\text{AlOx-pad}} + t_{\text{gap,equi}}}, \tag{5.5}$$

with $t_{\text{AlOx-pad}}$ as the thickness of the aluminum-oxide pad between winding and housing and $t_{\text{gap,equi}}$ the equivalent thickness of the gaps filled with epoxy. The phase-to-ground insulation will be modelled as an amalgam of aluminum-

oxide and epoxy resin. The fill factor will be used for the calculation of the equivalent thermal conductivity in Section 5.3.2.

Anisotropic Material Modelling

The winding body, the laminated iron core and the phase-to-ground insulation exhibit anisotropic thermal properties since these bodies consist of strands or laminations of different materials with different thermal properties. As already explained in Section 5.2.4, this will be modelled via two equivalent thermal conductivities. One for the direction along the strand or lamination k_1 and one for the direction perpendicular to the strand or out of the lamination plane k_2.

For the epoxy impregnated, enamelled copper wire winding body, the equivalent thermal conductivities are calculated through the use of the Hashin and Shtrikman approximation [19]:

$$k_{1,\mathrm{wi}}^{\mathrm{Cu}} = f_{\mathrm{wi}}^{\mathrm{Cu}} \cdot k_{\mathrm{Cu}} + (1 - f_{\mathrm{wi}}^{\mathrm{Cu}}) \cdot k_{\mathrm{Ep}} \tag{5.6}$$

$$k_{2,\mathrm{wi}}^{\mathrm{Cu}} = k_{\mathrm{Ep}} \cdot \frac{(1 + f_{\mathrm{wi}}^{\mathrm{Cu}}) \cdot k_{\mathrm{Cu}} + (1 - f_{\mathrm{wi}}^{\mathrm{Cu}}) \cdot k_{\mathrm{Ep}}}{(1 - f_{\mathrm{wi}}^{\mathrm{Cu}}) \cdot k_{\mathrm{Cu}} + (1 + f_{\mathrm{wi}}^{\mathrm{Cu}}) \cdot k_{\mathrm{Ep}}} \tag{5.7}$$

For the anodized aluminum foil winding body, a two-step approach is followed: first, the equivalent properties of the anodized foil are calculated and subsequently, these properties are used to calculate the properties of an impregnated anodized aluminum foil winding body.

Step 1:

$$k_{1,\mathrm{afol}} = f_{\mathrm{afol}} \cdot k_{\mathrm{Al}} + (1 - f_{\mathrm{afol}}) \cdot k_{\mathrm{AlOx,film}} \tag{5.8}$$

$$k_{2,\mathrm{afol}} = \frac{k_{\mathrm{Al}} \cdot k_{\mathrm{AlOx,film}}}{(1 - f_{\mathrm{afol}}) \cdot k_{\mathrm{Al}} + f_{\mathrm{afol}} \cdot k_{\mathrm{AlOx,film}}}, \tag{5.9}$$

where k_{Al} and k_{AlOx} are the thermal conductivity of aluminum and aluminum-oxide film, respectively. The fill factor for this combination is defined as:

$$f_{\mathrm{afol}} = \frac{t_{\mathrm{Al,tot}} - 2 \cdot t_{\mathrm{AlOx}}}{t_{\mathrm{Al,tot}}}, \tag{5.10}$$

where $t_{\mathrm{Al,tot}}$ is the thickness of the anodized aluminum foil and t_{AlOx} the thickness of the aluminum-oxide insulation film on the foil.

Step 2:

$$k_{1,\mathrm{wi}}^{\mathrm{Al}} = f_{\mathrm{wi}}^{\mathrm{Al}} \cdot k_{1,\mathrm{afol}} + (1 - f_{\mathrm{wi}}^{\mathrm{Al}}) \cdot k_{\mathrm{Ep}}, \tag{5.11}$$

where $f_{\mathrm{wi}}^{\mathrm{Al}}$ is the fill factor of the impregnated winding body, $k_{1,\mathrm{afol}}$, the equivalent thermal conductivity of the anodized foil in the plane of the foil and k_{Ep}, the thermal conductivity of the epoxy resin. For the thermally poor conducting direction, the equivalent thermal conductivity can be calculated using the

series material model from [19]:

$$k_{2,\text{wi}}^{\text{Al}} = \frac{k_{2,\text{afol}} \cdot k_{\text{Ep}}}{(1 - f_{\text{wi}}^{\text{Al}}) \cdot k_{2,\text{afol}} + f_{\text{wi}}^{\text{Al}} \cdot k_{\text{Ep}}}, \tag{5.12}$$

where $k_{2,\text{afol}}$ is the equivalent thermal conductivity of the anodized foil perpendicular to the plane of the foil.

The laminated iron core is an amalgam of electrical steel sheets and a thin adhesive layer to bond the sheets together. The equivalent thermal conductivities are also calculated using the series-parallel model from [19]:

$$k_{1,\text{core}} = f_{\text{core}} \cdot k_{\text{FeSi}} + (1 - f_{\text{core}}) \cdot k_{\text{Ep}} \tag{5.13}$$

$$k_{2,\text{core}} = \frac{k_{\text{FeSi}} \cdot k_{\text{Ep}}}{(1 - f_{\text{core}}) \cdot k_{\text{FeSi}} + f_{\text{core}} \cdot k_{\text{Ep}}}, \tag{5.14}$$

where f_{core} is the fill factor of the laminated iron core and k_{FeSi} the thermal conductivity of electrical steel.

As already mentioned in Section 5.3.2, the phase-to-ground insulation will be modelled as an amalgam of aluminum-oxide and epoxy resin. The equivalent thermal conductivities are again calculated using the series-parallel model from [19]:

$$k_{1,\text{pad}} = f_{\text{pad}} \cdot k_{\text{AlOx}} + (1 - f_{\text{pad}}) \cdot k_{\text{Ep}} \tag{5.15}$$

$$k_{2,\text{pad}} = \frac{k_{\text{Ep}} \cdot k_{\text{AlOx}}}{(1 - f_{\text{pad}}) \cdot k_{\text{AlOx}} + f_{\text{pad}} \cdot k_{\text{Ep}}}. \tag{5.16}$$

Boundary Conditions

As already explained in Section 5.3.1, convective heat transfer at the airgap surface is neglected. It is assumed that all heat is dissipated via forced convection over the housing at the outer diameter.

Transient Model Calibration

To calibrate the 3D thermal FE model, the coils of both the stator with round enamelled copper wire and the stator with anodized aluminum are configured to emulate a 24 slot, 22 or 26 poles combination as depicted in Figure 5.10. Initially, the stator is in thermal equilibrium with its environment. A constant current $I_{\text{set}} = 4A$ is then injected in phase U which corresponds to 21 W dissipated power in the motor. For 100 min, the hotspot and corresponding housing temperatures of selected coils, all coil voltages, and the phase currents are recorded. The voltage and current measurements are used to calculate the power losses at every time step, these serve as inputs for the FE model

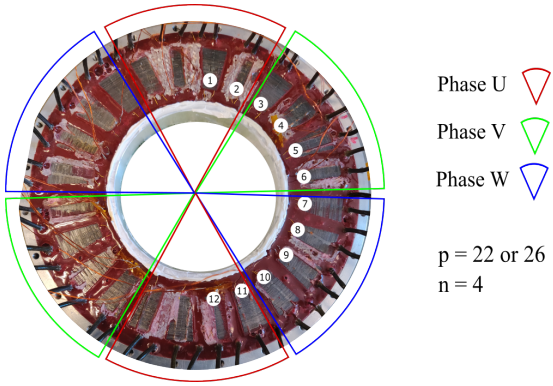

Figure 5.10: Indication of the PT100 temperature sensor location.

transient simulation. These transient experiments are performed once for a stator without thermal end-winding interconnection ring and once for a stator with thermal end-winding interconnection ring. The results from both the simulation with the 3D thermal FE model and the measurements are given in Figures 5.11 and 5.12. The numbering of the temperature signals corresponds to the numbering of the tooth coils in Figure 5.10. The parameters used for the simulations are given in Table 5.4. Due to the temperature limit of the used epoxy resin, the maximum hotspot temperature was kept below 80 °C. The maximum difference between the estimated and the measured temperature is smaller than 2 °C. It can be concluded that the simulations are in good agreement with the measurements for both the round enamelled copper wire stator and the anodized aluminum foil winding stator, and for the case with and without thermal end-winding interconnection ring. Note that it is not possible to draw conclusions on the relative performance of the different cases since only absolute temperature are given in Figures 5.11 and 5.12 which depend on the ambient temperature and convective heat transfer coefficient of the housing. The 3D thermal FE model can thus reliably be used to support the experimental data analysis in order to obtain a better understanding of the measurement results.

Steady-State Temperature Distribution

Using the calibrated model from Section 5.3.2, the steady-state temperature distribution can be calculated. This is illustrated for the scenario from Figure 5.11a, i.e., the stator with round enamelled copper wire without thermal end-winding interconnection, with a 24 slots, 22 or 26 poles combination and $I_{\mathrm{u}} = 2 \cdot I_{\mathrm{v}} = 2 \cdot I_{\mathrm{w}} = 4$ A in Figure 5.13.

As expected, the highest temperatures are found in the coils belonging

Table 5.4: Thermal Finite Element Model Parameters.

Parameter	Value	Unit
k_{Cu}	385	W/mK
k_{Al}	237	W/mK
k_{Ep}	0.37	W/mK
$k_{\mathrm{AlOx,film}}$	1.6	W/mK
k_{AlOx}	20	W/mK
k_{FeSi}	28	W/mK
$f_{\mathrm{wi}}^{\mathrm{Cu}}$	0.49	[/]
f_{afol}	0.89	[/]
$f_{\mathrm{wi}}^{\mathrm{Al}}$	0.75	[/]
f_{core}	0.98	[/]
f_{pad}	0.88	[/]
$k_{\mathrm{1,wi}}^{\mathrm{Cu}}$	189	W/mK
$k_{\mathrm{2,wi}}^{\mathrm{Cu}}$	1.08	W/mK
$k_{\mathrm{1,afol}}$	212	W/mK
$k_{\mathrm{2,afol}}$	14.3	W/mK
$k_{\mathrm{1,wi}}^{\mathrm{Al}}$	159	W/mK
$k_{\mathrm{2,wi}}^{\mathrm{Al}}$	1.37	W/mK
$k_{\mathrm{1,core}}$	27.4	W/mK
$k_{\mathrm{2,core}}$	0.37	W/mK
$k_{\mathrm{1,pad}}$	17.6	W/mK
$k_{\mathrm{2,pad}}$	2.72	W/mK
C_{Ep}	798	J/kgK
C_{Cu}	385	J/kgK
C_{FeSi}	490	J/kgK
C_{Al}	897	J/kgK
C_{AlOx}	880	J/kgK

to phase *U* since the losses in phase *U* are four times higher than in phase *V*. It can also be observed that there is a temperature difference between the coils of phase *U* clearly proving the presence of a heat flux in the tangential direction, i.e., heat is redistributed from coils with higher losses to coils with lower losses.

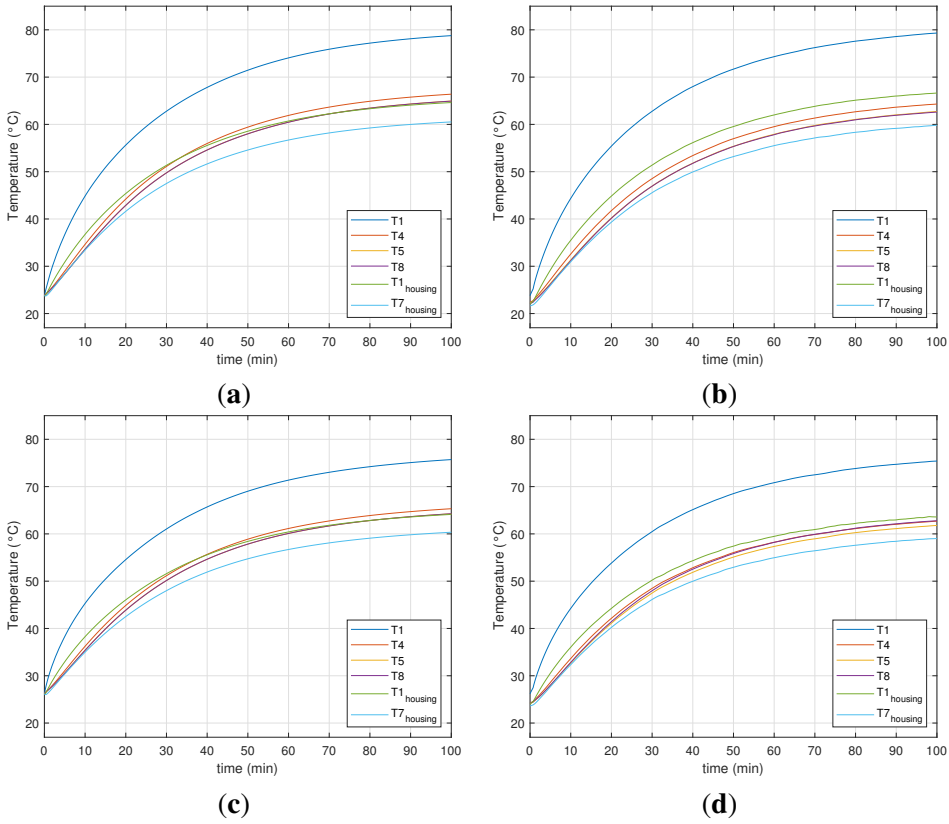

Figure 5.11: Transient temperature evolution at selected locations (see Figure 5.10) in a stator with round enamelled copper wire for a 24 slot, 22 or 26 pole combination. (**a**) Simulated temperatures—stator without end-winding ring. (**b**) Measured temperatures—stator without end-winding ring. (**c**) Simulated temperature—stator with end-winding ring. (**d**) Measured temperatures—stator with end-winding ring.

5.4 Results

5.4.1 Experimental Results

To study the influence of the slot/pole combination, thermal end-winding interconnection and equivalent winding body thermal conductivity on the stall torque performance, 10 experiments are performed in which the slot/pole combination, the presence of a thermal end-winding ring and the conductor material are varied. Table 5.5 specifies the test conditions for each experiment.

To emulate a stall torque loss distribution, the stator coils are connected

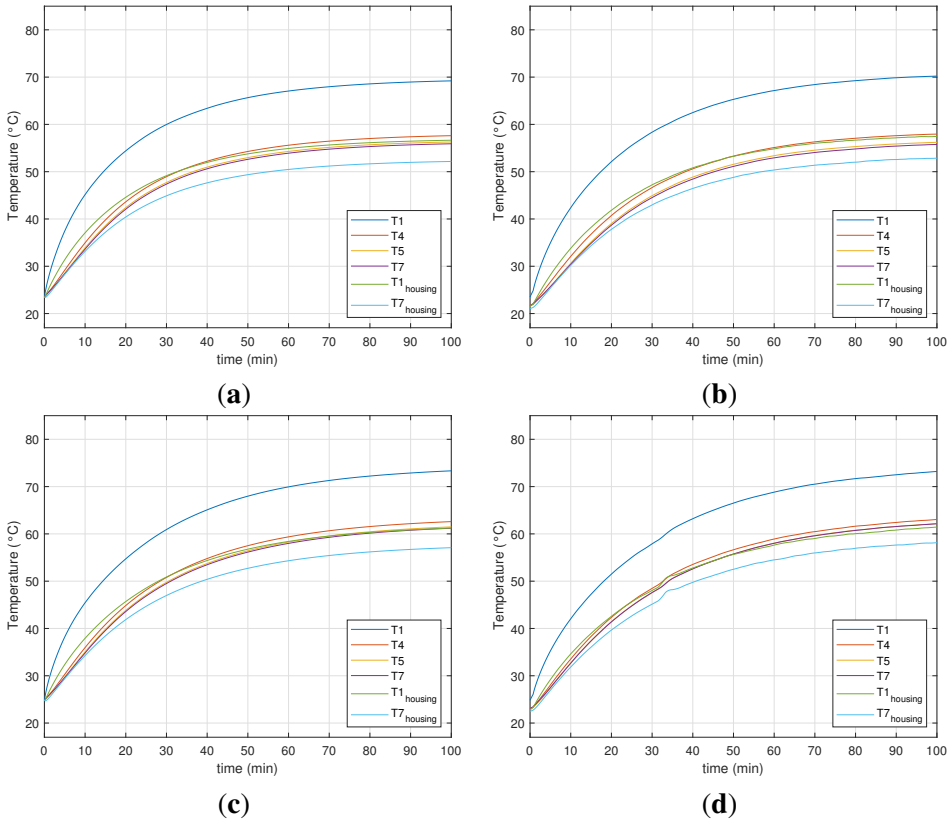

Figure 5.12: Transient temperature evolution at selected locations (see Figure 5.10) in a stator with anodized aluminum foil winding for a 24 slot, 22 or 26 pole combination. (**a**) Simulated temperatures—stator without end-winding ring. (**b**) Measured temperatures—stator without end-winding ring. (**c**) Simulated temperatures—stator with end-winding ring. (**d**) Measured temperatures—stator with end-winding ring.

as shown in Figure 5.6. A constant current $I_{\text{set}} = 4A$ is injected in phase U, which corresponds to 21 W dissipated power in the motor. The stall torque temperature distribution will be compared with the temperature distribution under uniform losses. To emulate this scenario, all coils of the stator are connected in series and a constant current $I_{\text{set}}^{\text{uniform}} = 2.8A = 4/\sqrt{2}A$ is injected into this ring network, also resulting in 21 W dissipated power. After 100 minutes, thermal steady-state is reached i.e. the time derivative of all temperatures has dropped below 0.5°/10 min, and the hotspot and corresponding housing temperatures, coil voltages and phase currents are recorded. The recorded values are used to calculate the thermal resistance between the hotspot and the

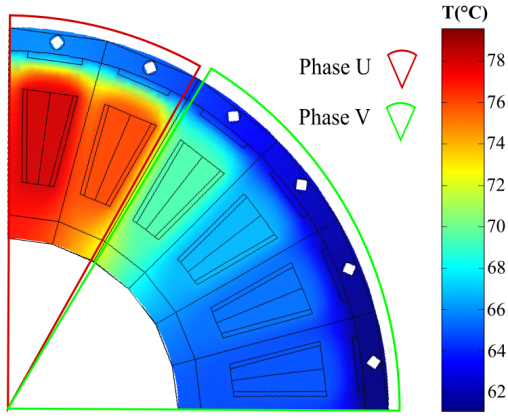

Figure 5.13: Steady-state temperature distribution in the stator with round enamelled copper wire without thermal end-winding interconnection, with a 24 slots, 22 or 26 poles combination

Table 5.5: Measured thermal resistance between hotspot and housing surface.

n	**Thermal End-Winding Connection (Yes/No)**	**Al/Cu**	R_{hotspot} **(K/W)**	$\frac{Q_{\text{stall}}}{2 \cdot Q_{\text{uniform,s24p22}}}$
4	No	Cu	7.89	0.534
4	Yes	Cu	7.29	0.578
2	No	Cu	6.44	0.655
2	Yes	Cu	6.34	0.665
1	No	Cu	4.86	0.866
1	Yes	Cu	4.90	0.860
4	No	Al	7.33	0.536
4	Yes	Al	6.43	0.611
	uniform losses	Cu	8.42	
	uniform losses	Al	7.86	

housing at the same angular position (θ^*) as:

$$R_{\text{hotspot}} = \frac{T_{\text{hotspot}}(\theta^*) - T_{\text{housing}}(\theta^*)}{Q_{\text{coil},U}} \qquad (5.17)$$
$$Q_{\text{coil},U} = V_{\text{coil},U} \cdot I_U,$$

where $T_{\text{hotspot}}(\theta^*)$ is the temperature in the hotspot of a coil (see Figure 5.8) in the centre of phase U, $T_{\text{housing}}(\theta^*)$ is the temperature of the

housing (see (2) in Figure 5.5) at the same angular location θ^*, $Q_{\text{coil},U}$ is the dissipated power in this coil, which is the product of the voltage $V_{\text{coil},U}$ over and the current I_U through the coil. The thermal resistance is preferred as a metric to compare the experimental results over the absolute or relative temperature since this metric is less sensitive to variations in ambient conditions (e.g. ambient temperature and housing convective heat transfer coefficient). As already mentioned in Section 5.3.1, two hotspot and housing temperatures are measured in different spatial periods of the stator, the average of thermal resistance of both is given in Table 5.5. Note that the thermal resistance in all cases is lower compared to the thermal resistance in case of uniform losses. This could be expected since a part of the losses of phase U are dissipated via the other phases, hence the decrease in the effective thermal resistance of phase U. Although the thermal resistance is lower in case of uneven loss distribution, the temperature is still higher in comparison to a uniform loss distribution because two times more losses are dissipated in phase U in case of uneven loss distribution. Therefore, the maximum stall torque is lower than the maximum torque at low speed. Low speed means sufficiently high such that a uniform loss distribution can be assumed, but low enough such that iron and mechanical losses can be neglected. The ratio of the maximum stall torque over the torque at low speed will be used as a performance metric to quantify the stall torque performance of a motor. This ratio can also be interpreted as a 'torque derating factor at standstill':

$$\frac{T_{\text{stall}}}{T_{\text{uniform,ref}}}, \tag{5.18}$$

where $T_{\text{uniform,ref}}$ is the maximum torque under uniform losses at low speed for a reference scenario. The calculation of the torque derating factor as well as the definition of the reference scenario will be discussed in detail in the following paragraphs.

Influence of Slot/Pole Combination

To study the influence of the slot/pole combination, $T_{\text{uniform,ref}} = T_{\text{uniform,s24p22}}$ with $T_{\text{uniform,s24p22}}$ the maximum torque under uniform losses at low speed for a stator without end-winding ring and for the slot/pole combination with the highest $\xi \cdot k'_\phi$, i.e. 24 slots and 22 poles. This factor is now calculated using the measured thermal resistance from Table 5.5 and the fundamental winding factor and back-emf constant from Table 5.2:

$$\frac{T_{\text{stall}}}{T_{\text{uniform,s24p22}}} = \frac{\xi \cdot k'_\phi \cdot I_{\text{stall}}}{\xi_{\text{s24p22}} \cdot k'_{\phi,s24p22} \cdot I_{\text{uniform,s24p22}}}. \tag{5.19}$$

The currents can be expressed in terms of the dissipated power losses in phase U:

$$Q_{U,\text{stall}} = R_U \cdot (1 + \alpha \Delta T_{\text{stall}}) \cdot I^2_{U,\text{stall}} \tag{5.20}$$

and

$$Q_{U,\text{uniform,s24p22}} = R_U \cdot (1 + \alpha \Delta T_{\text{uniform,s24p22}}) \cdot I^2_{U,\text{uniform,s24p26}} \tag{5.21}$$

and since for the worst-case standstill position $I_{U,\text{stall}} = \sqrt{2} \cdot I_{\text{stall}}$, Equation (5.20) becomes:

$$Q_{U,\text{stall}} = R_U \cdot (1 + \alpha \Delta T_{\text{stall}}) \cdot (\sqrt{2} I_{\text{stall}})^2, \tag{5.22}$$

with α, the resistance temperature coefficient, ΔT_{stall} and $\Delta T_{\text{uniform,s24p22}}$, the difference between the winding temperature and the reference temperature at which the winding resistance R_U was determined. To obtain a fair comparison between the cases in Table 5.5, it is assumed that $\Delta T_{\text{stall}} = \Delta T_{\text{uniform,s24p22}}$ and R_U is assumed the same for all slot/pole combinations of the stator with round copper wire in Table 5.5, Equation (5.19) now becomes the following:

$$\frac{T_{\text{stall}}}{T_{\text{uniform,s24p22}}} = \frac{\xi \cdot k'_\phi}{\xi_{\text{s24p22}} \cdot k'_{\phi,s24p22}} \cdot \sqrt{\frac{Q_{\text{stall}}}{2 \cdot Q_{\text{uniform,s24p22}}}} \tag{5.23}$$

$$\frac{Q_{\text{stall}}}{Q_{\text{uniform,s24p22}}} = \frac{\frac{\Delta T_{\text{stall}}}{R_{\text{hotspot,stall}}}}{\frac{\Delta T_{\text{uniform,s24p22}}}{R_{\text{hotspot,uniform,s24p22}}}} = \frac{R_{\text{hotspot,uniform,s24p22}}}{R_{\text{hotspot,stall}}}. \tag{5.24}$$

The ratio $\frac{Q_{\text{stall}}}{Q_{\text{uniform,s24p22}}}$ can now be found using the thermal resistance measurements from Table 5.5. The assumption of equal temperature difference between hotspot and housing in the 'stall torque case' and the 'uniform losses reference case' $\Delta T_{\text{stall}} = \Delta T_{\text{uniform,s24p22}}$ entails that the hotspot temperature in both cases is the same if the housing temperature is the same. The same hotspot temperature means that in both cases the motors operate at their thermal limit.

To study the influence of the slot/pole combination on the stall torque performance, the coils of the stator of the prototype YASA AFPMSM (Figure 5.5) are allocated to a phase as shown in Figure 5.3 and their terminals are connected according to Figure 5.6. Experiments are performed as described in Section 5.4.1. First, the ratio $Q_{\text{stall}}/Q_{\text{uniform,s24p22}}/2$ is considered. This ratio is also given in Table 5.5 and can be interpreted as the ratio of the total losses that can be dissipated in a motor producing torque at standstill over the losses that can be dissipated in a motor with uniform loss. To have a fair compari-

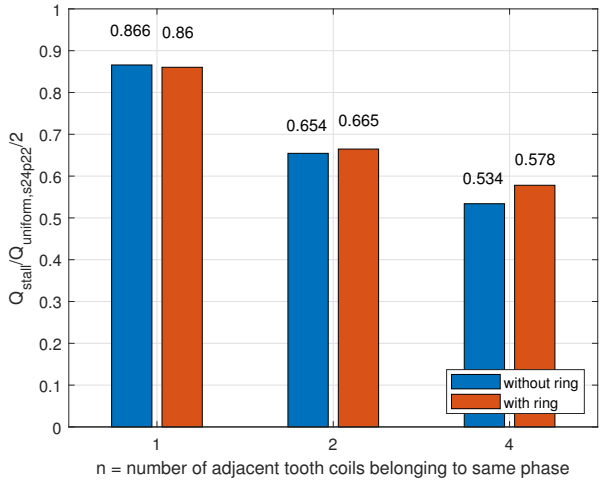

Figure 5.14: Measured ratio of the losses that can be dissipated in under stall torque conditions over the losses that can be dissipated in case of uniform loss distribution for various slot/pole combinations (see Figure 5.3) and for the cases with and without thermal end-winding interconnection.

son, in both cases, the losses result in the same temperature difference between hotspot and housing. The results from Table 5.5 are visualised in a bar plot in Figure 5.14. It is clear that the number of adjacent coils belonging to the same phase has a large influence on the ratio $Q_{\text{stall}}/Q_{\text{uniform,s24p22}}/2$. For the case $n = 4$, which corresponds to 24 slots and either 22 or 26 poles, even 47% less power can be dissipated to obtain the same difference between hotspot and housing as compared to the case of a uniform loss distribution. The slot/pole combinations with $n = 1$ exhibit the best thermal performance because losses from phase *U* can be very effectively dissipated via the tooth coils from phases *V* and *W* due to the large surface area between the phases since every tooth coil from phase *U* has two neighbouring tooth coils from other phases.

The superior thermal performance of the slot/pole combinations with $n = 1$ does not necessarily imply superior stall torque performance. The torque derating factor $T_{\text{stall}}/T_{\text{uniform,s24p22}}$ for various slot/pole combinations is shown in Figure 5.15. It can be seen that the combination of 24 slots and 20 poles exhibits the highest stall torque performance because this combination combines good thermal performance (see Figure 5.14) with a good winding factor and back-emf constant. The stall torque of this slot/pole combination is 8.5% higher than the slot/pole combination in the prototype YASA AFPMSM (24 slot, 26 poles). However, the differences between slot/pole combinations in terms of the stall torque performance are less pronounced than in terms of the thermal performance (see Figure 5.14).

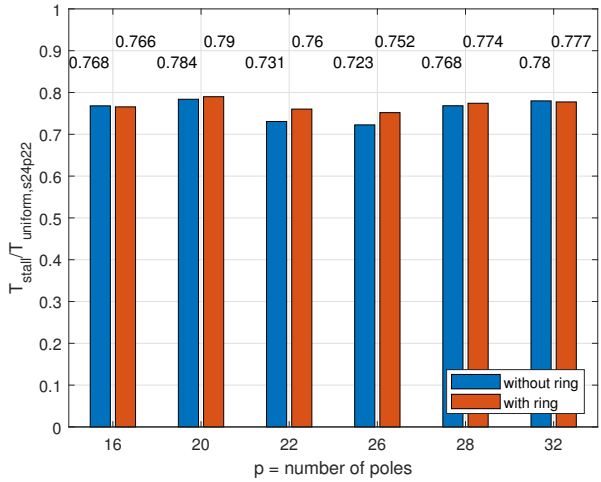

Figure 5.15: Measured torque derating factor $T_{\text{stall}}/T_{\text{uniform,s24p22}}$ for various slot/pole combinations and for the case with and without thermal end-winding interconnection.

Influence of Thermal End-Winding Interconnection

To study the influence of a thermal end-winding interconnection on the stall torque performance, a solid aluminum ring is inserted at the inner diameter of the stator prototypes and the same experiments as described in Sections 5.4.1 and 5.4.1 are repeated. The results in terms of the thermal performance were already given in Table 5.5 and are shown in Figure 5.14. The addition of a thermal end-winding ring results in 0.6% up to 4% increase in thermal performance for $n = 1$ and $n = 4$, respectively, compared to the case without end-winding ring. This confirms that a thermal end-winding interconnection contributes in redistributing the heat from phase U to the other phases. The influence is more pronounced for $n = 4$ because in this case the surface area for heat transfer between phases is limited and thus, adding a thermal end-winding interconnection has more impact on the thermal performance. However, compared to the influence of the slot/pole combination on the thermal performance or stall torque performance, the influence of an end-winding ring is lower. A possible explanation for this is the presence of a large gap (2 mm) filled with epoxy between the end-winding and the end-winding interconnection ring. The influence of this gap will be studied in more detail in Section 5.4.2.

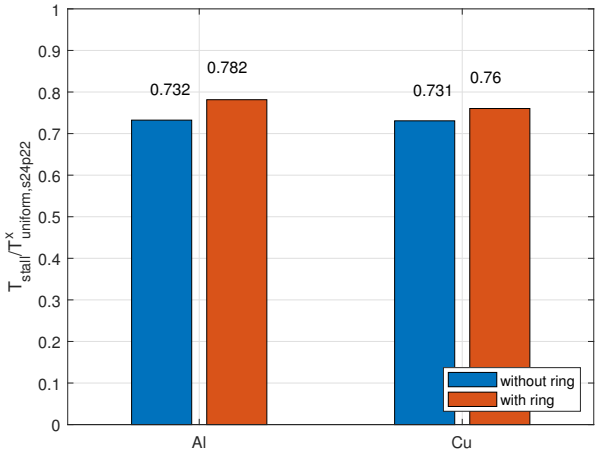

Figure 5.16: Measured torque derating factor $T_{\text{stall}}/T^{\text{x}}_{\text{uniform,s24p22}}$ with x $\in$ {Al,Cu}for different conductor types, for $n = 4$, and for the case with and without thermal end-winding ring.

Influence of Equivalent Winding Body Thermal Conductivity

The influence of the equivalent thermal conductivity of the winding body is studied by comparing a stator with round enamelled copper wire as conductor and a stator with anodized aluminum foil as conductor. The experiments as described in Section 5.4.1 are performed on both stators for $n = 4$ (see Figure 5.3), once without the end-winding interconnection and once with the end-winding interconnection. The outcome of the experiments was already given in Table 5.5. $T_{\text{uniform,ref}}$ in the torque derating factor $T_{\text{stall}}/T_{\text{uniform,ref}}$ is now defined as $T^{\text{x}}_{\text{uniform,s24p22}}$ with x $\in$ {Al,Cu} i.e., the maximum torque under uniform losses at low speed for either the stator with anodized aluminum foil winding or with round enamelled copper wire, without end-winding ring and the slot/pole combination with the highest $\xi \cdot k'_{\phi}$, i.e., 24 slots and 22 poles. The results are visualised in Figure 5.16.

No significant difference can be observed between the two conductor types. Although, it was expected that the stator with anodized aluminum foil winding would have a better stall torque performance due to its higher equivalent thermal conductivity in the direction out of the plane of the foil, i.e., $k^{\text{Al}}_{2,\text{wi}}$. However, since no explanation can be given at this point, this aspect will be further investigated with the aid of the 3D thermal FE model in Section 5.4.2.

5.4.2 Experimental Data Analysis through Simulation

Influence of Gap between End-Winding and End-Winding Interconnection Ring

It was mentioned in Section 5.4.1 that the addition of a thermal end-winding interconnection ring had less influence on the stall torque performance in comparison to the choice of the slot/pole combination. The presence of a gap filled with epoxy in between the end-winding and the ring was mentioned as a possible explanation. To study whether a higher stall torque performance can be obtained through the addition of a thermal end-winding ring if this gap is thinner, the calibrated 3D thermal FE model from Section 5.3.2 will be used here. The gap between the end-winding and the end-winding ring is decreased to its minimal value, the power losses in each tooth coil recorded during the experiments described in Section 5.4.1 are used as inputs for the simulation. The torque derating factor $T_{\text{stall}}/T_{\text{uniform,s24p22}}$ is again calculated using the simulated steady-state temperature distribution for various slot/pole combinations for the stator with copper wire winding for both the case without end-winding ring and the case with a minimal gap between the end-winding and end-winding ring. The results are given in Figure 5.17a.

The addition of a thermal end-winding interconnection ring with minimum gap between end-winding and ring allows to increase the stall torque performance by up to 8.2%, whereas this was only 4% with a gap of two millimetres as mentioned in Section 5.4.1.

To compare the actual stall torque values for the different cases, the maximum stall torque for the various cases is shown in Figure 5.17b. The maximum stall torque is defined as the torque that results in a hotspot temperature of $150\ ^\circ$C. This torque was calculated using the current that results in a hotspot temperature of $150\ ^\circ$C, Equation (5.1) and the values from Table 5.2. The current was found iteratively using the thermal FE model. It can be seen that there is a difference of 0.5 Nm in maximum stall torque between the slot/pole combinations 24/16 and 24/20.

When comparing Figures Figure 5.17a and b, it can be seen that there is a larger difference between the cases with ring and without ring on Fig. Figure 5.17a than on Fig. Figure 5.17b. This is because the metric in Fig. Figure 5.17a is insensitive to environmental conditions like convection coefficient on the housing. In Fig. Figure 5.17b, a certain convection coefficient on the housing is assumed as stated in Section 5.3.2. If convection is the thermal bottleneck, the presence or absence of a thermal end-winding ring will have less influence on performance and therefore there is less difference between the cases with and without thermal end-winding ring in Fig. Figure 5.17b.

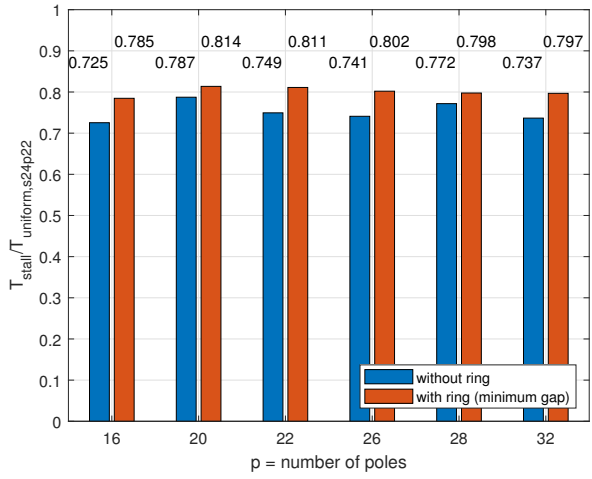

(**a**)

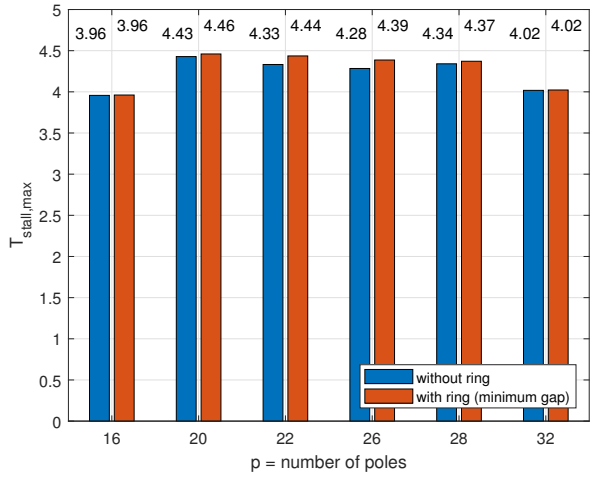

(**b**)

Figure 5.17: Simulated (**a**) torque derating factor $T_{\text{stall}}/T_{\text{uniform,s24p22}}$ and (**b**) maximum stall torque for various slot/pole combinations and for the case without thermal end-winding interconnection and with a thermal end-winding interconnection with a minimum gap between the end-winding and the ring. (**a**) Simulated torque derating factor $T_{\text{stall}}/T_{\text{uniform,s24p22}}$. (**b**) Simulated maximum stall torque (@ $T_{\text{hotspot}} = 150\ ^{\circ}\text{C}$).

Analysis of Equivalent Thermal Conductivity of Winding Body

The study of the influence of the equivalent winding body thermal conductivity is one of the main goals of this work; however, the experimental results from Section 5.4.1 did not allow us to draw strong conclusions. No clear difference in stall torque performance between the stator with copper wire winding and the stator with anodized aluminum foil could be found. It was expected that the higher equivalent thermal conductivity of the anodized foil in the direction out of the plane of the foil [4, 19] would lead to a better tangential heat transfer. This could not be proven experimentally.

By varying the winding fill factor in the 3D thermal FE model, the equivalent winding body thermal conductivity can be varied. The fill factor will be varied by $\pm 20\%$ with respect to its nominal value in the 3D thermal FE model and the torque derating factor $T_{\text{stall}}/T^{\text{x}}_{\text{uniform,s24p22}}$ with $\text{x} \in \{\text{Al,Cu}\}$ is again calculated based on the simulated steady-state temperature distribution. The recorded power losses from the experiments in Section 5.4.1 were used as inputs for the simulations. The results are visualised in the barplot in Figure 5.18.

It can be concluded that for both the aluminum winding and copper winding stators, the fill factor and the equivalent winding body thermal conductivity has no significant influence on the stall torque performance.

It is important to note, however, that increasing the fill factor increases both the maximum stall torque T_{stall} and the maximum torque under uniform losses at low speed $T^{\text{x}}_{\text{uniform,s24p22}}$ in the ratio $T_{\text{stall}}/T^{\text{x}}_{\text{uniform,s24p22}}$ with $\text{x} \in \{\text{Al,Cu}\}$, but it will not allow a higher maximum stall torque as compared to its maximum torque under uniform losses at low speed.

Similarly to in Section 5.4.2, the actual stall torque values for the different cases are compared in Figure 5.18. It can be seen that, also at elevated temperatures, the winding body thermal conductivity does not have a significant influence on the stall torque values. This is because the winding body thermal resistance is not dominant in the thermal path from heat source to heat sink. Therefore, changes in the thermal conductivity do not have a significant impact on the thermal performance and thus, has no impact on the stall torque performance either. It could already be seen in Figures 5.11 and 5.12 that the temperature difference between hotspot and housing was much smaller than the difference between hotspot and ambient, confirming that the thermal resistance between housing and ambient is dominant in this case.

Influence of Cyclic Loading

There are no applications in which a motor operates sufficiently long at standstill and maximum stall torque to reach thermal steady state. More frequently,

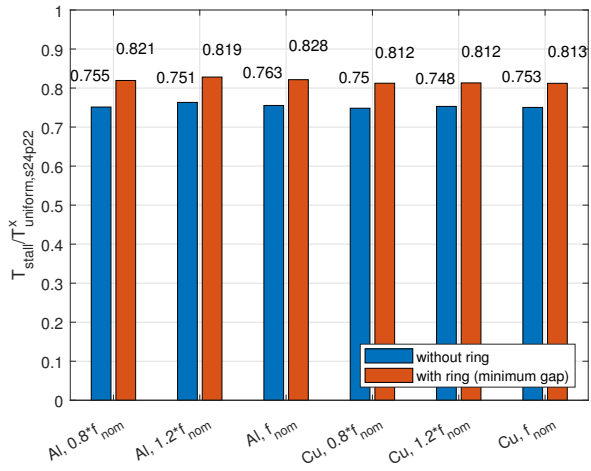

(**a**)

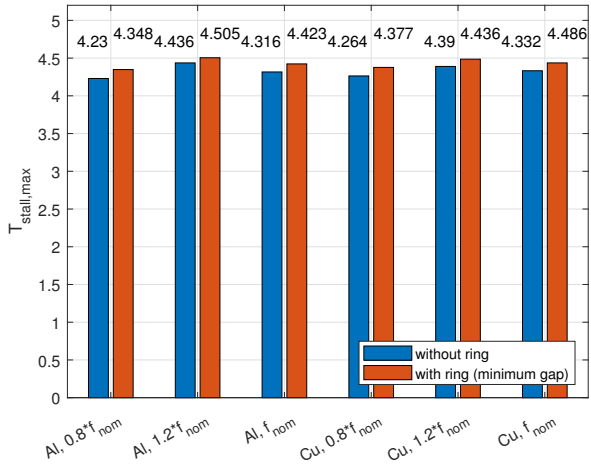

(**b**)

Figure 5.18: Simulated (**a**) torque derating factor $T_{\text{stall}}/T^{\text{x}}_{\text{uniform,s24p22}}$ with x $\in$ {Al,Cu} and (**b**) maximum stall torque, for different values of $f^{\text{Al}}_{\text{wi}}$, for different conductor types, for a 24 slots and 22 or 26 poles combination, and for the case with and without thermal end-winding ring. (**a**) Simulated torque derating factor $T_{\text{stall}}/T_{\text{uniform,s24p22}}$. (**b**) Simulated maximum stall torque (@ $T_{\text{hotspot}} = 150$ °C).

as in the case of a force-controlled robotic gripper, the load cycle of the motor consists of a long period of high torque at standstill, e.g. when the gripper is holding a soft object and short periods of low torque and high speed when the gripper is opening and closing. Since the term stall torque is frequently used in motor datasheets, it is also used as a metric here, as it is a well known and easy-to-understand term. However, it would be interesting to study the impact of a load cycle on the stall torque performance. To this end, the thermal FE model is used to simulate the following load cycle which corresponds to a realistic gripper scenario: (1) gripper grasps object at start location: high speed, gradually increasing current (duration: 4 s); (2) gripper holds object while it is moved to end position: standstill, maximum current (duration: 26 s); (3) gripper releases object at end position: high speed, gradually decreasing current (duration: 4 s); (4) gripper without object returns to start position: standstill, no current (duration: 26 s). Hence, the duty cycle for this load cycle is 50%. A scenario with uniform loss distribution as would be the case if the motor rotates when generating torque and a scenario with non-uniform loss distribution as is the case for a motor generating torque at standstill are compared. For both scenarios, the torque that results in a peak hotspot temperature of 150 °C is determined. The hotspot temperature variations for both scenarios are given in Figure 5.19. The non-smooth course of the graphs originates from the large time-step which was chosen to limit the simulation time. Larger temperature variations can be found for the case with non-uniform loss distribution since the variation of the losses is larger in case of a non-uniform loss distribution. The torque derating factor for this load cycle is then calculated as the ratio of the maximum stall torque over the maximum torque in case of uniform losses, i.e. when the losses are uniform during phase (2). The derating factor for a load cycle is compared to the derating factor for a continuous load scenario, but no difference could be observed, this allows to conclude that the stall torque derating factor for continuous load can reliably be used also in cyclic load applications.

5.5 Conclusions

In this work, the stall torque performance of a YASA AFPMSM motor was analysed. More specifically, the influence of the slot/pole combination, the addition of a thermal end-winding interconnection ring and the equivalent thermal conductivity of the winding body were studied. To this end, prototype YASA AFPMSM stators were manufactured and instrumented with temperature sensors. A uniform and an uneven loss distribution were imposed on the stators by injecting DC currents to emulate a low-speed and a standstill situation, respectively. The steady-state hotspot temperatures and losses

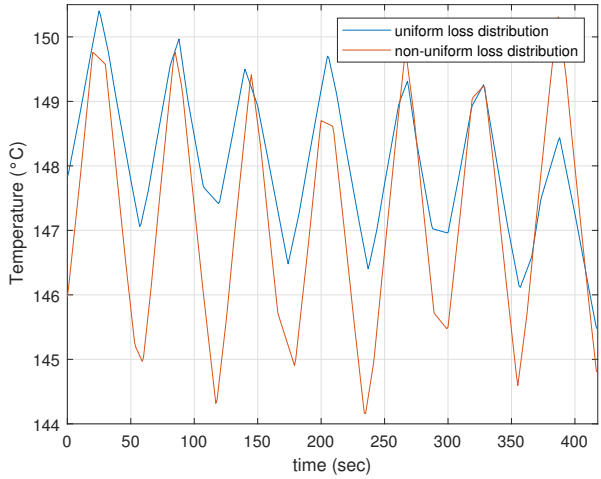

Figure 5.19: Simulated hotspot temperature variations for a load cycle with a duty cycle of 50% for a case with uniform losses (e.g., when the motor is rotating when producing torque) and for a case with non-uniform losses (e.g., when the motor is at standstill when producing torque).

were recorded and used to calculate the thermal resistance between hotspot and housing. These thermal resistances, the fundamental winding factor and the back-emf constants were then used to calculate the stall torque performance metric introduced in this work. This metric was determined for various slot/pole combinations, a stator with/without thermal end-winding interconnection and for a stator with anodized aluminum foil winding and a stator with copper wire winding to study the impact of the equivalent thermal conductivity of the winding body.

It was concluded that only the slot/pole combination and the addition of a thermal end-winding interconnection can have a significant impact on the stall torque performance (with up to 8% increase in the stall torque performance metric). The equivalent thermal conductivity of the winding body has no impact on the stall torque performance, specifically; however, a higher fill factor leads to superior thermal properties and thus, to both a higher maximum stall torque and a higher maximum torque at low speed.

References

[1] H. Vansompel, A. Hemeida, and P. Sergeant, “Stator heat extraction system for axial flux yokeless and segmented armature machines,” in *2017*

IEEE International Electric Machines and Drives Conference (IEMDC), 2017, pp. 1–7.

[2] H. Vansompel, P. Leijnen, and P. Sergeant, "Multiphysics analysis of a stator construction method in yokeless and segmented armature axial flux pm machines," *IEEE Transactions on Energy Conversion*, vol. 34, no. 1, pp. 139–146, 2019.

[3] M. Waldhof, A. Echle, and N. Parspour, "A novel drive train concept for personalized upper body exoskeletons with a multiphase axial flux machine," in *2019 IEEE International Electric Machines & Drives Conference (IEMDC)*, 2019, pp. 2160–2166.

[4] J. Van Damme, H. Vansompel, and G. Crevecoeur, "Anodised aluminium foil winding axial flux machine for direct-drive robotic applications," *IEEE Transactions on Industrial Electronics*, pp. 1–10, 2022.

[5] T. De Clercq, A. Sianov, and G. Crevecoeur, "A soft barometric tactile sensor to simultaneously localize contact and estimate normal force with validation to detect slip in a robotic gripper," *IEEE Robotics and Automation Letters*, vol. 7, no. 4, pp. 11 767–11 774, 2022.

[6] H. Gill, "Ac servo motor system the difference between continuous ratings and holding continuous loads," Kollmorgen, Tech. Rep., 2018.

[7] G. Pfaff, A. Weschta, and A. F. Wick, "Design and experimental results of a brushless ac servo drive," *IEEE Transactions on Industry Applications*, vol. IA-20, no. 4, pp. 814–821, 1984.

[8] "Robotics and automation," Mayr Antriebstechnik, Tech. Rep., 2022.

[9] R. Camilleri, D. A. Howey, and M. D. McCulloch, "Predicting the temperature and flow distribution in a direct oil-cooled electrical machine with segmented stator," *IEEE Transactions on Industrial Electronics*, vol. 63, no. 1, pp. 82–91, 2016.

[10] A. H. Mohamed, H. Vansompel, and P. Sergeant, "An integrated modular motor drive with shared cooling for axial flux motor drives," *IEEE Transactions on Industrial Electronics*, vol. 68, no. 11, pp. 10 467–10 476, 2021.

[11] Z.-p. Tang, Y.-c. Wang, F. Zhou, F.-y. Yu, J. F. Gieras, and J.-x. Shen, "Study on heat dissipation of low-speed outer rotor permanent magnet motor based on multi-phase flow model," in *Conference Proceedings of 2021 International Joint Conference on Energy, Electrical and Power*

Engineering, W. Cao, C. Hu, X. Huang, X. Chen, and J. Tao, Eds. Singapore: Springer Nature Singapore, 2022, pp. 607–620.

[12] P. Gnacinski, "Effect of unbalanced voltage on windings temperature, operational life and load carrying capacity of induction machine," *Energy Conversion and Management*, vol. 49, no. 4, pp. 761–770, 2008.

[13] A. Adouni and A. J. Marques Cardoso, "Thermal analysis of low-power three-phase induction motors operating under voltage unbalance and inter-turn short circuit faults," *Machines*, vol. 9, no. 1, 2021.

[14] "Universal robots - robotiq," https://robotiq.com/cobot-brands/universal-robots, accessed: 2023-01-04.

[15] J. Melkebeek, *Electrical Machines and Drives: Fundamentals and Advanced Modelling*. Springer Cham, 2018.

[16] R. Di Stefano and F. Marignetti, "Electromagnetic analysis of axial-flux permanent magnet synchronous machines with fractional windings with experimental validation," *IEEE Transactions on Industrial Electronics*, vol. 59, no. 6, pp. 2573–2582, 2012.

[17] Vansompel, Hendrik, "Design of an energy efficient axial flux permanent magnet machine," Ph.D. dissertation, Ghent University, 2013.

[18] B. Li, Y. Yuan, P. Gao, Z. Zhang, and G. Li, "Cooling structure design for an outer-rotor permanent magnet motor based on phase change material," *Thermal Science and Engineering Progress*, vol. 34, p. 101406, 2022.

[19] N. Simpson, R. Wrobel, and P. H. Mellor, "Estimation of equivalent thermal parameters of impregnated electrical windings," *IEEE Transactions on Industry Applications*, vol. 49, no. 6, pp. 2505–2515, 2013.

[20] D. A. Howey, "Thermal design of air-cooled axial flux permanent magnet machines," Ph.D. dissertation, Imperial College London, 2010.

Chapter 6

Conclusion and Future Work

6.1 Conclusion

In the future, we expect more and more robots to leave the confined factory floor and take up tasks in a more unstructured, unknown and changing environment whilst closely collaborating with humans. This requires robots that are intrinsically safe to humans and their environment, robust to collisions, capable of highly dynamic motions to overcome obstacles and that can perceive their environment in order to react to sudden changes. Present day robots deployed in industry do not meet these requirements, and a large part of the reason for this lies in the their actuator architecture which is heavy and stiff. To meet the requirements, novel robots require actuators that:

- have a high torque density to make the actuator lightweight
- can accelerate to a high speed, to realize highly dynamic motions
- are robust to survive intentional and unintentional collisions
- are backdrivable, to facilitate the perception of the environment and ensure safe collaboration with humans
- are simple, which is required to limit the cost and make a widespread use possible

Quasi-direct-drive actuators meet all these requirements but one, perhaps also the most important one: “have a high torque density”. Insufficient torque density will constrain the capabilities of robots based on quasi-direct-drive actuators. Therefore this dissertation aims to increase their torque density.

A first step in this direction was the introduction of an axial endplate mount integration concept for the electric motor and power electronics in Chapter 2.

Integrating the motor and its power electronics converter creates the opportunity to share parts of the thermal management system i.e. a fan-heatsink combination in this case. Additionally, separate enclosures and wire harness connecting both are avoided. The torque density of this concept was evaluated using a 3D thermal finite element model validated by experimental data obtained on a testbench. As mentioned in Table 2.6, a torque density of 2 Nm/kg was achieved. When comparing this result to the state-of-the-art, it was concluded that there was still room for improvement. The type of conductor and the rotor mass were identified as key bottlenecks for the torque density, the latter falls beyond the scope of this work.

The poor fill factor and equivalent thermal conductivity of a winding based on round enamelled copper wire was indicated as a limiting factor for the torque density in Section 1.4. This challenge is addressed in Chapter 4. Anodized aluminum foil is proposed as an alternative because the electrical insulation constituted by the aluminum-oxide layer has a higher thermal conductivity and a higher fill factor is possible with a foil winding. Two electromagnetically identical motors were constructed, one for each type of conductor. An almost identical DC winding resistance was reported in Table 4.3 which is the result of the higher fill factor of the anodized aluminum foil despite aluminum's higher electrical resistivity. Up to an excitation frequency of 65 Hz also no difference in AC losses was observed due to the limited foil width. In Table 4.4, the higher equivalent thermal conductivity of the anodized aluminum foil winding was confirmed. The high fill factor and the lower density of aluminum eventually led to an experimentally measured increase of 13% in the torque per kg stator mass for the anodized foil winding stator (see Table 4.5). The better thermal properties are not reflected in this result as the winding thermal resistance was not dominant in the path from heat source to heat sink. Eventually, it was concluded that the use of anodized aluminum foil results in a higher torque density in designs where the winding body is the dominant thermal resistance and the foil width and excitation frequency are limited.

Apart from the clear potential of anodized aluminum foil proven in previous paragraph, without a proper manufacturing method it remains useless. To come to the results in previous paragraph, the two mechanical challenges mentioned in Section 1.4, originating from the nature of the anodized aluminum had to be addressed first. In Chapter 3, the YASA AFPMSM electric machine topology is brought forward. Its inherent segmented nature allows to rely on existing foil winding techniques which reduces the risk of damaging the brittle aluminum-oxide insulation layer. This chapter describes the preliminary design of a YASA AFPMSM based on the requirements of a quasi-direct-drive robotic actuator. The second mechanical challenge addressed in this chapter relates to connecting a copper wire to the anodized foil. This is required to

connect the winding to its power electronics converter, because the geometry of the foil does not allow a direct connection. Conventional soldering methods used for copper wire cannot be used any more due to the high melting temperature and hardness of the aluminum-oxide layer which impedes diffusion of the metals. Ultrasonic welding is examined thoroughly in this chapter as the ultrasonic vibration and pressure can break the hard oxide layer and create a strong bond between wire and aluminum foil. Although good electrically conducting welds were obtained, the mechanical properties remained unsatisfactory for further handling of the coils during manufacturing. Eventually, two pads of the foil were electrolytically nickel-plated facilitating conventional soldering of the copper wire. This method showed satisfactory electrical and mechanical properties.

Finally, in Chapter 5 the last challenge mentioned in Section 1.4 was addressed: overheating due to an uneven loss distribution at standstill. The actuators in legged quadrupeds, humanoids or grippers often produce a high torque at almost standstill, also known as stall torque. This leads to an uneven loss distribution in the winding and if the stall torque is not derated with respect to the nominal torque also to overheating. The influence of the slot/pole combination, thermal end-winding interconnection and equivalent thermal conductivity of the winding on the required derating were studied experimentally in this chapter. From Fig. 5.15, it could be concluded that only the slot/pole combination and thermal end-winding interconnection can have an influence on the derating with up to 8% increase in the stall torque performance. Improving the thermal conductivity of the winding does not lead to a better stall torque performance as illustrated in Fig. 5.18. It improves both the rated torque and thus also the stall torque but it does not allow to decrease the derating. Overall, it can be concluded that design measures focusing on improving the stall torque performance can only to a minor extent reduce the required derating at standstill. It is better to focus on design measures that improve general thermal performance since they also lead to a higher stall torque, therefore this research topic will not be given further attention in the future work section.

6.2 Future Perspectives

When overlooking the research results summarized in previous section, it can be concluded that anodized aluminum foil has proven that it can outperform round enamelled copper wire for a direct-drive robotic actuator. One of the first priorities for future work, is to evaluate its performance in quasi-direct-drive applications similar to what was described in Chapter 4 but now increasing the maximum speed at which both motors are tested. It can be argued however that the validity of this conclusion is limited to the very specific application

characteristics and geometry of the anodized aluminum foil winding YASA AFPMSM realized in this dissertation. This is true, however this is the first reported realization of a rotating electrical machine based on this type of conductor which is a fundamental step in exploring its possibilities. Moreover this step has allowed to identify three interesting future research directions described in the following subsections that can build upon the knowledge created in this dissertation.

6.2.1 Electrical Insulation Properties of Anodized Aluminum

The turn-to-turn electrical insulation capabilities of the anodized aluminum foil have proven sufficient for the YASA AFPMSM realized in this dissertation. However, the fact that the breakdown voltage decreases with bending radius and the difficulty to insulate the foil edges might raise serious concerns about the insulation reliability in different motor designs. To facilitate the assessment of anodized aluminum in other motor designs, more research is required into the insulation properties of anodized aluminum: both on a fundamental level and on the application level. In [1], breakdown voltage between two foils wound on a bobbin was determined. The bobbins were positioned orthogonally to each other to avoid edge effects. Although it gives a good indication of the maximum theoretical breakdown voltage, this situation does almost never occur in an electric machine. Preliminary experiments on a bifilar coil with open ends were performed in this work, they have shown that the edges constitute the weak spots in a real coil. Additionally, the influence of ageing on the insulation properties of anodized aluminum is still an open research topic. The fundamental ageing phenomena under electrical, thermal and mechanical stress are known from the use of aluminum-oxide substrates in power electronics [2]. However, the electrical, thermal and mechanical stresses in an electric machine are very different. A preliminary study on the effect of thermal ageing on the insulation properties was presented in [3]. An unexplainable decrease in the insulation thickness was observed after ageing for several days at a high constant temperature. This indicates more fundamental and applied research on ageing is required to gain sufficient confidence in the capabilities of anodized aluminum.

Apart from the need for more fundamental and applied knowledge on the insulating properties and the influence of ageing, three strategies could be identified that might offer a workaround for the dependence of the insulation properties on the bending radius and thus on the motor design or manufacturing method:

- *Coating the edges:* No oxide coating can be applied on the foil edge because its bending radius approaches zero. Although it was not strictly

necessary in this work for insulation reasons, the anodized aluminum foil coils were potted using a low viscosity epoxy resin as described in Chapter 3. Because the edges of the used foil are chamfered, the epoxy resin can penetrate the space between two foil edges and reinforce the electrical insulation locally. Excessive flow of epoxy between the foils should be avoided as this could be detrimental for the thermal conductivity.

- *Alternative electric machine topology:* Although the inherent segmented nature of a YASA AFPMSM make winding of the foil coils outside the motor possible, during the consequent stator manufacturing process, they might get damaged by when inserting the coils in the stator. In transverse flux machines [4], the foil can be wound directly on the stator yoke which might also offer a protection during consequent handling. Additionally, directly winding the foil on the stator yoke might result in a good thermal contact with the stator yoke which can provide an efficient path for heat dissipation. Moreover, due to its high torque density, a transverse flux machine was also indicated as good machine topology for robotic applications [4, 5].

- *Alternative conductor geometries:* an alternative strategy to avoid insufficient breakdown voltage due to excessive bending of the foil during winding, is simply not to deform the conductor. A foil conductor geometry is however not suited for this. In the recently granted European Horizon RIA project CliMAFlux, a YASA AFPMSM with a flat concentrated winding tooth coil using anodized aluminum will be evaluated (See Fig. 6.1). Although a manufacturing method is not fixed yet, it could be investigated if anodization is possible after winding as this could drastically reduce the deformation. This can be done e.g. by slightly stretching the flat winding axially to allow the electrolytic solution to reach the complete conductor surface.

  For radial flux machines with distributed windings, a hairpin winding based on flat or rectangular conductors can be considered. The conductors undergo very limited deformation if anodization is done after forming of the conductors. However, welding of the hairpin ends still requires to remove the oxide layer locally and re-insulate the ends. A continuous wave winding eliminates the need for welding and if anodization is done right before insertion into the slots, excessive deformation is also avoided.

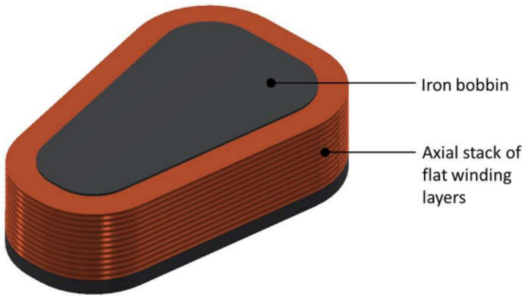

Figure 6.1: Conceptual drawing of a flat concentrated winding tooth coil of a YASA AFPMSM [6].

6.2.2 Demonstration of High Temperature (>450°C) Capabilities

Anodized aluminum foil was considered in this work to increase the torque density of quasi-direct-drive robotic actuators. This was mainly motivated by its higher equivalent thermal conductivity, the lower density of aluminum and the higher fill factor possible with foil conductors. The capability of anodized aluminum foil to operate at high temperature could further improve torque density. Although it has been considered, it was not exploited in this dissertation as operating an electric motor at >450°C gives rise to a number of other research challenges that need to be tackled as well. To name only one: the use of organic epoxy potting for fixating the coils is not longer possible. Preliminary experiments with a ceramic aluminum-oxide based potting material were performed in this dissertation [7]. However, it appeared difficult to cure thick layers without cracking. The idea of reinforcing the ceramic potting with glass, basalt or steel fibre could be explored in future research because it was shown already in [8] that stability of a building after a fire can be enhanced by adopting this reinforced concrete based on a similar ceramic potting or cement.

6.2.3 Light Weight Rotor

In Section 2.2.4, both the type of conductor and rotor were identified as key determinants of the torque density. An alternative type of conductor was already thoroughly investigated and discussed in previous chapters. The optimization of the rotor configuration is one of the subjects that will be investigated in the recently granted European Horizon RIA project CliMAFlux. The project will focus on the use of lightweight composite structures to reduce the rotor mass.

References

[1] S. Babicz, S. Ait-Amar Djennad, and G. Velu, "Preliminary study of using anodized aluminum strip for electrical motor windings," in *2014 IEEE Conference on Electrical Insulation and Dielectric Phenomena (CEIDP)*, 2014, pp. 176–179.

[2] D. Malec, S. Dinculescu, and T. Lebey, "Aging of ceramic materials used in power electronic substrates," in *2000 Annual Report Conference on Electrical Insulation and Dielectric Phenomena (Cat. No.00CH37132)*, vol. 2, 2000, pp. 604–607 vol.2.

[3] S. Ait-Amar, R. Saoudi, and G. Velu, "Thermal aging study of an anodized aluminum strip wire for winding and high temperature use," *Energies*, vol. 15, no. 15, 2022.

[4] B. Kaiser and N. Parspour, "Transverse flux machine - a review," *IEEE Access*, vol. 10, pp. 18 395–18 419, 2022.

[5] M. Keller, S. Muller, and N. Parspour, "Design of a transverse flux machine as joint drive for an articulated six-axis robot arm," in *2016 International Symposium on Power Electronics, Electrical Drives, Automation and Motion (SPEEDAM)*, 2016, pp. 849–854.

[6] R. Camilleri and M. McCulloch, "A new flat winding construction for direct liquid cooled axial flux machine with segmented stators," in *2018 XIII International Conference on Electrical Machines (ICEM)*, 2018, pp. 2416–2422.

[7] Resbond 989f datasheet. Available at https://www.cotronics.com/catalog/27%20989%20989FS%20989F.pdf (accessed: 12-06-2023).

[8] S. Guler and Z. F. Akbulut, "Effect of high-temperature on the behavior of single and hybrid glass and basalt fiber added geopolymer cement mortars," *Journal of Building Engineering*, vol. 57, p. 104809, 2022.